TWO UNCONVENTIONAL APPROACHES TO ELECTROMAGNETIC INVERSION

Hierarchical Bayesian Inversion and Inverse Scattering Series

by

Myoung Jae Kwon

A thesis submitted to the Faculty and the Board of Trustees of the Colorado School of Mines in partial fulfillment of the requirements for the degree of Master of Science (Geophysics).

Golden, Colorado

Date _____

Signed: _____
Myoung Jae Kwon

Approved: _____
Dr. Roel K. Snieder
Professor of Geophysics
Thesis Advisor

Golden, Colorado

Date _____

_____
Dr. Terence K. Young
Professor and Head,
Department of Geophysics

ABSTRACT

Electromagnetic methods are effective complementary tools, when combined with seismic exploration, for the delineation of a hydrocarbon reservoir, because electromagnetic methods provide extra information about, for example, electric conductivity, which is an important property for the economic evaluation of reservoirs. In this study, we analyze unconventional approaches of electromagnetic inversion: hierarchical Bayesian inversion and inverse scattering series. We apply the hierarchical Bayesian inversion to the uncertainty analysis for the joint inversion and utilize rock-physics models to integrate these two disparate data sets. The study shows that the uncertainties in the seismic wave velocity and electric conductivity play a more significant role in the variation of posterior uncertainty than do the seismic and CSEM data noise. The numerical simulations also show that the uncertainty in porosity is most affected by the uncertainty in seismic wave velocity and that the uncertainty in water saturation is most influenced by the uncertainty in electric conductivity. The framework of the uncertainty analysis presented in this study can be utilized to effectively reduce the uncertainty of the porosity and water saturation derived from integration of seismic and CSEM data. We also study the feasibility of the inverse scattering series, which can effectively resolve the nonlinearity of an inverse problem, for the interpretation of electromagnetic data. The application of the inverse scattering series has been limited because the series converges when the reference model sufficiently close to the true model. This study quantifies convergence conditions of the inverse scattering series and suggests a different approach of the inverse series, the modified inverse scattering series, which guarantees the convergence of the series and facilitates the choice of a reference model.

TABLE OF CONTENTS

LIST OF FIGURES

LIST OF TABLES

ACKNOWLEDGMENTS

I began working on electromagnetic inversion in the Summer of 2007 under Dr. Roel Snieder after being asked to join the Center for Wave Phenomena as a research assistant. His thoughtful acts of guidance is the reason I have arrived to the position I am currently. I am proud to think of him as more than an advisor but also as a friend. I would also like to thank the Center for Wave Phenomena consortium for funding my research and exposing me to new ideas. I also want to thank my research committee members Dr. André Revil and Dr. Terry Young for their support, help, and guidance on my project. Their insight extended my work outside the intent of the application. I also want to thank Dr. Luis Tenorio for his teaching on statistics and ideas for research. I acknowledge Inge Myrseth (Norwegian University of Science and Technology), Malcolm Sambridge (Australian National University), Arthur Weglein (University of Houston), Dmitry Avdeev (Halliburton), Evert Slob (Delft University of Technology), Yuanzhong Fan (Shell International), Mike Batzle, Misac Nabighian and Steve Hill (Colorado School of Mines) for helpful information, discussions, and suggestions. I have been fortunate to be surrounded by intelligent and caring colleagues in the Geophysics Department.

Most importantly, I want to thank my wife for always supporting me and giving me encouragement. She was the driving force for me to complete my work here as a student of the Colorado School of Mines. Thank you all.

"All models are wrong but some are useful"

George E. P. Box

Chapter 1

INTRODUCTION

Geophysical methods are based on the theory of different physical fields propagating through the earth's interior. The most important geophysical methods include gravity, magnetic, electromagnetic, and seismic methods (Telford *et al.*, 1990). Among these, seismic exploration provides good structural information of the subsurface medium and is the major exploration method for the discovery of a hydrocarbon reservoir. Recently, the controlled-source electromagnetic (CSEM) exploration method has been considered a good complementary tool for hydrocarbon discovery because the method provides more decisive information about the reservoir composition than the seismic method. The CSEM method is an electromagnetic exploration method designed for marine environments; the theoretical foundation of the CSEM method was laid in the 1980s (Chave & Cox, 1982; Cox *et al.*, 1986). Since then, the application of the CSEM method for hydrocarbon exploration has been extensively studied (Hoversten *et al.*, 2006; Constable & Srnka, 2007). The electromagnetic field is sensitive to electric conductivity, and electric conductivity within the subsurface is predominantly influenced by water content: increasing water content causes larger conductivity. Hydrocarbons, on the other hand, are poor electric conductors. The significant difference of electric conductivity between water and hydrocarbons makes the CSEM method an ideal tool to distinguish a hydrocarbon reservoir from a water reservoir.

The goal of geophysical exploration is to determine the subsurface structure from

geophysical data. One usually approximates real geology by a more or less simple model and tries to determine the model parameters from the data. This approach is called an inverse problem. Geophysical inverse problems are very difficult problems due to the complex structure of the earth's interior. Moreover, inverse problems of electromagnetic data are large-scale, strongly nonlinear, and severely ill-posed (Jackson, 1972; Parker, 1977). The success of electromagnetic data interpretation thus depends on our ability to approximate real geological structures by reasonable models, and to solve the corresponding inverse problems effectively (Zhdanov, 2002). The most common approach of interpreting electromagnetic data is the optimization method. Two representative approaches of the optimization method have been applied to the interpretation of a CSEM data set: deterministic (Gribenko & Zhdanov, 2007) and stochastic optimization (Chen *et al.*, 2007). The deterministic approach, which is also known as gradient-based iterative nonlinear inversion, is more widely applied than the stochastic approach, which is still impractical when the dimension of the model parameter is large.

The interpretation result of electromagnetic data is non-unique and strongly depends on initial assumptions (Aster *et al.*, 2005). Several questions thus arise when interpreting an electromagnetic dataset. How can one be convinced of an inversion result? How can one quickly build a good starting model? This dissertation describes the journey I have taken to answer those questions.

The first question is called the appraisal problem of an inverse problem (Figure 1.1). Chapter 2 describes my study of the appraisal problem for the joint inversion of seismic and CSEM data, which are sensitive to different medium properties: the seismic method is sensitive to density and seismic wave velocity and the CSEM method to electric conductivity. There have been several approaches for joint inversion that

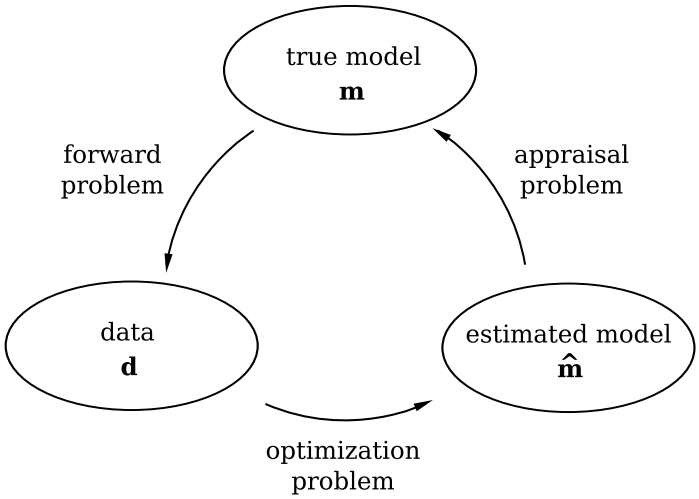

Figure 1.1. Division of an inverse problem into a forward problem, an optimization problem, and an appraisal problem (Snieder, 1998).

integrate disparate data sets. Some of them assume a common structure (Musil *et al.*, 2003) or similar structural variations of different medium properties (Gallardo & Meju, 2004; Hu *et al.*, 2009). Rock-physics models also enable one to interrelate seismic wave velocity and electric conductivity with the reservoir parameters such as porosity, water saturation, or permeability. Considering great economic significance of the reservoir parameters, I utilize rock-physics models to integrate these two disparate data sets and solve the appraisal problem by adopting a Bayesian model (Bayes, 1763; Tarantola, 2005; Ulrych *et al.*, 2001). The main goal of the uncertainty analysis is to investigate the relative contribution of different sources of overall uncertainty that arise when we use rock-physics models for joint inversion. These include seismic data noise, CSEM data noise, and uncertainties of rock-physics models. A series of numerical simulations reveals that the uncertainties in the seismic wave velocity and electric conductivity play a more significant role in the variation of posterior uncertainty than do the seismic and CSEM data noise. The numerical simulations also show that the

uncertainty in porosity is most affected by the uncertainty in seismic wave velocity and that the uncertainty in water saturation is most influenced by the uncertainty in electric conductivity. The framework of the uncertainty analysis in Chapter 2 can be utilized to effectively reduce the uncertainty of the porosity and water saturation derived from integration of seismic and CSEM data.

The rest of this dissertation is associated with the second question: how can one quickly build a good starting model? This question let me study an intriguing approach, the inverse scattering series (ISS), that effectively resolves the nonlinearity of an inverse problem and may be a framework that quickly yields an inversion result. The ISS is originally an approach of solving inverse problems in quantum scattering theory (Gel'fand & Levitan, 1951; Jost & Kohn, 1952; Moses, 1956; Prosser, 1969). The basic idea of the inverse scattering series is apprehended by considering the following example of two complex variables x and y that are related by

$$y = e^x - 1 = \sum_{n=1}^{\infty} \frac{x^n}{n!}, \quad \text{for all } x. \tag{1.1}$$

Regarding equation (1.1) as a forward scattering series between x and y, we express the inverse scattering series between the two variables as

$$x = \sum_{n=1}^{\infty} a_n y^n. \tag{1.2}$$

Substituting equation (1.2) into the forward scattering series and equating terms that are of the same order of y yields the following set of equations:

$$1 = a_1, \tag{1.3}$$

$$0 = a_2 + \frac{a_1}{2}, \tag{1.4}$$

$$\begin{aligned} 0 &= a_3 + a_1 a_2 + \frac{a_1^3}{6}, \\ &\dots \end{aligned} \tag{1.5}$$

One can recursively solve the above set of equations and write the inverse scattering series as

$$x = \sum_{n=1}^{\infty} (-1)^{n+1} \frac{y^n}{n}, \quad \text{for } |y| < 1, \tag{1.6}$$

which coincides with the Taylor series expansion of $x = \ln(1 + y)$ in order of y. The two variables of the example, x and y, correspond to scattered fields and model perturbations of inverse scattering problems, respectively. The geophysical application of the ISS has focused previously on seismic exploration, in particular on velocity estimation and multiple suppression (Weglein *et al.*, 1981, 1997, 2003). However, the inverse scattering series has not been widely applied to the interpretation of electromagnetic data. This dissertation describes the feasibility study of this application.

The first step of the feasibility study is to analyze the convergence conditions of the forward (FSS) and inverse scattering series (ISS). Compared to seismic exploration, electromagnetic methods are characterized by a rapid spatial decay of the probing field and a strong perturbation of the medium parameters. Chapter 3 discusses the difference between the convergence patterns of the scattering series for acoustic wave propagation and electromagnetic diffusion problems. Analysis of the formal expressions of the scattering series solutions shows that for electromagnetic diffusion, one can improve the convergence of the ISS by choosing a reference medium that is less conductive than the true medium. The analysis also shows that there is no fundamental difference between the convergence pattern of the scattering series

for the acoustic wave and electromagnetic diffusion equations. In other words, the rapid spatial decay of a diffusive field does not necessarily mean fast convergence of the scattering series for the diffusion equation. Model tests with parameters representing geophysical exploration of hydrocarbon reservoirs suggest, however, that the scattering series for the electromagnetic diffusion equation converges faster than that for the acoustic wave equation.

The analysis of the convergence conditions in Chapter 3 provides insight into model reconstructions via the ISS. Chapter 4 demonstrates 1D examples of electromagnetic model reconstruction via the ISS. and exemplifies that the ISS converges only when the contrast between true and reference models is sufficiently small. Chapter 4 also discusses the origin of the narrow range of convergence and qualitatively describes that there are two contradictory conditions that determine the convergence of the ISS. To mitigate the convergence conditions, I propose an alternative approach to electromagnetic data inversion: the modified inverse scattering series (MISS), which is based on the iterative dissipative method (IDM) (Singer, 1995; Singer & Fainberg, 1995; Avdeev *et al.*, 1997). The IDM provides an absolutely converging forward series, and the MISS, which is based on the IDM, converges for a wider contrast of the electric conductivity between true and reference models than the ISS. Several 1D tests also demonstrate that models reconstructed by the MISS are closer to true models than models generated via the ISS. This study shows that the MISS enables fast reconstruction of an electromagnetic model, which can be a good starting model for large-scale geophysical data processing, such as marine controlled-source electromagnetic (CSEM) data inversion.

Chapter 2

UNCERTAINTY ANALYSIS FOR THE INTEGRATION OF SEISMIC AND CSEM DATA

2.1 Summary

We study the appraisal problem for the joint inversion of seismic and controlled source electro-magnetic (CSEM) data and utilize rock-physics models to integrate these two disparate data sets. The appraisal problem is solved by adopting a Bayesian model and we incorporate four representative sources of uncertainty. These are uncertainties in (1) seismic wave velocity, (2) electric conductivity, (3) seismic data, and (4) CSEM data. The uncertainties in porosity and water saturation are quantified by a posterior random sampling in the model space of porosity and water saturation in a marine one-dimensional structure. We study the relative contributions from the four individual sources of uncertainty by performing several statistical experiments. The uncertainties in the seismic wave velocity and electric conductivity play a more significant role in the variation of posterior uncertainty than do the seismic and CSEM data noise. The numerical simulations also show that the uncertainty in porosity is most affected by the uncertainty in seismic wave velocity and that the uncertainty in water saturation is most influenced by the uncertainty in electric conductivity. The framework of the uncertainty analysis presented in this study can be utilized to effectively reduce the uncertainty of the porosity and water saturation derived from integration of seismic and CSEM data.

2.2 Introduction

The controlled source electromagnetic (CSEM) method has been studied for the last few decades (Chave & Cox, 1982; Cox *et al.*, 1986) and its application for the delineation of a hydrocarbon reservoir has recently been discussed (Constable & Srnka, 2007). Currently, there is an increasing interest in the integration of the seismic and controlled source electro-magnetic (CSEM) method in deep marine exploration (Harris & MacGregor, 2006). Although the CSEM method has less resolution than the seismic method, it provides extra information about, for example, electric conductivity. This property is important for the economic evaluation of reservoirs. Therefore, the CSEM method is considered an effective complementary tool when combined with seismic exploration.

The seismic and CSEM methods are disparate exploration techniques that are sensitive to different medium properties: the seismic method is sensitive to density and seismic wave velocity and the CSEM method to electric conductivity. There have been several approaches for joint inversion that integrate disparate data sets. Some of them assume a common structure (Musil *et al.*, 2003) or similar structural variations of different medium properties (Gallardo & Meju, 2004; Hu *et al.*, 2009). More recently, the application of rock-physics models for joint inversion has been studied (Hoversten *et al.*, 2006). Rock-physics models enable us to interrelate seismic wave velocity and electric conductivity with the reservoir parameters such as porosity, water saturation, or permeability. The main advantage of the approach is that these reservoir parameters have great economic importance. The application of a rock-physics model is limited, however, by the fact that such a model is site-specific and there are not yet any universal solutions to the inverse problem. Furthermore, even for a particular area of interest, any rock-physics model is generally described

as a cloud of samples. These limitations imply that joint inversion via a rock-physics model intrinsically necessitates a stochastic approach. Stochastic inversion has recently been studied for seismic inversion (Spikes *et al.*, 2007) and joint inversion of seismic and CSEM data (Chen *et al.*, 2007). The contributions of rock-physics model uncertainties are also being studied (Chen & Dickens, 2009). Generally, the accuracy of joint inversion of seismic and CSEM data via rock-physics models is limited by the uncertainty of the rock-physics model as well as by the data noise. The contribution of seismic and CSEM data noise on the joint inversion via rock-physics models, however, has not yet been studied. Moreover, it is not yet understood whether rock-physics model uncertainties play a more significant role than data noise on the joint inversion process.

We aim to investigate the relative contribution of different sources of overall uncertainty that arise when we use rock-physics models for joint inversion. These include seismic data noise, CSEM data noise, and uncertainties of rock-physics models. We implement several numerical experiments that reflect scenarios we may encounter in practice and compare the uncertainties in the inferred parameters. The comparison reveals the relative contributions of different sources of uncertainty and we can utilize the procedure to more effectively reduce the uncertainty, depending on whether our interests focus on porosity or water saturation.

2.3 Methodology

The goal of geophysical inversion is to make quantitative inferences about the earth from noisy data. There are mainly two different approaches for attaining this goal: in one, the unknown models are assumed to be deterministic and one uses inversion methods such as Tikhonov regularization (Tikhonov & Arsenin, 1977; Aster

et al., 2005); in the other, all the unknowns are random and one uses Bayesian methods (Bayes, 1763; Tarantola, 2005; Ulrych *et al.*, 2001). The objective of this project is to provide a framework for Bayesian joint inversion that leads to model estimates and their uncertainties.

The connection between geophysical data $\mathbf{d}$ and model $\mathbf{m}$ is written as

$$\mathbf{d} = L[\mathbf{m}] + \mathbf{e} \tag{2.1}$$

where L denotes a linear or nonlinear operator that maps the model into the data and $\mathbf{e}$ represents data measurement error. The details of the operator are presented in the modeling procedure section. Bayes' theorem relates conditional and marginal probabilities of a data $\mathbf{d}$ and a model $\mathbf{m}$ as follows (Tarantola, 2005):

$$\pi(\mathbf{m}|\mathbf{d}) = \frac{\pi(\mathbf{m})f(\mathbf{d}|\mathbf{m})}{\pi(\mathbf{d})} \propto \pi(\mathbf{m})f(\mathbf{d}|\mathbf{m}), \tag{2.2}$$

where $\pi(\mathbf{m})$ is a prior probability in the sense that it does not take into account any information about the data $\mathbf{d}$; $f(\mathbf{d}|\mathbf{m})$ is likelihood of the data $\mathbf{d}$, given a model $\mathbf{m}$; and $\pi(\mathbf{m}|\mathbf{d})$ is a posterior probability density that we are inferring.

2.3.1 Hierarchical Bayesian model

The P-wave velocity and electric conductivity are derived from two reservoir parameters: porosity and water saturation. These reservoir parameters are the target model parameters in this project. There are two layers of likelihood probabilities that have hierarchical dependency. The variables and their hierarchical dependencies are displayed in Figure 2.1. The uppermost row represents prior probabilities of the reservoir parameters: the porosity ($\mathbf{m}_\phi$) and water saturation ($\mathbf{m}_{S_w}$); the middle

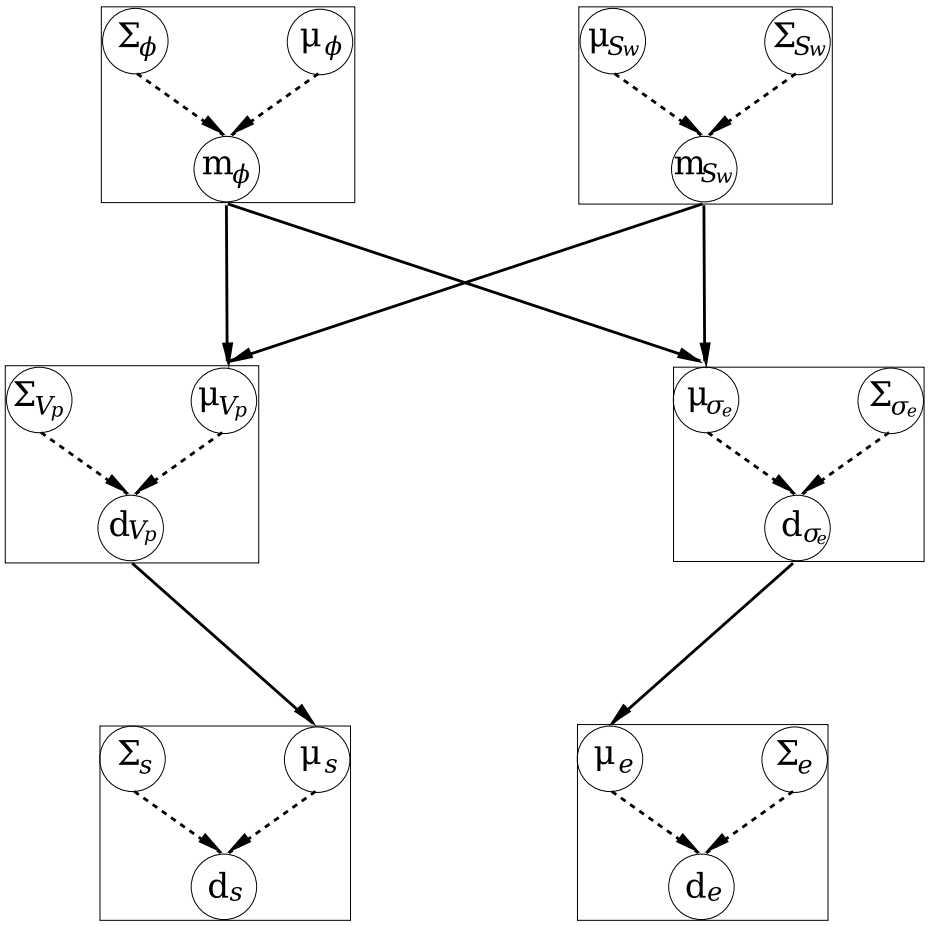

Figure 2.1. A hierarchical dependency structure represented by a directed graph. The nodes represent stochastic variables, the dashed arrows represent probability dependencies, and the solid arrows represent deterministic relationships. μ and $\mathbf{\Sigma}$ denote expectation vectors and covariance matrices, respectively. $\mathbf{m}_\phi$ and $\mathbf{m}_{S_w}$ represent two reservoir parameters: medium porosity and water saturation. $\mathbf{d}_{V_p}$ and $\mathbf{d}_{\sigma_e}$ denote P-wave velocity and logarithm of electric conductivity, respectively. $\mathbf{d}_s$ and $\mathbf{d}_e$ represent two different data sets: seismic and CSEM data.

row denotes the likelihoods of the P-wave velocity ($\mathbf{d}_{V_p}$) and logarithm of electric conductivity ($\mathbf{d}_{\sigma_e}$). Finally, the lowermost row represents the likelihoods of the seismic ($\mathbf{d}_s$) and CSEM data ($\mathbf{d}_e$).

Within the Bayesian framework, the prior probabilities of the reservoir parameters are expressed as $\pi_{prior}(\mathbf{m}_\phi)$ and $\pi_{prior}(\mathbf{m}_{S_w})$. Likewise, four possible likelihoods are expressed as follows: the likelihoods of the P-wave velocity $f(\mathbf{d}_{V_p}|\mathbf{m}_\phi, \mathbf{m}_{S_w})$, logarithm of electric conductivity $f(\mathbf{d}_{\sigma_e}|\mathbf{m}_\phi, \mathbf{m}_{S_w})$, seismic data $f(\mathbf{d}_s|\mathbf{d}_{V_p})$, and CSEM data $f(\mathbf{d}_e|\mathbf{d}_{\sigma_e})$. Therefore, the posterior probabilities (π_{post}) of the porosity and water saturation are derived from the prior (π_{prior}) and likelihood (f) probabilities as follows:

$$\begin{aligned} & \pi_{post}(\mathbf{m}_\phi, \mathbf{m}_{S_w}|\mathbf{d}_{V_p}, \mathbf{d}_{\sigma_e}, \mathbf{d}_s, \mathbf{d}_e) \qquad (2.3) \\ \propto \; & \pi_{prior}(\mathbf{m}_\phi)\pi_{prior}(\mathbf{m}_{S_w}) f(\mathbf{d}_{V_p}|\mathbf{m}_\phi, \mathbf{m}_{Sw}) f(\mathbf{d}_{\sigma_e}|\mathbf{m}_\phi, \mathbf{m}_{Sw}) f(\mathbf{d}_s|\mathbf{d}_{Vp}) f(\mathbf{d}_e|\mathbf{d}_{\sigma_e}). \end{aligned}$$

Equation (2.3) indicates that the posterior probability is proportional to the product of individual priors and likelihoods.

In statistics, the central limit theorem states that the sum of a sufficiently large number of identically distributed independent random variables follows a normal distribution. This implies that the normal distribution is a reasonable choice for describing probability. Therefore, throughout this project, we assume that the priors and likelihoods generally follow multivariate Gaussian distributions with expectation vector μ and covariance matrix $\mathbf{\Sigma}$, such that

$$f(\mathbf{x}) = \frac{1}{\sqrt{(2\pi)^n \det(\mathbf{\Sigma})}} \exp\left[-\frac{1}{2}(\mathbf{x}-\mu)^T \mathbf{\Sigma}^{-1}(\mathbf{x}-\mu)\right], \qquad (2.4)$$

where $\mathbf{x}$ denotes data or model, and n denotes the dimension of $\mathbf{x}$. Equation (2.4)

expresses the general form of the probability function used in this project and the covariance matrices for individual prior and likelihoods are discussed later. Note that since the forward operations in this project (solid arrows in Figure 2.1) are nonlinear, the posterior distributions are not necessarily Gaussian.

2.3.2 Prior and likelihood model

In the Bayesian context, there are several approaches to represent prior information (Scales & Tenorio, 2001). The prior model encompasses all the information we have before the data sets are acquired. In practice, the prior information includes the definition of the model parameters, geologic information about the investigation area, and preliminary investigation results. Therefore, the prior model is the starting point of a Bayesian approach, and we expect to have a posterior probability distribution with less uncertainty than the prior probability. The prior model plays an important role in Bayesian inversion by eliminating unreasonable models that also fit the data (Tenorio, 2001). Obvious prior information we have is the definition of the porosity and water saturation, such that $0 \leq m_{\phi_i} \leq 1$ and $0 \leq m_{S_{w_i}} \leq 1$. This definition implies that the prior distributions of the porosity and water saturation are intrinsically non-Gaussian. Furthermore, there can be several fluid phases within pore space, and the probability distribution of each fluid saturation can be described by a different distribution such as Dirichlet distribution (Gelman *et al.*, 2003). In this study, we consider two fluid phases (gas and water) and assume that the variance of the water saturation is sufficiently small to warrant the assumption of Gaussian *a priori* probability density functions. We aim to assess the porosity and water saturation of the subsurface medium that has several layers. Generally, these reservoir parameters of each layer are correlated and have different variance. The assessment

of the correlation and variance requires detailed analysis of geology and well logging data. In this study, we focus on the formulation of Bayesian joint inversion and, as a starting point, regard that the reservoir parameters of each layer are uncorrelated and have identical variance. In other words, we assume that the covariance matrices $\mathbf{\Sigma}_{\phi}$ and $\mathbf{\Sigma}_{S_w}$ (Figure 2.1) are diagonal and that the diagonal elements within each covariance matrix are identical.

For the hierarchical Bayesian model shown in Figure 2.1, there are four elementary likelihoods. Each of these likelihoods describes how well any rock-physics model or geophysical forward modeling fits with the rock-physics experiment results or the noisy observations. The details of the likelihood modeling are covered in the modeling procedure section.

2.3.3 MCMC sampling

The assessment of the posterior probability requires great computational resources and, in most cases, is still impractical for 3-D inverse problems. Pioneering studies about the assessment were performed for 1-D seismic waveform inversion (Gouveia & Scales, 1998; Mosegaard *et al.*, 1997). The posterior model space of this project encompasses porosity and water saturation of several layers. We use a Markov-Chain Monte Carlo (MCMC) sampling method to indirectly estimate the posterior probability distribution of the porosity and water saturation. In this project, the goal of the MCMC sampling method is to retrieve a set of samples, such that the sample distribution describes the joint posterior probability of equation (2.3). The MCMC sampling method is a useful tool to explore the space of feasible solutions and to investigate the resolution or uncertainty of the solution (Mosegaard & Sambridge, 2002; Sambridge *et al.*, 2006). The Metropolis-Hastings algorithm (Hastings, 1970;

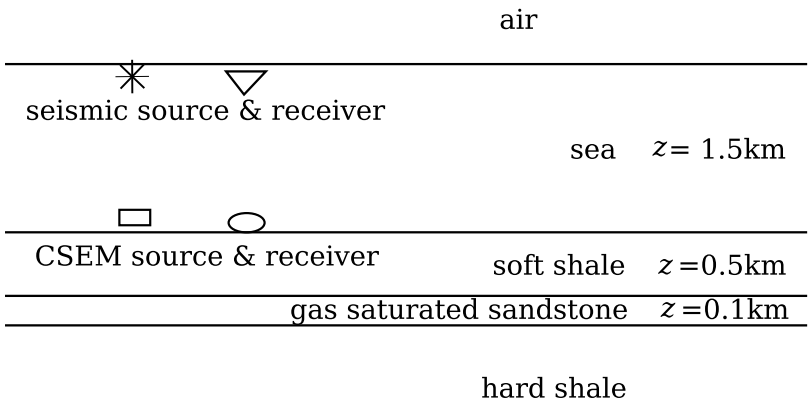

Figure 2.2. The employed marine 1-D model. Seismic source and receiver are located 10 m below the sea surface. CSEM source is located 1 m above the sea bottom and receiver is on the bottom. The earth is modeled as four homogeneous isotropic layers: seawater, soft shale, gas saturated sandstone, and hard shale. The air and hard shale layer are the two infinite half-spaces. The thicknesses (z) of the layers between the two half-spaces are fixed.

Metropolis *et al.*, 1953) and Gibbs sampler (Geman & Geman, 1984) are the most widely used samplers for this purpose. We apply the Metropolis-Hastings algorithm for the assessment of posterior probability. The details of the Metropolis-Hastings algorithm are presented in Appendix A.

2.4 Modeling procedures

The marine 1-D model used in this research is shown in Figure 2.2. The target layer, a gas saturated sandstone layer, is located between shale layers. The soft shale layer is modeled to have the highest clay content and the gas saturated sandstone layer to have the lowest clay content. The modeled values of the porosities ϕ, water saturations S_w, P-wave velocities V_p and electric conductivities σ_e are summarized in Table 2.1. The mean prior porosity μ_ϕ and water saturation μ_{S_w} values are assumed to be the modeled values.

Table 2.1. The modeled values of the porosity ϕ, water saturation S_w, P-wave velocities V_p, and electric conductivities σ_e of the 1-D model shown in Figure 2.2. ϕ_c is the critical porosity. K_d, K_0, and K_f denote the bulk modulus of the dry rock, mineral material, and pore fluid, respectively. μ_0 is the shear modulus of the mineral material, and ρ_w and ρ_0 are the density of the water phase and mineral material, respectively. σ_w denote the electric conductivity of the water phase, and m and n are the cementation and saturation exponents. CEC is the cation exchange capacity. The detailed explanation of the rock physics parameters is presented in Appendix B.

	soft shale	gas saturated sandstone	hard shale
ϕ (%)	35	25	10
S_w (%)	90	10	50
V_p (km/s)	2.28	3.56	4.88
σ_e (S/m)	0.580	0.007	0.044
ϕ_c (%)	60	40	40
K_w (MPa)	2.2	3.2	4.2
K_g (MPa)	0.03	0.03	0.03
K_0 (MPa)	16	36	40
μ_0 (MPa)	6	24	30
ρ_w (g/cc)	1	1	1
ρ_0 (g/cc)	2.55	2.65	2.75
σ_w (S/m)	3.33	3.33	3.33
m	2	2	2
n	2	2	2
CEC (C/kg)	10000	2000	6000

2.4.1 Rock-physics likelihood modeling

Rock-physics models play a central role in the joint inversion presented here. However, in many cases the rock-physics models are site-specific and complicated functions of many variables that include porosity, water saturation and clay content. Furthermore, there is an additional source of uncertainty associated with the choice of rock-physics model. The motivation of this research is not to develop rock-physics models that better describe the earth and have smaller uncertainty. Instead, it is to understand the contribution of rock-physics model uncertainties to the overall uncertainty of joint inversion. However, by comparing the posterior density functions from different possible rock-physics models, we can deduce which rock-physics model better fits the given lithology. In this study, we utilize several empirical relations that are widely accepted. The quantitative dependence of the P-wave velocity and electric conductivity on porosity and water saturation is presented in Appendix B.

As stated in Appendix B, the distribution of P-wave velocity is affected by several rock physics parameters and, in the scale of geophysical exploration, there is no statistical model that universally describes the distribution of P-wave velocity. The statistical description of P-wave velocity is therefore site-specific and involves detailed analysis of well logging data and laboratory experiments. The rough range of P-wave velocity of the earth minerals is 2 - 10 km/s (Mavko *et al.*, 1998). In this study, we adopt the Gaussian distribution for the modeling of uncertainty of P-wave velocity. In contrast, considering that the electric conductivity exhibits exponential variation in most geologic environments (Palacky, 1987), we assume that the electric conductivity follows a lognormal distribution. The P-wave velocity and electric conductivity are derived from the empirical relations, and Gaussian and lognormal random numbers are thereafter added to the P-wave velocity and electric conductivity, respectively,

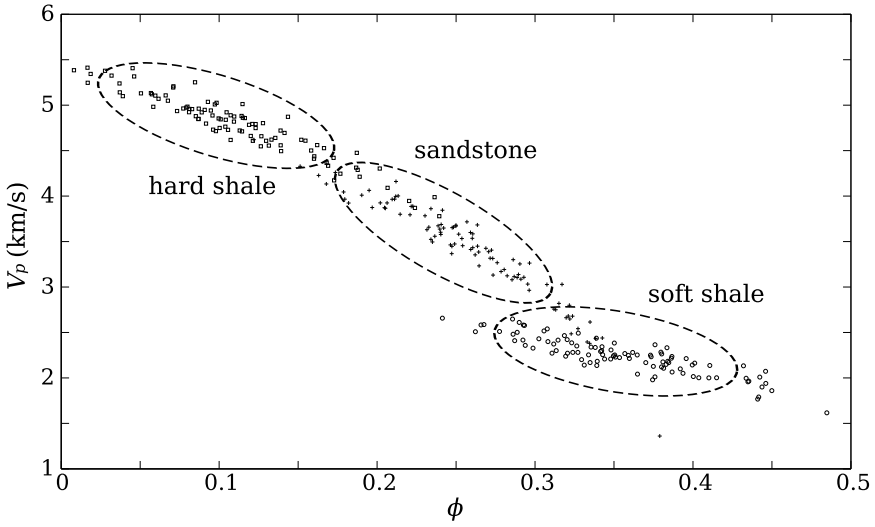

Figure 2.3. Simulated rock-physics model between porosity ϕ and P-wave velocity V_p. Among three layers, the P-wave velocity depends least on the porosity in the soft shale layer. The quantitative dependence of the P-wave velocity on porosity is presented in Appendix B and Table 2.1.

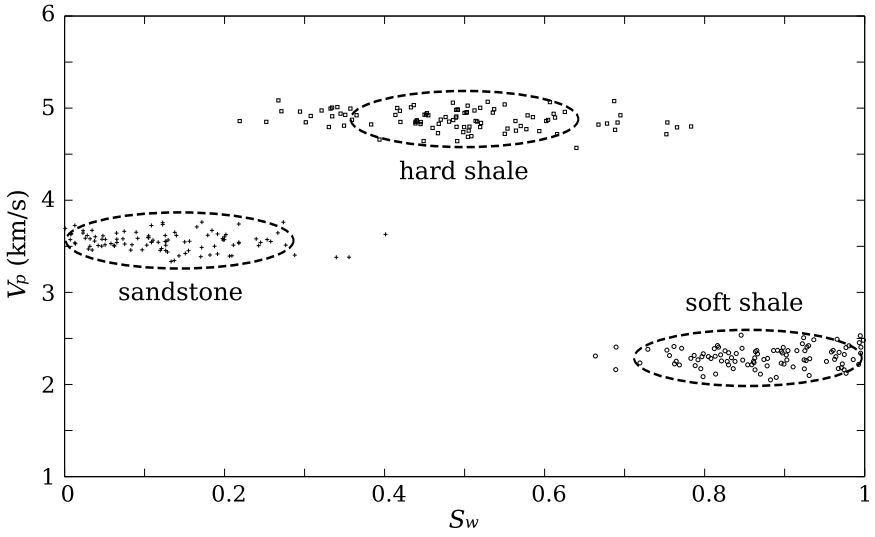

Figure 2.4. Simulated rock-physics model between water saturation S_w and P-wave velocity V_p. The P-wave velocity depends less on the water saturation than on the porosity. The quantitative dependence of the P-wave velocity on water saturation is presented in Appendix B and Table 2.1.

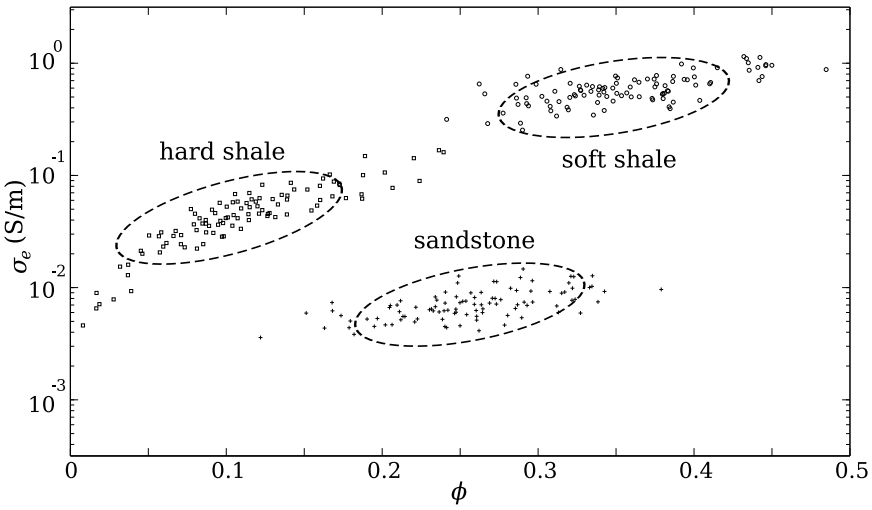

Figure 2.5. Simulated rock-physics model between porosity ϕ and electric conductivity σ_e. For each layer, increased porosity tends to accompany larger electric conductivity. The quantitative dependence of the electric conductivity on porosity is presented in Appendix B and Table 2.1.

to account for the uncertainty in the rock-physics model. Figures 2.3 through 2.6 show the simulated rock-physics models, where the porosity and water saturation samples of each layer are retrieved from the prior distributions. The distributions for the P-wave velocity indicate that the velocity is strongly dependent on the porosity and the contribution of the water saturation is less significant. In contrast, the distributions for the electric conductivity show that both the porosity and water saturation influence the electric conductivity. Note that the dependencies are different for each layer. The dependency of the P-wave velocity on the porosity is weakest in the soft shale layer and the dependency of the electric conductivity on the water saturation is strongest in the sandstone layer. These differential dependencies in the different layers play a significant role in the joint inversion presented for this project.

We assume the likelihoods of the P-wave velocity $f(\mathbf{d}_{V_p}|\mathbf{m}_\phi, \mathbf{m}_{S_w})$ and logarithm

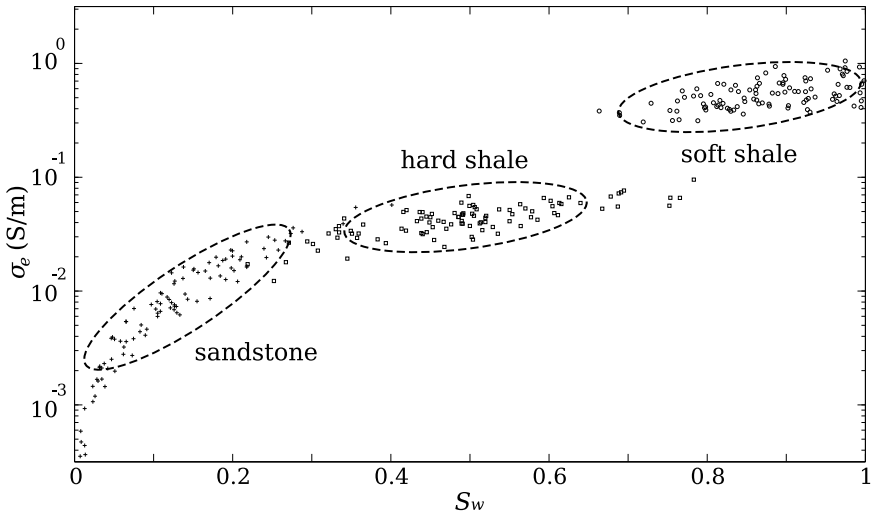

Figure 2.6. Simulated rock-physics model between water saturation S_w and electric conductivity σ_e. Among three layers, the dependency of the electric conductivity on the water saturation is strongest in the sandstone layer. The quantitative dependence of the electric conductivity on water saturation is presented in Appendix B and Table 2.1.

of electric conductivity $f(\mathbf{d}_{\sigma_e}|\mathbf{m}_\phi, \mathbf{m}_{S_w})$ to follow the multivariate Gaussian distribution (equation (2.4)). Generally, the P-wave velocity and logarithm of electric conductivity of the layers are correlated and have different variance. The assessment of the correlation and variance requires detailed analysis of geology and well logging data, which are beyond the scope this study. For the evaluation of the likelihoods, we assume that the P-wave velocity and electric conductivity of each layer (Figure 2.2) are independent. We model the covariance matrices $\mathbf{\Sigma}_{V_p}$ and $\mathbf{\Sigma}_{\sigma_e}$ (Figure 2.1) as diagonal matrices whose diagonal elements are constants.

2.4.2 Seismic data likelihood modeling

There are many kinds of seismic data we can utilize: reflection data, travel time data, amplitude versus offset or angle data, and full waveform data. The full wave-

form data is the most general and encapsulates the largest amount of information. Seismic migration is the most common approach for handling the full waveform data to reconstruct subsurface geometry. The application of the full waveform inversion is limited by its poor convergence speed. We use the waveform data for the joint inversion of seismic and CSEM data because the Monte Carlo method is effective for the least-squares misfit optimization for the velocities (Jannane *et al.*, 1989; Snieder *et al.*, 1989). Seismic waveform data is synthesized by a ray-tracing algorithm (Docherty, 1987) and we model the primary reflections of the P-wave from the top and bottom boundaries of the target sandstone layer. There are many sources of seismic noise in a marine environment: ambient noise, guided waves, tail-buoy noise, shrimp noise, and side-scattered noise (Yilmaz, 1987). We model the seismic noise by adding band-limited noise. The frequency band of the noise is between 10 and 55 Hz, and the central frequency of the source wavelet is 30 Hz.

We assume that the seismic data likelihood probability $f(\mathbf{d}_s|\mathbf{d}_{V_p})$ follows the multivariate Gaussian distribution (equation (2.4)). For the calculation of the likelihood, it is necessary to evaluate the covariance matrix $\mathbf{\Sigma}_s$ (Figure 2.1). For band-limited noise, the covariance matrix follows from the power spectrum of the bandpass filter and the resulting covariance matrix is not diagonal; a row of the covariance matrix is a sinc function. It is possible to derive the inverse covariance matrix from the above described covariance matrix. However, the inverse covariance matrix is generally unstable, and we need to truncate the singular values of the covariance matrix, which yields an inverse matrix that has no significant improvement over the inverse of a diagonal matrix. We therefore approximate the covariance matrix of a band-limited noise as the covariance matrix of a white noise. We model the covariance matrix Σ_s (Figure 2.1) as a diagonal matrix whose diagonal elements are constant.

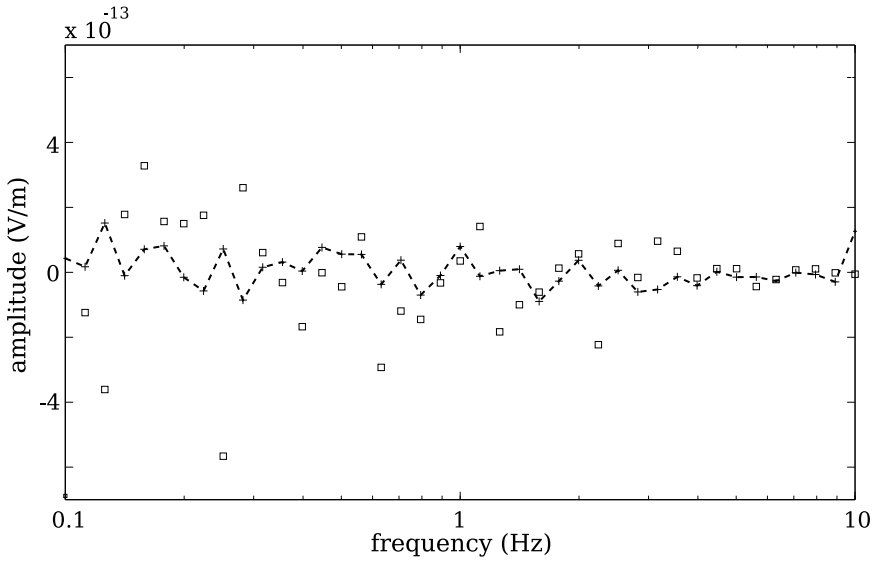

Figure 2.7. Two different types of CSEM noise: systematic noise (open dots) and non-systematic background noise (dashed curve). The systematic noise decreases with frequency. In contrast, the non-systematic noise is independent of frequency.

2.4.3 CSEM data likelihood modeling

The CSEM signal measured at a receiver location is comprised of three components. The first propagates through the solid earth and contains the information on the reservoir properties. The second propagates through the seawater and attenuates rapidly. It is therefore only significant near the transmitter. The third travels as a wave along the seawater-air interface (air-wave) and decreases with increasing water depth. In this project, the depth of the sea is 1.5 km and the air-wave is not significant.

Even though the deep sub-sea environment has little cultural noise, the CSEM measurements are not free from noise. These noise sources include the magneto-telluric signal, streaming potential, and instrument noise. The magneto-telluric signal is significant at frequencies lower than 1 Hz. The streaming potential is generated

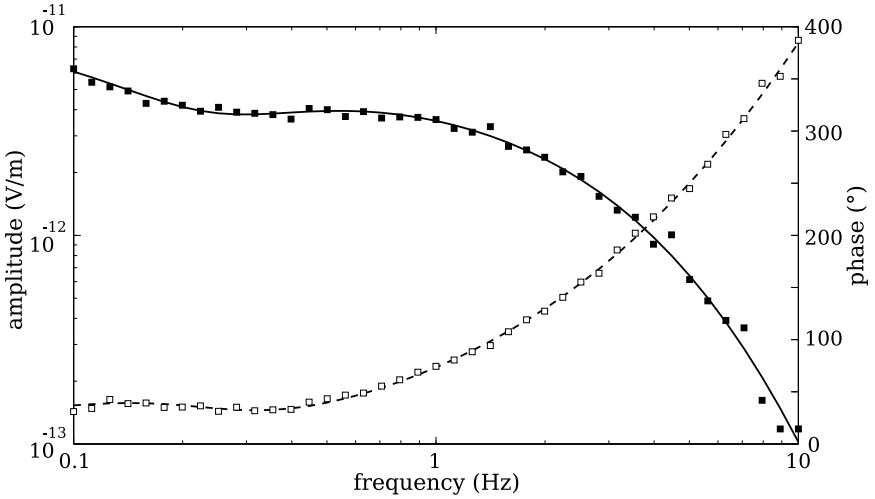

Figure 2.8. Electric field amplitude and phase response of a noise free (solid and dashed curves) and noise contaminated case (black and open dots). The exact electric conductivities are used for the CSEM data calculation shown here. The CSEM noise is significant in high frequency range.

by seawater movement. The natural background noise at frequencies around 1 Hz is about 1 pV/m (Chave & Cox, 1982) and its influence can be minimized by using a stronger transmitter. The instrument noise is more important and mainly comes from the transmitter amplifier or receiver electrodes. At lower frequency range, the noise from the amplifier and electrodes is proportional to $1/f$ and $1/\sqrt{f}$, respectively. On the other hand, the instrument noise is saturated at the higher frequency range, i.e., Johnson noise limit. Furthermore, the CSEM data quality is influenced by the positioning or aligning error of the transmitter and receiver locations/directions.

The CSEM data we utilize consists of the real and imaginary parts of the CSEM signal. We design the CSEM noise from the amplitude of the CSEM response and then add the noise to the real and imaginary parts of the response. The CSEM noise is categorized as systematic and non-systematic noise as shown in Figure 2.7. The

systematic noise includes instrument noise and positioning error. We assume the systematic noise to be proportional to the amplitude of the CSEM signal whereas the non-systematic noise is independent of the signal. A realization of noisy CSEM data is shown in Figure 2.8, where the systematic noise is 5% of each noise-free amplitude and the non-systematic noise is 5×10^{-14} V/m. The CSEM signal decreases with frequency and the CSEM noise is more obvious.

We assume the CSEM data likelihood probability $f(\mathbf{d}_e|\mathbf{d}_{\sigma_e})$ follows the multivariate Gaussian distribution (equation (2.4)). For the calculation of the likelihood, we assume that the CSEM data noise is independent. We model the covariance matrix $\mathbf{\Sigma}_e$ (Figure 2.1) as a diagonal matrix. Assuming that the systematic and non-systematic noise is uncorrelated, the diagonal element of the covariance matrix that corresponds to i-th datum (σ_i^2) is derived as

$$\sigma_i^2(d_e) = \sigma_i^2(\varepsilon_{\text{sys}}) + \sigma_i^2(\varepsilon_{\text{nonsys}}), \tag{2.5}$$

where ε_{sys} and $\varepsilon_{\text{nonsys}}$ denote the systematic and non-systematic noise, respectively. Note that $\sigma_i^2(\varepsilon_{\text{sys}})$ values decrease at the larger frequency whereas $\sigma_i^2(\varepsilon_{\text{nonsys}})$ is independent of frequency.

2.5 Uncertainty Analysis

2.5.1 Histogram analysis of posterior distributions

We perform MCMC sampling to describe the posterior probability distribution (equation (2.3)). The random sampling is performed within a six dimensional model space that accounts for porosity or water saturation of soft shale, sandstone, and hard shale layers (Figure 2.2). The initial sample is drawn from the prior distribution, and

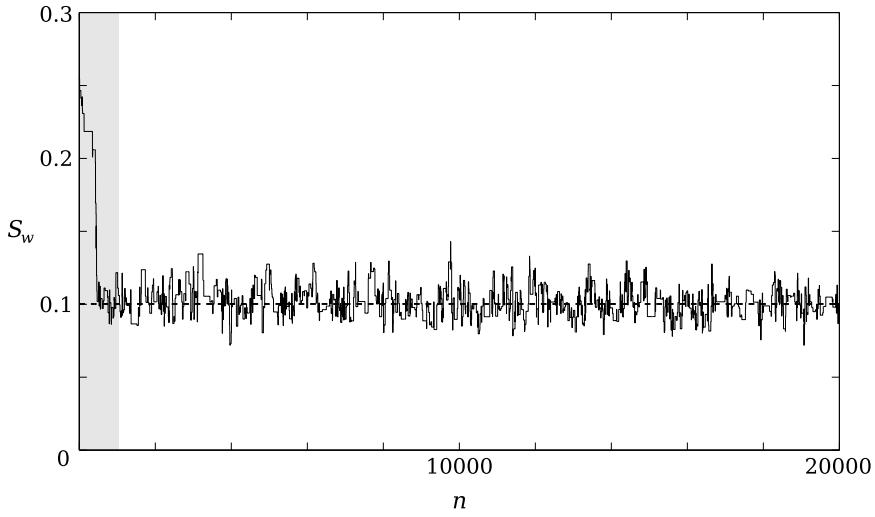

Figure 2.9. Samples of the water saturation (S_w) of the sandstone layer for subsequent samples with sampling number n. In the initial stage of random sampling (shaded area), the random sample is located away from the modeled value (dashed line) and shows gradual approach toward the posterior distribution (burn-in process). We discard the burn-in stage from the calculation of the sample variance.

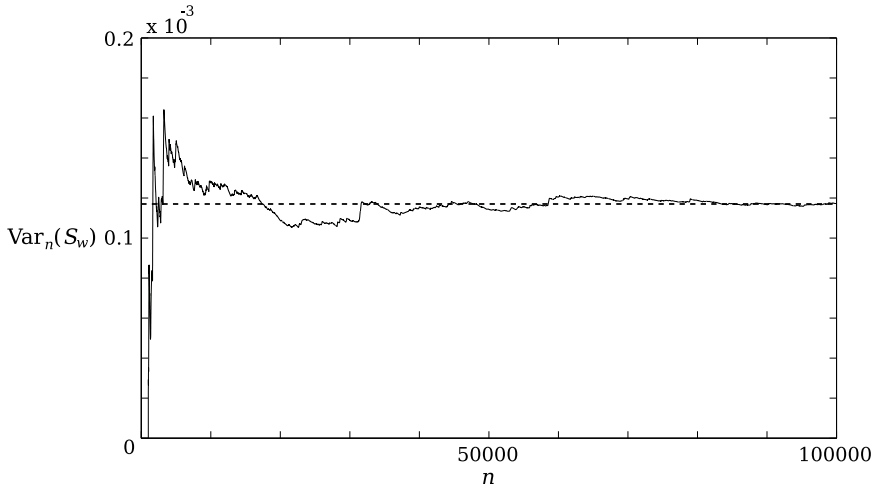

Figure 2.10. Convergence of the variance of the water saturation (S_w) as a function of the total number of samples. The burn-in samples are excluded from the calculation of the sample variance. For sufficiently large sampling number n, the variance of the random samples converges to the posterior variance value (dashed line).

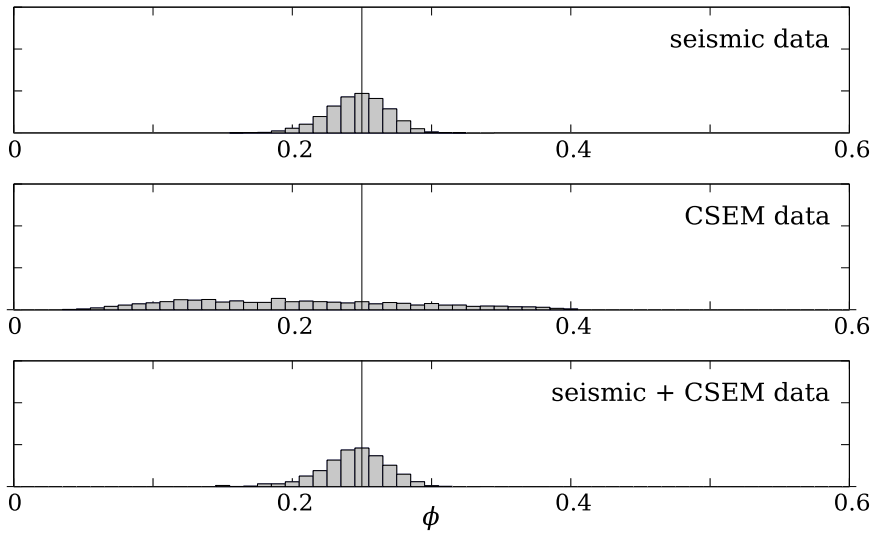

Figure 2.11. Histograms of posterior porosity (ϕ) samples of the sandstone layer. Vertical lines indicate the true porosity values.

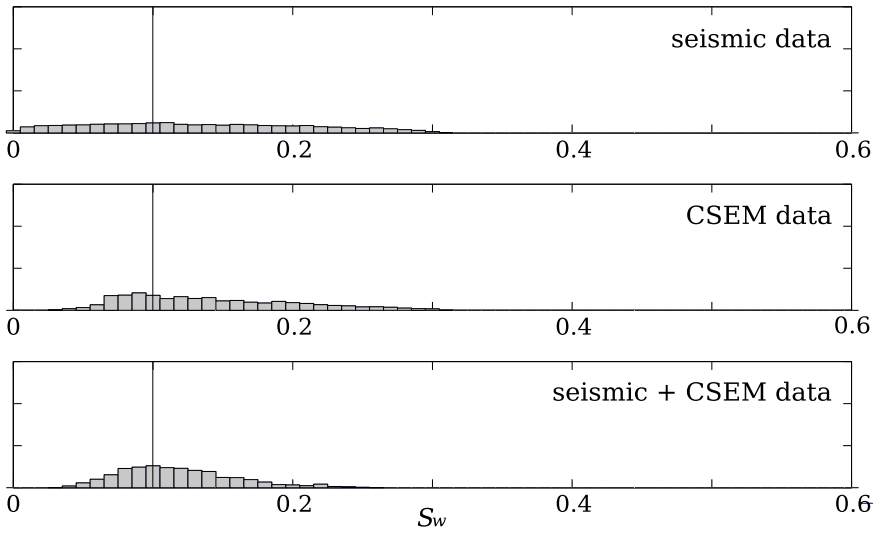

Figure 2.12. Histograms of posterior water saturation (S_w) samples of the sandstone layer. Vertical lines indicate the true water saturation values.

Table 2.2. Two representative uncertainty levels used in the project.

type of uncertainty source	base state variance	reduced state variance
seismic wave velocity	$(0.1\ \mathrm{km/s})^2$	$(0.03\ \mathrm{km/s})^2$
electric conductivity	$(0.1\ \log_{10}(\mathrm{S/m}))^2$	$(0.03\ \log_{10}(\mathrm{S/m}))^2$
seismic noise	$(30\%$ of max. amplitude$)^2$	$(10\%$ of max. amplitude$)^2$
CSEM noise (systematic)	$(5\%$ of each amplitude$)^2$	$(2\%$ of each amplitude$)^2$
CSEM noise (non-systematic)	$(5 \times 10^{-14}\ \mathrm{V/m})^2$	$(2 \times 10^{-14}\ \mathrm{V/m})^2$

subsequent samplings are performed by the algorithm summarized in Appendix A. An example of the random sampling is shown in Figure 2.9, which shows subsequent samples of the water saturation of the sandstone layer. In the given example, the initial sample is far away from the range of the posterior distribution, and the initial movement of random samples toward posterior distribution, the burn-in stage, is clearly shown (shaded area). We exclude those samples from assessing the posterior distribution. For the diagnosis of the convergence of the random sampling toward the posterior distribution, we monitor the variance of the random samples as a function of total number of samples (Figure 2.10). For sufficiently large sampling number n, the variance of the random samples converges, and we use this value for the variance of the posterior distribution.

The random samples of the porosity and water saturation are drawn from the posterior probability distribution of three different cases: using seismic data only, using CSEM data only, and using both seismic and CSEM data. The uncertainty levels applied to the comparison are summarized as the base state variances in Table 2.2. The posterior distributions of the porosity and water saturation of the target sandstone layer are summarized as histograms as shown in Figures 2.11 and 2.12. Note that for the given uncertainties of rock-physics model and data noise levels, the

histograms show that the models based on seismic data or CSEM data alone weakly constrain porosity and water saturation. However, the histograms from the joint interpretation exhibit a narrower sample distribution of the porosity and water saturation. The figures also show that the seismic data is more sensitive to the porosity than to the water saturation. This is partly due to the rock-physics models in Figures 2.3 and 2.4 which show that the P-wave velocity has weaker correlation with the water saturation than with porosity. The relatively poor resolution from the CSEM data is attributed to the fact that the sandstone layer is electrically shielded by the more conductive overburden (soft shale layer). These examples illustrate the strength and limitation of both seismic and CSEM methods and explain the motivation of the joint interpretation of seismic and CSEM data. The histograms of the joint interpretation show smaller posterior uncertainty than do the single interpretations. The reduction of uncertainty is more pronounced for water saturation than for porosity.

Next we compare the histograms that describe the posterior probabilities of different layers. Figure 2.13 shows the joint posterior distributions of the porosity of three layers. The posterior distribution for the soft shale layer is less constrained than that of the other layers. This is a consequence of the relatively weak correlation between the porosity and P-wave velocity of the soft shale layer (Figure 2.3). Despite the stronger sensitivity of the seismic and CSEM methods on the properties of the uppermost layer, the weaker correlations of the rock-physics model cause larger variance of the porosity samples. The joint posterior distributions of the water saturation (Figure 2.14) also exhibit that the posterior distribution for the soft shale layer is less constrained than for the sandstone layer and that the rock-physics model uncertainty has more significance on constraining the posterior distribution than the resolution of the seismic and CSEM methods.

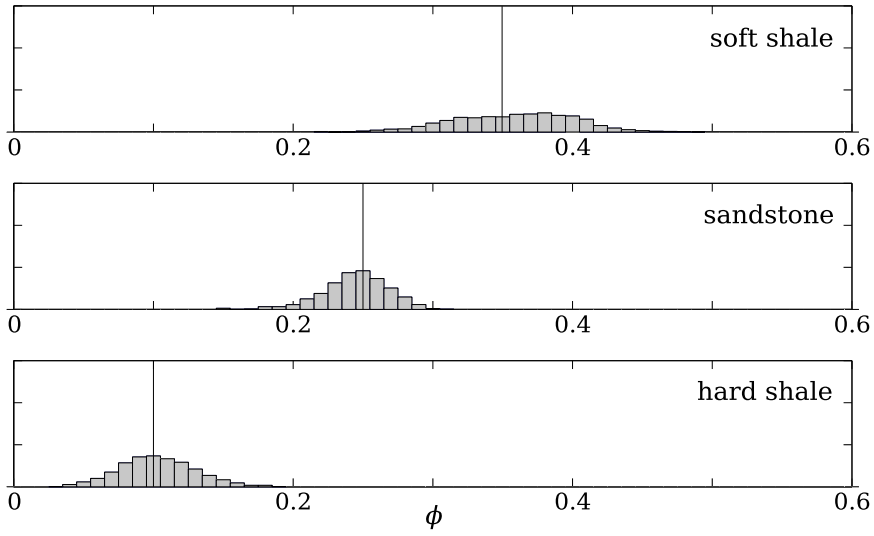

Figure 2.13. Histograms of posterior porosity (ϕ) samples of the three layers obtained from joint inversion of seismic and CSEM data (base uncertainty level). Vertical lines indicate the true porosity values.

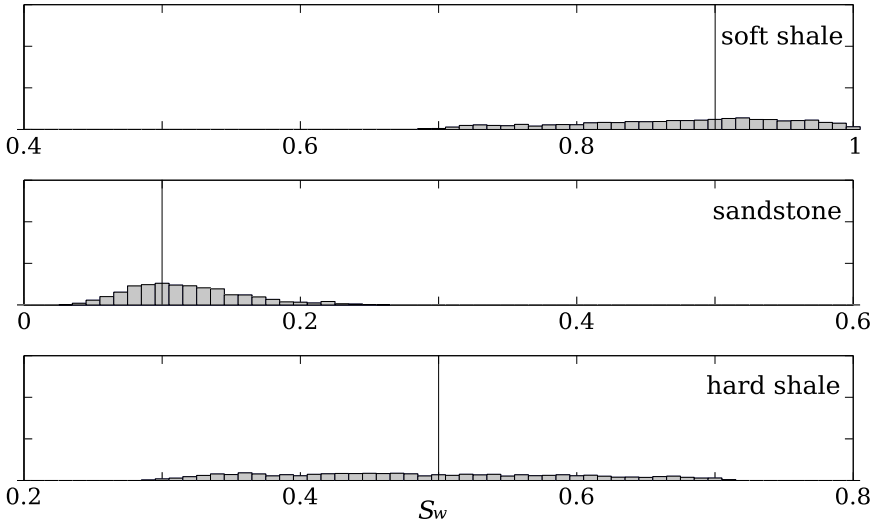

Figure 2.14. Histograms of posterior water saturation (S_w) samples of the three layers obtained from joint inversion of seismic and CSEM data (base uncertainty level). Vertical lines indicate the true water saturation values.

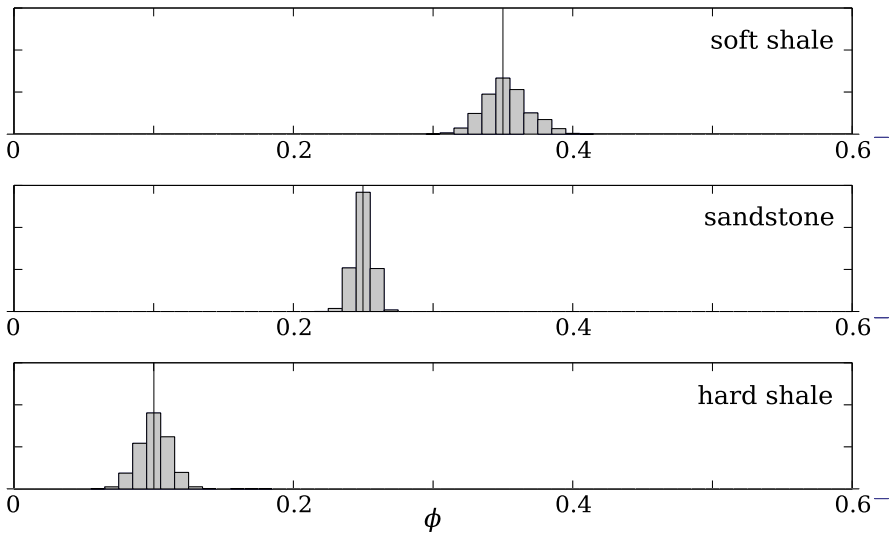

Figure 2.15. Histograms of posterior porosity (ϕ) samples of the three layers obtained from joint inversion of seismic and CSEM data (reduced uncertainty level). Vertical lines indicate the true porosity values.

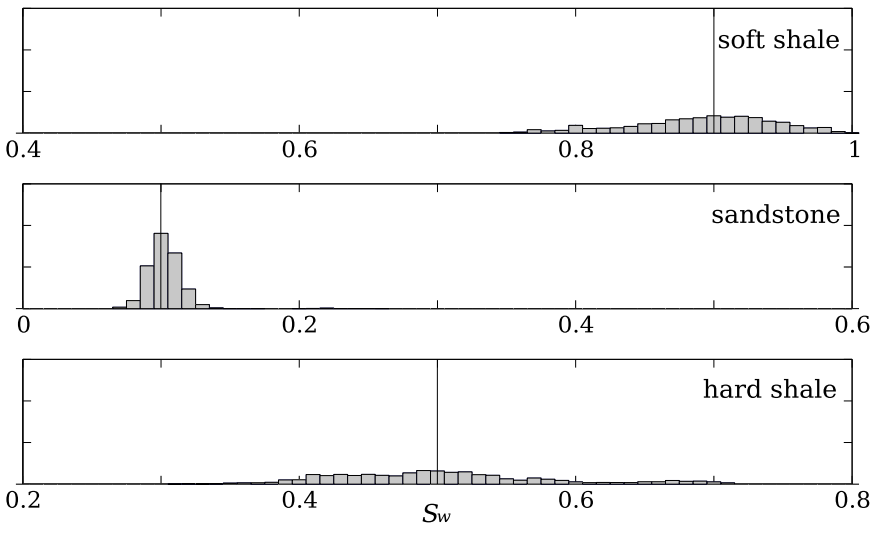

Figure 2.16. Histograms of posterior water saturation (S_w) samples of the three layers obtained from joint inversion of seismic and CSEM data (reduced uncertainty level). Vertical lines indicate the true water saturation values.

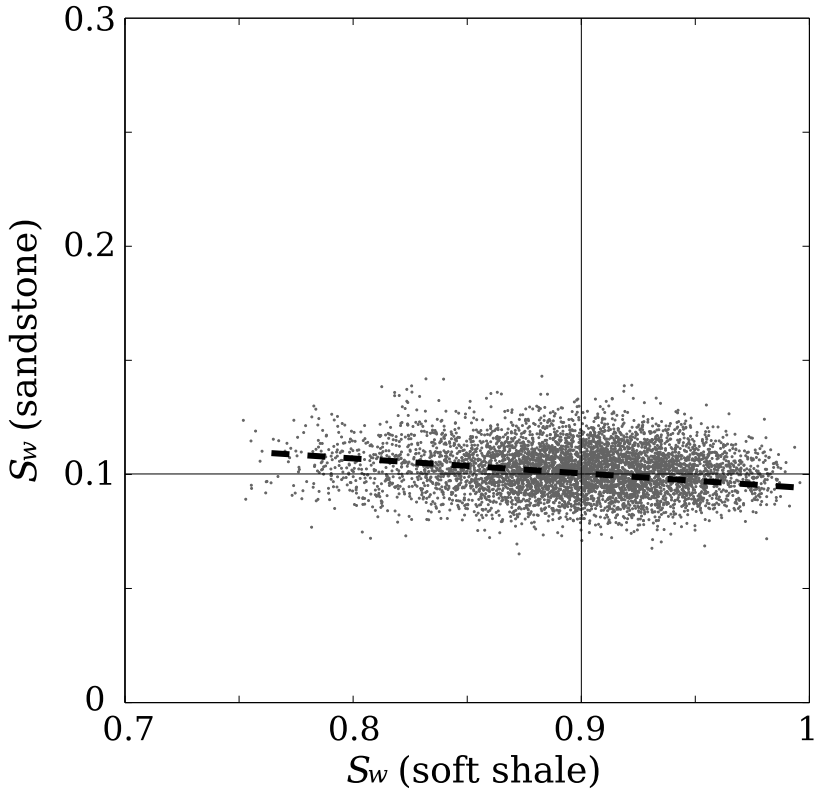

Figure 2.17. Crossplot of posterior water saturation samples of the soft shale and sandstone layers. The histograms of the corresponding samples are shown in Figure 2.16. The vertical and horizontal lines indicate the true water saturation values. The correlation coefficient between the two random variables is negative (dashed line).

Finally, we study two representative uncertainty levels: a base state and a new state with reduced data uncertainties (Table 2.2). Note that the uncertainty of the electric conductivity is defined on a logarithmic scale. The seismic data uncertainty is defined as a ratio from the maximum amplitude value, and the CSEM data uncertainty is defined as a sum of systematic and non-systematic noise. Figures 2.13 and 2.14 represent the posterior probability for the base uncertainty level. The histograms for the reduced uncertainty level are shown in Figures 2.15 and 2.16. The reduced uncertainty level leads, of course, to a sharper posterior probability distribution than the base state and thus increases the accuracy in the estimates of porosity and water saturation. This stronger constraint is more obvious for porosity than for water saturation. This is due to the smaller resolution of the CSEM method compared to the seismic method.

The correlation of reservoir parameters between different layers can be studied by crossplot analysis. An example of the crossplot analysis is shown in Figure 2.17, where the posterior water saturation samples of the soft shale and sandstone layers are crossplotted. The example demonstrates that the water saturation of the two layers has negative correlation, which arises from the weak depth resolution of the CSEM exploration. Therefore, the correlation between the two layers becomes weaker as the thickness of the sandstone layer increases. The weaker correlation of a reservoir parameter between different layers generally accompanies reduced uncertainty of the reservoir parameter. The correlation analysis can help diagnose the trade-off between different model parameters.

2.5.2 Different scenarios for uncertainty reduction

In the previous section, we presented histograms that characterize the posterior uncertainty. As stated before, we assume the multivariate Gaussian distribution (equation (2.4)) for the calculation of prior and likelihood. There are however several factors that make the distribution of the posterior samples non-Gaussian. First, the porosity or water saturation have values between 0 and 1. Second, the porosity sampling is bounded by the critical porosity ϕ_c. The critical porosity is the threshold value between the suspension and the load-bearing domain and denotes the upper porosity limit of the range where the rock-physics model can be applied (Mavko *et al.*, 1998). The critical porosity values we apply for the soft shale, sandstone, and hard shale layer are 0.6, 0.4, and 0.4, respectively. These bounds can lead to skewed sample distributions. Furthermore the posterior distributions do not necessarily follow the Gaussian distribution because of the nonlinearity of the forward models. The posterior uncertainty can generally be assessed by sample mean and sample variance. For reasons of clarity, we use the Gaussian curves for the representation of the sample mean and sample variance.

In this project, we model four factors of uncertainty: rock-physics model uncertainties of the P-wave velocity and electric conductivity, and noise of the seismic and CSEM data. We discussed the posterior probabilities of the porosity and water saturation for the base and reduced uncertainty levels (Table 2.2) in the previous section (Figures 2.13 - 2.16). We perform the following numerical experiments to quantify the contributions of the four possible sources of uncertainty. The initial simulation is performed based on the base uncertainty level. For analysis of the contributions of each of the factors on the posterior uncertainties, six subsequent simulations are performed with reduced uncertainty levels of one or two of the four factors of uncertainty.

Table 2.3. Eight numerical experiments for the analysis of the contributions of four possible factors of uncertainty. Two states of uncertainty for the individual factors are listed in Table 2.2.

	uncertainty of the individual factors
base level	none of the factors are reduced
treatment-1	only reducing P-wave velocity uncertainty
treatment-2	only reducing electric conductivity uncertainty
treatment-3	only reducing seismic noise level
treatment-4	only reducing CSEM noise level
treatment-5	reducing P-wave velocity uncertainty and seismic noise level
treatment-6	reducing electric conductivity uncertainty and CSEM noise level
reduced level	reducing all of the four uncertainty factors

We perform the last simulation based on reduced uncertainty levels of all factors of uncertainty (reduced level). These eight numerical experiments are summarized in Table 2.3. We compare the posterior distributions from different treatments with the base and reduced levels, and deduce how much a treatment contributes to the overall change of the sample variances. The posterior distributions of the porosity and water saturation are shown in Figures 2.18 - 2.23.

Figures 2.18 and 2.19 show the posterior probability distributions acquired after performing the treatments 1 and 2. When we reduce uncertainty levels of P-wave velocity or electric conductivity, the resultant posterior distributions exhibit smaller sample variances than the base level. Furthermore, the sample means generally are closer to the modeled values as we reduce the individual uncertainty levels. The probability density distribution for porosity of the sandstone layer (Figure 2.18) reveals that the P-wave velocity uncertainty plays a significant role on the overall uncertainty

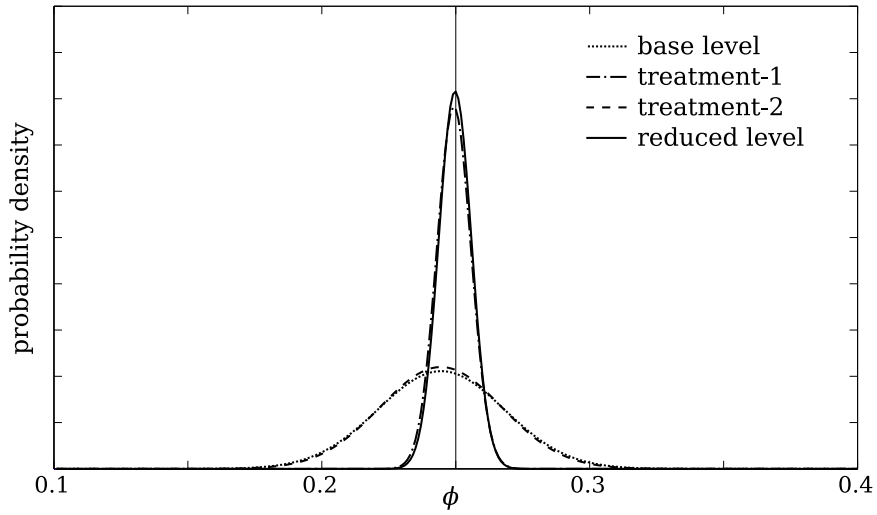

Figure 2.18. Posterior probability distributions of porosity ϕ of the sandstone layer. The distributions from the treatments 1 and 2 (Table 2.3) are compared with those from the base and reduced levels. Vertical line indicates the true porosity value.

reduction of the porosity and the contribution of the electric conductivity uncertainty is limited. In contrast, Figure 2.19 shows that the overall uncertainty variation of the water saturation is more strongly influenced by the uncertainty of the electric conductivity than by the uncertainty of the P-wave velocity. This is consistent with the simulated rock-physics models shown in Figures 2.3 - 2.6. From the rock-physics models, we can deduce that the porosity strongly influences both the P-wave velocity and electric conductivity. The rock-physics models also show that the water saturation strongly influences the electric conductivity while its influence on the P-wave velocity is limited.

The posterior probability distributions for the treatments 3 and 4 are shown in Figures 2.20 and 2.21. When we reduce the noise levels of the seismic or CSEM data, the improvements of the posterior uncertainties of the porosity and water saturation are much less significant than the improvements due to the reduction of rock-physics

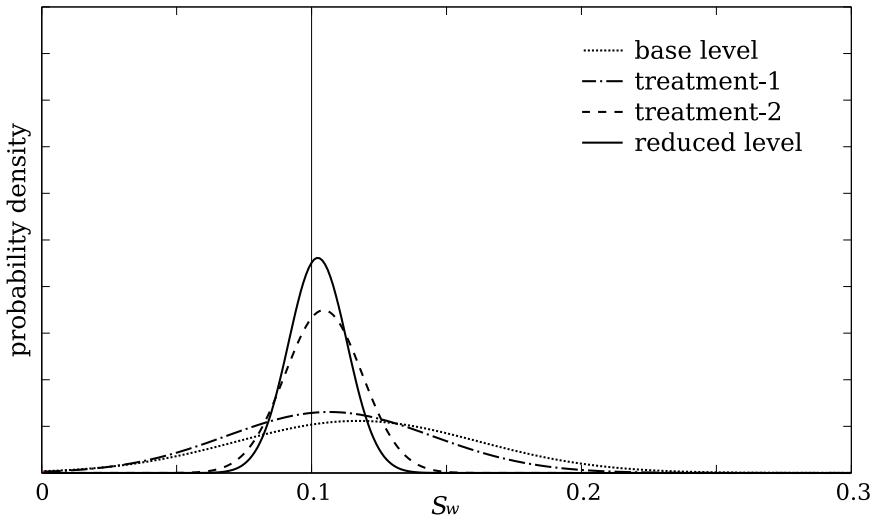

Figure 2.19. Posterior probability distributions of water saturation S_w of the sandstone layer. The distributions from the treatments 1 and 2 (Table 2.3) are compared with those from the base and reduced levels. Vertical line indicates the true water saturation value.

model uncertainties. This shows that the overall uncertainty of the porosity and water saturation is more influenced by the rock-physics model uncertainties than by the noise of the seismic or CSEM data. The figures also show that for the given range of data noise, the seismic data noise reduction yields a more precise estimate than when the CSEM data noise is reduced.

Figures 2.22 and 2.23 show the posterior probability distributions for the treatments 5 and 6. Compared to the single improvement cases, it is clear that the combined improvements give better assessments about the porosity and water saturation. The probability density distributions shown in Figures 2.22 and 2.23 are similar to the distributions shown in Figures 2.18 and 2.19. This implies that the posterior uncertainty variations from the combined improvements are mainly governed by the improvement of rock-physics model uncertainties and the contributions of the seismic

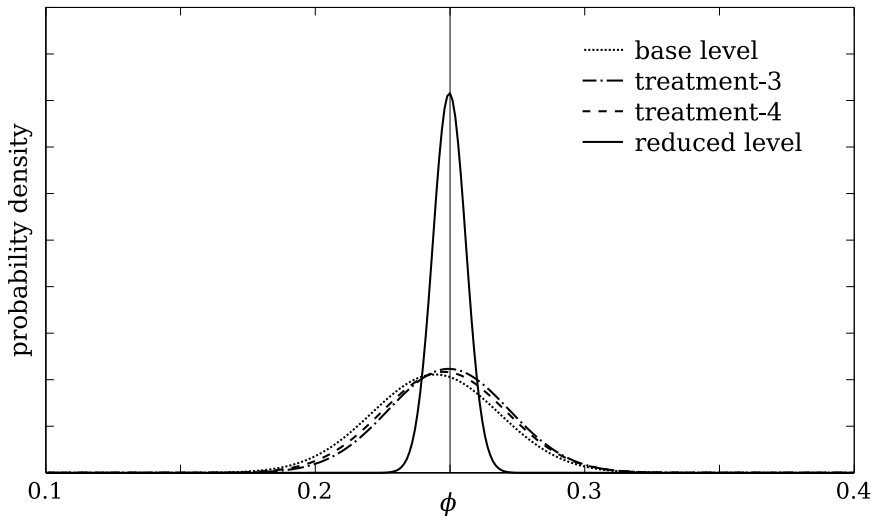

Figure 2.20. Posterior probability distributions of porosity ϕ of the sandstone layer. The distributions from the treatments 3 and 4 (Table 2.3) are compared with those from the base and reduced levels. Vertical line indicates the true porosity value.

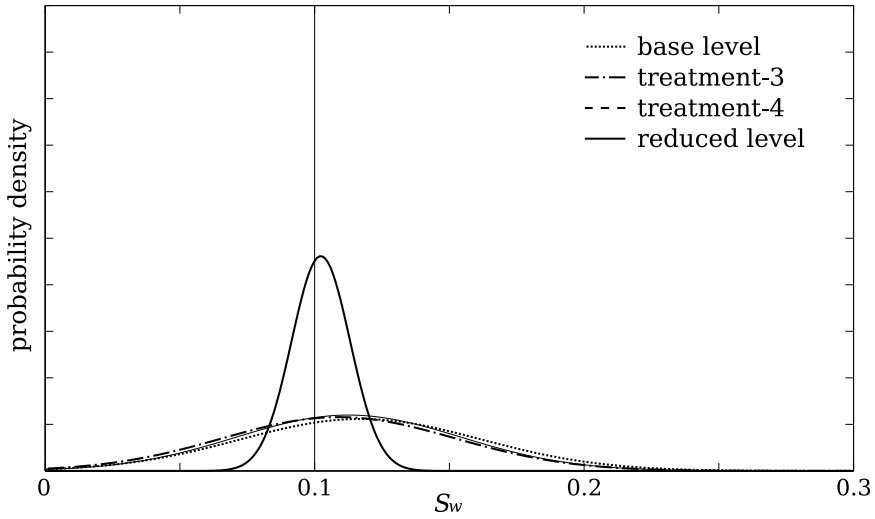

Figure 2.21. Posterior probability distributions of water saturation S_w of the sandstone layer. The distributions from the treatments 3 and 4 (Table 2.3) are compared with those from the base and reduced levels. Vertical line indicates the true water saturation value.

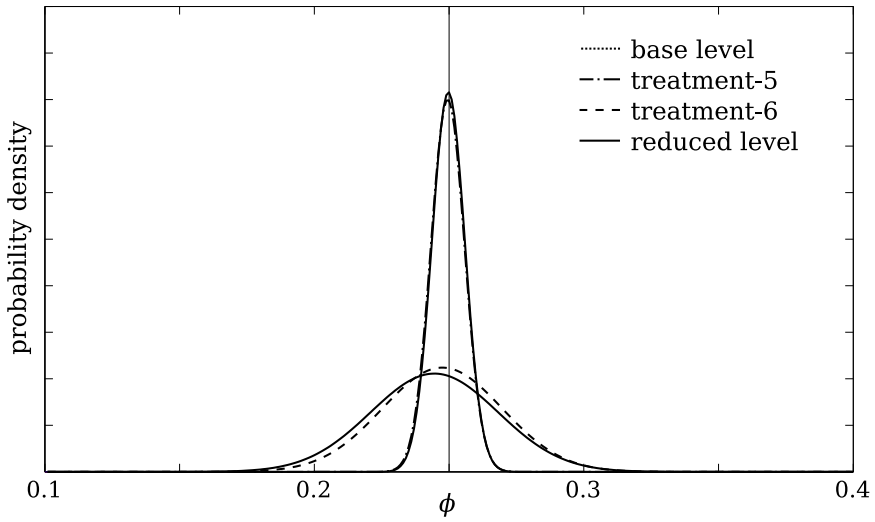

Figure 2.22. Posterior probability distributions of porosity ϕ of the sandstone layer. The distributions from the treatments 5 and 6 (Table 2.3) are compared with those from the base and reduced levels. Vertical line indicates the true porosity value.

and CSEM data noise are less significant.

The posterior probability distributions shown in Figures 2.18 - 2.23 are summarized in Table 2.4. The comparison of the variance values clearly show that the reductions of the sample variances of the porosity and water saturation are most strongly influenced by the uncertainty of the P-wave velocity and electric conductivity, respectively. The contributions of the rock-physics model uncertainties on the posterior uncertainties are generally larger than those of the seismic and CSEM data noise. The numerical experiments suggest different ways of accomplishing uncertainty reduction depending on whether our interests focus on the porosity or water saturation. When porosity is our prime concern, we can effectively accomplish uncertainty reduction by improving the P-wave velocity model and by suppressing the seismic data noise. On the other hand, if we need more accurate assessment of water saturation, the acquisition of more detailed electric conductivity information and the

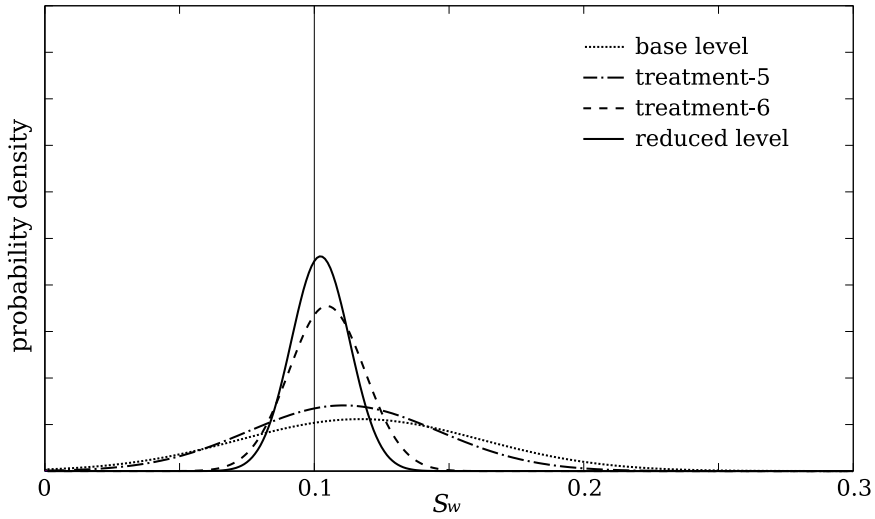

Figure 2.23. Posterior probability distributions of water saturation S_w of the sandstone layer. The distributions from the treatments 5 and 6 (Table 2.3) are compared with those from the base and reduced levels. Vertical line indicates the true water saturation value.

Table 2.4. Sample variances S^2 of porosity ϕ and water saturation S_w of the sandstone layer. The details about the treatments are in Table 2.3.

sample variance ($\times 10^{-3}$)	$S^2(\phi)$	$S^2(S_w)$
base level	0.560	1.997
treatment-1	0.041	1.456
treatment-2	0.516	0.205
treatment-3	0.501	1.865
treatment-4	0.532	1.728
treatment-5	0.039	1.251
treatment-6	0.498	0.198
reduced level	0.038	0.117

suppression of CSEM data noise is preferred.

Note that the above assessments are based on marginal analysis of posterior probability, and possible correlation between different uncertainty factors are ignored. This can be misleading in the presence of strong correlation. The correlation between uncertainty factors can be analyzed by the full factorial experiment (Fisher *et al.*, 1990) that requires 2^n treatments, where n is the number of uncertainty factors.

2.6 Conclusions

We have shown that the posterior probability random sampling based on the Metropolis-Hastings algorithm is capable of assessing the multi-dimensional probability distribution of porosity and water saturation. We have also shown that the joint inversion of the seismic and CSEM data can be achieved by introducing rock-physics models that interconnect the P-wave velocity and electric conductivity. There are four representative sources of uncertainty that influence the posterior probability density of porosity and water saturation. These uncertainties are related to seismic wave velocity, electric conductivity, seismic data, and CSEM data. Even when single interpretations poorly constrain the posterior distributions of porosity and water saturation, the distributions from the joint interpretation are well constrained and exhibit reduced uncertainty.

Assuming two levels of overall uncertainty, we study the relative contributions from the four individual sources of uncertainty. The numerical simulations show that rock-physics model uncertainties play a more significant role on the overall uncertainty variation than do seismic and CSEM data noise. The numerical experiment also suggests different ways of accomplishing uncertainty reduction depending on whether our interests focus on porosity or on water saturation. When porosity is our prime

concern, we can effectively accomplish uncertainty reduction by acquiring more precise P-wave velocity information and suppressing the seismic data noise. On the other hand, if we need a more accurate assessment of water saturation, the acquisition of more detailed electric conductivity information and the suppression of CSEM data noise are desirable.

We emphasize that the conclusions explained above depend on the parameters chosen in this project. Furthermore, there are many sources of uncertainty that we do not take into account such as lithological variations, variation of mineralogical composition of clay, and depth of layers. If we include more of the data uncertainties, the balance between the uncertainties in the seismic wave velocity or electric conductivity and seismic or CSEM data noise can, therefore, be changed. The methodology of the uncertainty analysis presented in this project can, however, be extended to include those parameters and their uncertainties. The employed method can be used for experimental design and for targeting the source of the error that contributes most to the posterior uncertainty.

2.7 Acknowledgments

This work was supported by the Consortium Project on Seismic Inverse Methods for Complex Structures at Center for Wave Phenomena (CWP). We thank Alan D. Chave (Woods Hole Oceanographic Institution) for providing his CSEM code, which was critically important for the success of this study. We acknowledge Inge Myrseth (Norwegian University of Science and Technology), Malcolm Sambridge (Australian National University), Albert Tarantola (Institut de Physique du Globe de Paris), Luis Tenorio, Mike Batzle, André Revil, Misac Nabighian, Steve Hill (Colorado School of Mines) for helpful information, discussions, and suggestions. We are also grateful to

colleagues at CWP for valuable discussions and technical help.

Chapter 3

CONVERGENCE ANALYSIS OF SCATTERING SERIES ACOUSTIC WAVE PROPAGATION VS. ELECTROMAGNETIC DIFFUSION

3.1 Summary

The inverse scattering series is a tool that can effectively resolve the nonlinearity of an inverse problem. The geophysical application of the inverse scattering series has focused previously on seismic exploration, in particular on velocity estimation and multiple suppressions. However, the inverse scattering series has not been widely applied to the interpretation of electromagnetic data. We study the feasibility of this application. Compared to seismic exploration, electromagnetic methods are characterized by a rapid spatial decay of the probing field and a strong perturbation of the medium parameters. We focus on identifying the difference between the convergence patterns of the scattering series for acoustic wave and electromagnetic diffusion problems. As a prototype of the forward and inverse scattering series, we analyze the 3D Green function for homogeneous media. The analysis shows that for electromagnetic diffusion, the reference medium should be sufficiently conductive to allow convergence of the forward scattering series. The analysis also illustrates that the rapid spatial decay of a diffusive field does not necessarily mean fast convergence of the scattering series. However, model tests with parameters representing geophysical exploration of hydrocarbon reservoirs suggest that the convergence of the scattering series for elec-

tromagnetic diffusion is faster than that for acoustic wave propagation. The model tests also show that for the diffusion equation, one can improve the convergence of the inverse scattering series by choosing a reference medium that is less conductive than the true medium. This research provides insights into the convergence requirements of the scattering series and guidelines for further application of the inverse scattering series to the interpretation of electromagnetic data.

3.2 Introduction

The goal of inverse scattering problems is to obtain a quantitative description of an unknown scatterer from knowledge of the scattering data. The inverse scattering theory originates from inverse problems in quantum scattering theory and formal solutions of inverse scattering problems (Gel'fand & Levitan, 1951; Jost & Kohn, 1952; Moses, 1956; Prosser, 1969). The inverse scattering series describes a model perturbation as a series in order of a scattered field. The inverse scattering series has been applied to seismic exploration for reconstructing subsurface velocity (Weglein *et al.*, 1981) and attenuating multiples in seismic reflection data (Weglein *et al.*, 1997, 2003). The main advantage of the inverse scattering series is that no *a priori* knowledge of the subsurface (e.g., velocity) is assumed and all refraction, diffraction, and multiple reflection phenomena are, in principle, taken into account. Recent studies show that the inverse scattering series can be applied to diverse seismic problems that include imaging, direct nonlinear inversion, data reconstruction, and wavefield separation (Ramirez & Weglein, 2009; Weglein *et al.*, 2009; Zhang & Weglein, 2009a,b).

Scattering theory relates the scattered field G^s (the difference between the true and reference fields) to the perturbation P (the difference between their corresponding medium properties). The forward scattering series, which is also known as the Born

or Neumann series (Weglein *et al.*, 1997), describes the scattered field G^s as a series in order of the perturbation P:

$$G^s = G_1^s + G_2^s + G_3^s + \cdots , \tag{3.1}$$

where G_n^s is the portion of the scattered field that is the nth order of the perturbation. On the other hand, the inverse scattering series expands the perturbation P as a series in order of the scattered field G^s:

$$P = P_1 + P_2 + P_3 + \cdots , \tag{3.2}$$

where P_n is the portion of the perturbation that is the nth order of the scattered field. In equation (3.2), P_1 is the portion of P that is linear in the scattered field. In fact, only the linear component in the scattered field ultimately contributes to the reconstruction of the model, and the nonlinear components are being subtracted in the inversion (Snieder, 1990a,b). The inverse scattering series effectively incorporates the nonlinearity of an inverse problem. Generally, the series expressions in equations (3.1) and (3.2) converge within a finite range of perturbation or scattered field (radius of convergence) (Prosser, 1969). When these series converge, one only requires the Green function of the reference medium and the scattered field for the reconstruction of the perturbation.

Marine electromagnetic surveys are useful complementary tools to seismic surveys in searching for a hydrocarbon reservoir (Constable & Srnka, 2007; Hu *et al.*, 2009; Kwon & Snieder, 2011b) because electromagnetic data can provide more decisive information about the reservoir composition than seismic data. The electromagnetic field is sensitive to the electric conductivity, which is predominantly influenced by

water content within the subsurface: increasing water content causes larger conductivity, and hydrocarbons, whether gas or petroleum, are poor electric conductors. The significant difference of electric conductivity in water and hydrocarbon makes the electromagnetic surveys ideal tools for distinguishing a hydrocarbon reservoir from a water saturated reservoir. Inverse problems of the electromagnetic surveys are strongly-nonlinear (Parker, 1977; Snieder, 1998), and the inverse scattering series can thus be useful for the inverse problems. However, the geophysical application of the inverse scattering series has focused previously on seismic exploration, and the inverse scattering series has not been widely applied to the interpretation of electromagnetic data. We study the feasibility of this application by a comparative analysis of the scattering series between seismic and electromagnetic exploration.

In geophysical applications, electromagnetic fields propagate as waves in a high frequency range (i.e., ground penetrating radar) or in an insulating medium (i.e., air). For most earth materials and frequencies of electromagnetic methods used in hydrocarbon exploration, diffusion is dominant and the contribution of wave propagation is negligible (Chave & Cox, 1982). In contrast, seismic exploration is always governed by wave propagation. Seismic exploration is performed over a scale of many wavelengths, whereas electromagnetic fields exhibit rapid spatial decay and diffuse over a few skin depths that describe the length scale where the amplitude decays to e^{-1} Jackson (1999). The seismic and electromagnetic surveys involve different data acquisition geometries, and noise statistics of marine electromagnetic data is different from that of seismic data (Kwon & Snieder, 2011b). Furthermore, the strength of the medium perturbation in electromagnetic exploration is stronger than that in seismic exploration. In other words, the range of the electric conductivity in the subsurface is generally wider than the range of seismic wave velocity (Palacky, 1987; Mavko *et al.*,

1998). Among many differences between seismic and electromagnetic exploration, we focus on two distinguishing features of electromagnetic exploration, i.e., diffusive probing field and strong perturbation. We also take acoustic wave propagation as a norm of seismic wave propagation. In this study, we analyze convergence conditions of the scattering series for acoustic wave propagation and electromagnetic diffusion and study the feasibility of applying the inverse scattering series to electromagnetic exploration.

In the following, we adopt mathematical prototypes of the wave and diffusion equations within a homogeneous medium, and identify medium properties that affect acoustic wave propagation and electromagnetic diffusion in the subsurface. We consider two different states of the infinite homogeneous medium, relate the scattered field G^s and perturbation P via the 3D Green functions of the homogeneous media, and formulate the forward and inverse scattering series. We thereafter analyze the convergence conditions of these formal series expressions and discuss the difference between the convergence conditions for acoustic wave and electromagnetic diffusion equations. Finally, we apply parameters representing geophysical exploration of hydrocarbon reservoirs, estimate the source-receiver offset range where the series converge, and discuss the feasibility of applying the inverse scattering series to electromagnetic exploration.

3.3 Formulation of scattering series

Consider the following differential equations as governing equations for true and reference media:

$$L(\mathbf{r};\omega)\, G(\mathbf{r},\mathbf{r}_s;\omega) = -\delta(\mathbf{r}-\mathbf{r}_s), \tag{3.3}$$

$$L_0(\mathbf{r};\omega)\, G_0(\mathbf{r},\mathbf{r}_s;\omega) = -\delta(\mathbf{r}-\mathbf{r}_s), \tag{3.4}$$

where L, L_0 and G, G_0 are the true and reference differential operators and Green functions, respectively, for an angular frequency ω, $\delta(\mathbf{r}-\mathbf{r}_s)$ is the Dirac delta function, and $\mathbf{r}$ and $\mathbf{r}_s$ are the receiver and source locations, respectively. The information about the true and reference media properties is encapsulated in L and L_0. The scattered field is the difference between the two Green functions:

$$G^s(\mathbf{r},\mathbf{r}_s;\omega) = G(\mathbf{r},\mathbf{r}_s;\omega) - G_0(\mathbf{r},\mathbf{r}_s;\omega). \tag{3.5}$$

The perturbation P is defined as the difference between two differential operators (Weglein *et al.*, 1997, 2003):

$$P(\mathbf{r};\omega) = L(\mathbf{r};\omega) - L_0(\mathbf{r};\omega). \tag{3.6}$$

For heterogeneous media, the Lippmann-Schwinger equation (Lippmann & Schwinger, 1950; Colton & Kress, 1998) relates the scattered field and perturbation, and the forward and inverse scattering series involve iterative evaluation of integral equations (Prosser, 1969; Weglein *et al.*, 2003). In this study, we consider two homogeneous media, which allow one to relate the scattered field and perturbation via analytic solution of the Green function. We use the Taylor series to expand the scattered field

and perturbation in order of the perturbation and scattered field, respectively, and study the convergence conditions of the forward and inverse scattering series.

The Helmholtz equation describes acoustic wave propagation and electromagnetic diffusion within a homogeneous medium:

$$L(\omega)\, G(\mathbf{r}, \mathbf{r}_s; \omega) = (\nabla^2 + k^2)\, G(\mathbf{r}, \mathbf{r}_s; \omega) = -\delta(\mathbf{r} - \mathbf{r}_s). \tag{3.7}$$

The wavenumber k is given as

$$k^2 = \begin{cases} \omega^2/c^2 & \text{(acoustic wave propagation)}, \\ i\omega/d = i\omega\mu\sigma & \text{(electromagnetic diffusion)}, \end{cases} \tag{3.8}$$

where c is the acoustic wave velocity (m/s), d the electromagnetic diffusivity (m^2/s), μ the magnetic permeability ($\mathrm{N/A}^2$), and σ the electric conductivity (S/m), respectively (Jackson, 1999). Magnetizable materials are rare in the subsurface (Chave & Cox, 1982), and we take the magnetic permeability μ to be the free space value. We also assume that the acoustic wave velocity c and electromagnetic diffusivity d are real, which implies that the wavenumber k is real for the wave equation and complex for the diffusion equation. The perturbation is described in terms of the acoustic wave velocity c and electric conductivity σ in this study.

3.3.1 Forward scattering series

Given a source at the origin, the 3D Green function for the Helmholtz equation is (Morse & Feshbach, 1953)

$$G(\mathbf{r}) = \frac{1}{4\pi r} e^{ikr}, \tag{3.9}$$

where $r = |\mathbf{r}|$. We denote the wavenumbers of the true and reference media as k and k_0, respectively. From equations (3.6) and (3.7), the perturbation is defined as

$$P = k^2 - k_0^2, \tag{3.10}$$

and the wavenumber of the true medium is expressed as

$$k = k_0\sqrt{1 + \frac{P}{k_0^2}}. \tag{3.11}$$

Equations (3.5), (3.9), and (3.11) yield the scattered field as follows:

$$G^s(\mathbf{r}) = \frac{1}{4\pi r}\left[\exp\left(ik_0 r\sqrt{1 + \frac{P}{k_0^2}}\right) - \exp\left(ik_0 r\right)\right]. \tag{3.12}$$

The forward scattering series expresses the scattered field $G^s(\mathbf{r})$ as a series in order of the perturbation P. Note that a function of a complex variable z, $f(z) = \sqrt{1+z}$, has a singular point (branch point) at $z = -1$, and the radius of convergence of the Taylor series expansion around $z = 0$ extends up to the singular point. The series for the exponential is absolutely convergent. Therefore, equation (3.12) shows that the forward scattering series converges only for small perturbations compared to the reference medium properties such that

$$\left|\frac{P}{k_0^2}\right| < 1. \tag{3.13}$$

Equation (3.13) resembles the convergence condition of the forward series for the scattering of an acoustic wave function from a variable index of refraction (Prosser, 1976). In that previous study, the perturbation is represented as $k_0^2 W(\mathbf{r})$ with $W(\mathbf{r})$

denoting the variable index of refraction, and the convergence criterion is given as $|W(\mathbf{r})| < 1$. Note that we formulate the forward scattering series via the Taylor series and deduce a convergence condition that is equivalent to that from the integral equation approach. Combining equations (3.8), (3.10), and (3.13) provides the following convergence criteria for acoustic wave propagation and electromagnetic diffusion:

$$\begin{cases} c > c_0/\sqrt{2} & \text{(acoustic wave equation)}, \\ \sigma < 2\,\sigma_0 & \text{(electromagnetic diffusion equation)}. \end{cases} \tag{3.14}$$

In other words, the reference medium should have sufficiently a small acoustic wave velocity to yield a converging forward series for acoustic wave propagation. For electromagnetic diffusion problems, we need to choose a sufficiently conductive reference model to achieve convergence of the forward series.

Denoting two complex quantities, $ik_0 r$ and P/k_0^2, as a and z, we express equation (3.12) as

$$G^s(\mathbf{r}) = G_0(\mathbf{r})F(z), \tag{3.15}$$

where $F(z)$ is a complex function:

$$F(z) = \exp\left(a\sqrt{1+z} - a\right) - 1. \tag{3.16}$$

As shown in Appendix C, the nth order derivative of $F(z)$ is

$$\frac{d^n F}{dz^n} = \frac{1}{2^n}\sum_{m=1}^{n} \beta_{n,m} a^{n-m+1}(1+z)^{-\frac{n+m-1}{2}} \exp\left(a\sqrt{1+z} - a\right), \tag{3.17}$$

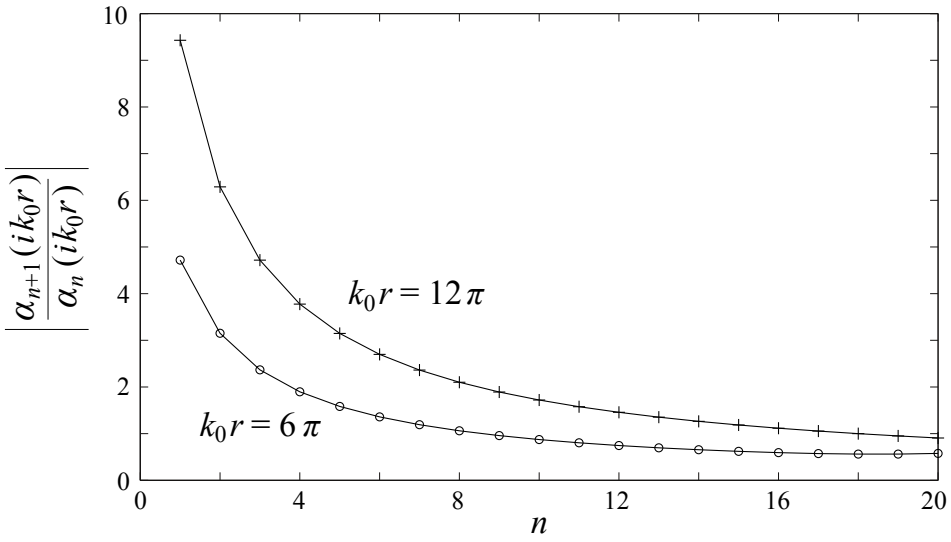

Figure 3.1. Convergence rate of forward scattering series. The ratio $|\alpha_{n+1}/\alpha_n|$ in equation (3.21) for increasing number of n is compared at two spatial locations: one is 3 wavelengths apart from the source ($k_0r = 6\pi$) and the other is 6 wavelengths ($k_0r = 12\pi$). The bigger value of $|\alpha_{n+1}/\alpha_n|$ at the larger source-receiver offset suggests that more terms in the forward scattering series are necessary to reach convergence with increasing source-receiver offset.

where

$$\beta_{n,m} = \begin{cases} 1 & (m = 1), \\ -\dfrac{\beta_{n,m-1}}{m-1} \displaystyle\sum_{l=m-1}^{n-1} l & (m = 2, 3, 4, \cdots, n). \end{cases} \tag{3.18}$$

Applying equation (3.17) to the Taylor series expansion of equation (3.12) gives the nth order term in the forward series as

$$G_n^s(\mathbf{r}) = G_0(\mathbf{r})\, \alpha_n(ik_0 r) \left[\frac{P}{k_0^2}\right]^n, \tag{3.19}$$

where $\alpha_n(ik_0 r)$ is an nth order power series of $ik_0 r$:

$$\alpha_n(ik_0 r) = \frac{1}{2^n\, n!} \sum_{m=1}^{n} \beta_{n,m}\, (ik_0 r)^{n-m+1}. \tag{3.20}$$

The convergence rate is, therefore,

$$R_n^F(\mathbf{r}) = \left|\frac{G_{n+1}^s(\mathbf{r})}{G_n^s(\mathbf{r})}\right| = \left|\frac{\alpha_{n+1}(ik_0 r)}{\alpha_n(ik_0 r)}\right| \left|\frac{P}{k_0^2}\right|. \tag{3.21}$$

The above equation shows that R_n^F is proportional to $|P/k_0^2|$, and the forward scattering series converges more rapidly as the perturbation is weaker. To appreciate the contribution of α_{n+1}/α_n on the convergence rate, we consider an acoustic wave problem where the frequency f is 50 Hz, wave velocity c_0 is 3,000 m/s, and wavenumber k_0 is about 0.1 m^{-1} (Table 3.1). Figure 3.1 shows the variation of $|\alpha_{n+1}/\alpha_n|$ at two spatial locations: one is 3 wavelengths apart from the source ($k_0 r = 6\pi$) and the other is 6 wavelengths ($k_0 r = 12\pi$). The figure shows that $|\alpha_{n+1}/\alpha_n|$ is larger for $k_0 r = 12\pi$ than for $k_0 r = 6\pi$, which implies that as the source-receiver offset increases, more terms in the series are necessary to reach convergence.

The formal expression of convergence rate given in equation (3.21) is valid for both the wave and diffusion equations. The wavenumber of the diffusion problem (equation (3.8)) has real and imaginary parts, and the Green function for the diffusion equation generally decays more rapidly than that for the wave equation, which has real wavenumber. However, equation (3.21) indicates that there is no fundamental difference in the convergence rate between the forward scattering series for the diffusion equation and the series for the wave equation. In fact, the rapid spatial decay of a diffusive field does not necessarily mean fast convergence of the scattering series. This counterintuitive behavior of the convergence rate can be comprehended by considering the following three functions: e^x, e^{-x}, and e^{ix}. The three functions exhibit different variations as a function of x, but their Taylor series expansions in the variable x show the same convergence rate. This property of the convergence rate implies that the comparison of the convergence speed between wave propagation and diffusion depends on the specific parameters that we incorporate instead of the difference in the behavior of the physical fields. In the following, we choose representative parameters relevant to hydrocarbon exploration situations and compare the convergence of the forward scattering series for the acoustic wave equation with that for the electromagnetic diffusion equation. The details of the parameters are introduced in the next section.

3.3.2 Inverse scattering series

While the forward scattering series expresses the scattered field $G^s(\mathbf{r})$ as a power series in order of the model perturbation P, the inverse series expresses the model perturbation as a power series in order of the scattered field. Rewriting equation

(3.12), we express the perturbation as a function of the scattered field:

$$P(\mathbf{r}) = -\frac{2ik_0}{r}\ln\left(1+\frac{G^s(\mathbf{r})}{G_0(\mathbf{r})}\right) - \frac{1}{r^2}\left[\ln\left(1+\frac{G^s(\mathbf{r})}{G_0(\mathbf{r})}\right)\right]^2. \tag{3.22}$$

Note that a function of a complex variable z, $f(z) = \ln(1+z)$, is singular at $z = -1$, and the radius of convergence of the Taylor series expansion centered at $z = 0$ extends up to the singular point. Equation (3.22) therefore shows that the inverse scattering series converges only for weak scattered fields that satisfy

$$\left|\frac{G^s(\mathbf{r})}{G_0(\mathbf{r})}\right| = \left|\frac{G(\mathbf{r})}{G_0(\mathbf{r})} - 1\right| = \left|e^{i(k-k_0)r} - 1\right| < 1. \tag{3.23}$$

A previous study that is based on the integral equation approach qualitatively stated that the inverse series converges when the perturbation is sufficiently small (Prosser, 1976). Equation (3.23), on the other hand, is a more quantitative convergence criterion and allows one to predict whether an inverse series converges by comparing the magnitude of the scattered and reference fields.

Denoting a complex variable, G^s/G_0, as z, we abbreviate equation (3.22) as

$$P(\mathbf{r}) = -\frac{2ik_0}{r}F_1(z) - \frac{1}{r^2}F_2(z), \tag{3.24}$$

where

$$F_1(z) = \ln(1+z), \tag{3.25}$$

$$F_2(z) = [\ln(1+z)]^2. \tag{3.26}$$

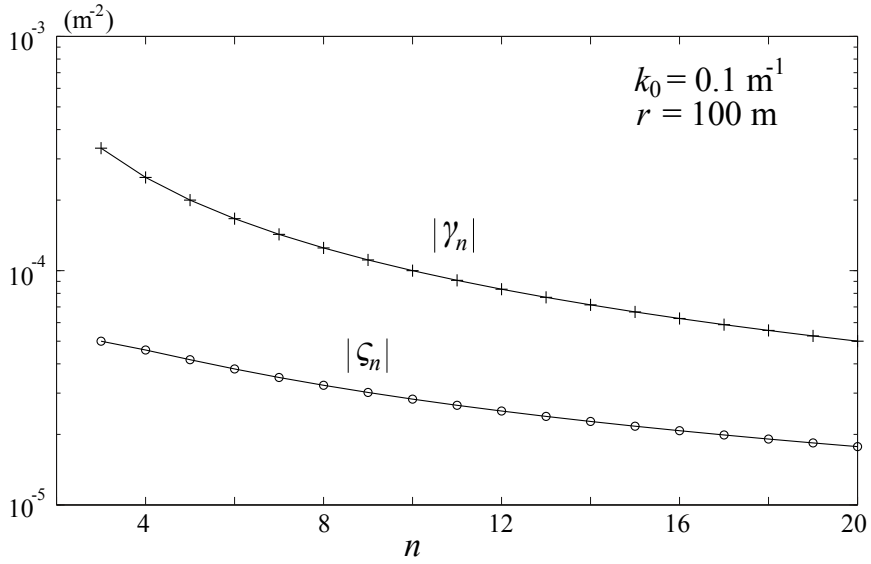

Figure 3.2. Comparison of the absolute values of γ_n and ζ_n in equation (3.30). For $k_0 = 0.1$ m^{-1} and $r = 100$ m, $|\zeta_n|$ is much smaller than $|\gamma_n|$. The two terms are dependent on k_0/r and $1/r^2$, respectively, which implies γ_n is significant at a large source-receiver offset and for a large wavenumber of the reference medium.

The nth order derivative of $F_1(z)$ is

$$\frac{d^n F_1}{dz^n} = (-1)^{n-1}(n-1)!(1+z)^{-n}. \tag{3.27}$$

The nth order derivative of $F_2(z)$ is shown in Appendix E to be

$$\frac{d^n F_2}{dz^n} = -2\eta_n(1+z)^{-n} + 2(-1)^{n-1}(n-1)!\ln(1+z)(1+z)^{-n}, \tag{3.28}$$

where

$$\eta_n = \begin{cases} 0 & (n=1), \\ -(n-1)\eta_{n-1} + (-1)^{n-1}(n-2)! & (n=2,3,4,\cdots). \end{cases} \tag{3.29}$$

Applying equations (3.27) and (3.28) to the Taylor series expansion of equation (3.22) gives the nth order term in the inverse series as

$$P_n(\mathbf{r}) = 2\left[\gamma_n(k_0, r) + \zeta_n(r)\right]\left[\frac{G^s(\mathbf{r})}{G_0(\mathbf{r})}\right]^n, \tag{3.30}$$

where

$$\gamma_n(k_0, r) = (-1)^n \frac{ik_0}{nr}, \tag{3.31}$$

$$\zeta_n(r) = \frac{\eta_n}{n!\, r^2}. \tag{3.32}$$

The above formal expression of the inverse scattering series is valid for both the wave and diffusion equations. Figure 3.2 shows the absolute values of γ_n and ζ_n in equation (3.30). When the wavenumber of the reference medium is $k_0 = 0.1$ m^{-1}, $|\zeta_n|$ is much smaller than $|\gamma_n|$ at $r = 100$ m. The coefficient $|\gamma_n|$ is proportional to k_0/r and $|\zeta_n|$ is to $1/r^2$. Therefore, compared to ζ_n, γ_n is significant at a large source-receiver offset

Table 3.1. Physical parameters adopted for model tests, where c and σ represent acoustic wave velocity and electric conductivity, respectively. Wavenumber k is derived from equation (3.8). The perturbation is real for the acoustic wave problem and imaginary for the electromagnetic diffusion problem.

Acoustic wave propagation		Electromagnetic diffusion	
f	50 Hz	f	10 Hz
c_0	3.0×10^3 m/s	σ_0	1.0×10^{-1} S/m
c	3.3×10^3 m/s	σ	1.0×10^{-2} S/m
k_0^2	1.10×10^{-2} m^{-2}	$\lvert k_0^2 \rvert$	7.90×10^{-6} m^{-2}
k^2	0.91×10^{-2} m^{-2}	$\lvert k^2 \rvert$	0.79×10^{-6} m^{-2}
$P = k^2 - k_0^2$	-0.19×10^{-2} m^{-2}	$\lvert P \rvert = \lvert k^2 - k_0^2 \rvert$	7.11×10^{-6} m^{-2}

and for a large wavenumber of the reference medium. Ignoring ζ_n, we approximate the convergence rate of the inverse scattering series as

$$R_n^I = \left| \frac{P_{n+1}(\mathbf{r})}{P_n(\mathbf{r})} \right| \simeq \left| \frac{\gamma_{n+1}}{\gamma_n} \frac{G^s(\mathbf{r})}{G_0(\mathbf{r})} \right| = \left| \frac{n}{n+1} \frac{G^s(\mathbf{r})}{G_0(\mathbf{r})} \right|. \tag{3.33}$$

The above equation shows that as the scattering becomes stronger, the convergence speed of the inverse scattering series becomes slower.

3.4 Model tests of scattering series

As noted in the previous section, a comparison of the convergence rates between wave propagation and diffusion depends on the specific parameters that we incorporate. We therefore choose parameters that are widely applied for exploring hydrocarbon reservoirs (Palacky, 1987; Mavko *et al.*, 1998). For the application of the scattering series expressions in equations (3.19) and (3.30) to the acoustic wave and electromagnetic diffusion problems, we adopt the parameters summarized in Table 3.1. Note we assume a velocity perturbation of 10% for the acoustic wave problem

and a perturbation with a factor 10 ($\sigma_0/\sigma = 10$) for the electromagnetic diffusion problem. We also assume that magnetic permeability of the medium is the same as that of free space ($\mu = 4\pi \times 10^{-7}$ N/A^2).

3.4.1 Forward scattering series

Figures 3.3 and 3.4 show the spatial variation of the forward scattering series for the acoustic wave and electromagnetic diffusion equations, respectively. The solutions derived from the forward series (solid curve) are compared with the analytic solution of the scattered field (dotted curve), which is expressed as

$$G^s(\mathbf{r}) = \frac{e^{ikr} - e^{ik_0 r}}{4\pi r}. \tag{3.34}$$

The scattered field of the acoustic wave equation (dotted curve in Figure 3.3) exhibits spatial oscillations, amplitude modulation, and geometric spreading. The scattered field of the electromagnetic diffusion equation (dotted curve in Figure 3.4) shows exponential amplitude decay and monotonous phase change. From equation (3.19), the first order term in the forward series is

$$G_1^s(\mathbf{r}) = \frac{iP}{8\pi k_0} e^{ik_0 r} \tag{3.35}$$

and near the source, exhibits better agreement with the analytic solution than at far receiver locations. As we include higher order terms, the partial sum of the forward series approaches the analytical solution of the scattered field. Note that except for short source-receiver offset, the forward scattering series for the electromagnetic diffusion equation ($N = 5$ in the middle panel of Figure 3.4) requires fewer terms to achieve good agreement with the analytic solution than the series for the acoustic

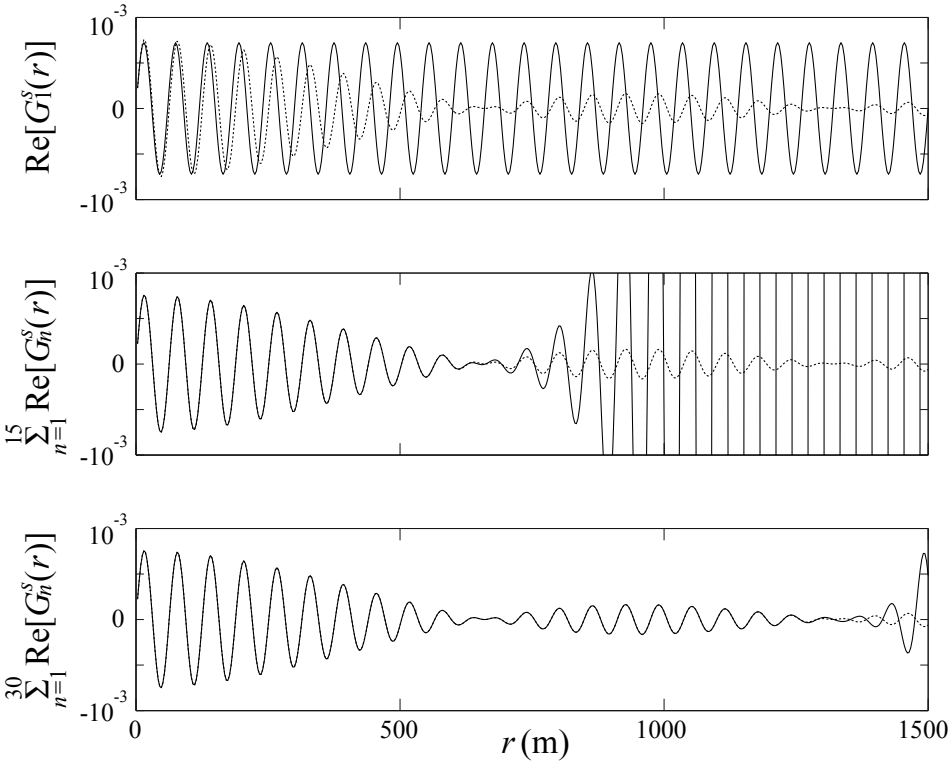

Figure 3.3. Spatial variation of forward scattering series for the acoustic wave equation (real part only). The employed parameters are summarized in Table 3.1. The solutions derived from the forward series (solid curves) are compared with the analytic solution of the scattered field (dotted curves). The top, middle, and bottom panels show the partial sum $\sum_{n=1}^{N} G_n^s(\mathbf{r})$ for $N = 1$, $N = 15$, and $N = 30$, respectively. As we include higher order terms in the forward series, the partial sum of the forward series approaches the analytic solution of the scattered field at an increasing range of r.

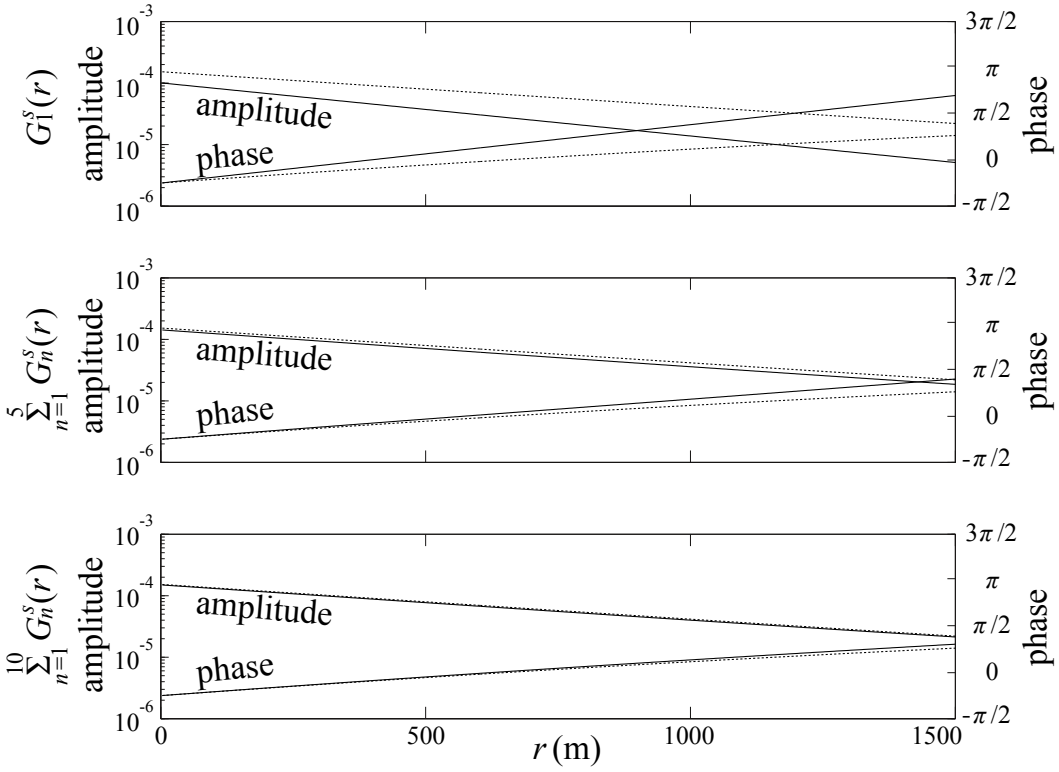

Figure 3.4. Spatial variation of the forward scattering series for the electromagnetic diffusion equation. The employed parameters are summarized in Table 3.1. The solutions derived from the forward series (solid curves) are compared with the analytic solution of the scattered field (dotted curves). The top, middle, and bottom panels show the partial sum $\sum_{n=1}^{N} G_n^s(\mathbf{r})$ for $N = 1$, $N = 5$, and $N = 10$, respectively. As we include higher order terms in the forward series, the partial sum of the forward series approaches the analytic solution of the scattered field at an increasing range of r.

wave equation ($N = 15$ in the middle panel of Figure 3.3). We therefore conclude that for the employed parameters (Table 3.1), which are representative of hydrocarbon exploration, the forward scattering series for the electromagnetic diffusion equation converges faster and requires fewer series terms than does the series for the acoustic wave equation.

3.4.2 Inverse scattering series

Figures 3.5 and 3.6 show the spatial variation of the inverse scattering series for the acoustic wave and electromagnetic diffusion equations, respectively. The solutions derived from the inverse series (solid curve) are compared with the exact value of the perturbation (dotted line), which is real for the wave equation and imaginary for the diffusion equation. Since the true and reference models are assumed to be homogeneous, the model perturbation is constant as well. In these figures, r_c describes the maximum distance for which the inverse scattering series converge to exact values as described below. Considering the convergence criterion given in equation (3.23), we also compare the variation of $|G^s/G_0|$ (solid curve in bottom panels) with the threshold value for convergence (dotted line). The first order terms in the inverse series exhibit significant deviations from the exact values (the first and second panels), and the partial sums of the inverse series up to the 20th order diverge in the ranges where the convergence criterion is violated (the third and fourth panels). For the electromagnetic diffusion equation (Figure 3.6), the ratio $|G^s/G_0|$ increases exponentially with the source-receiver offset r, and the inverse series converges to the exact value of the perturbation within the range that extends from $r = 0$ to the location where the convergence criterion is satisfied ($r < r_c$). On the other hand, the ratio $|G^s/G_0|$ varies periodically for the acoustic wave equation (Figure 3.5), and there thus is in-

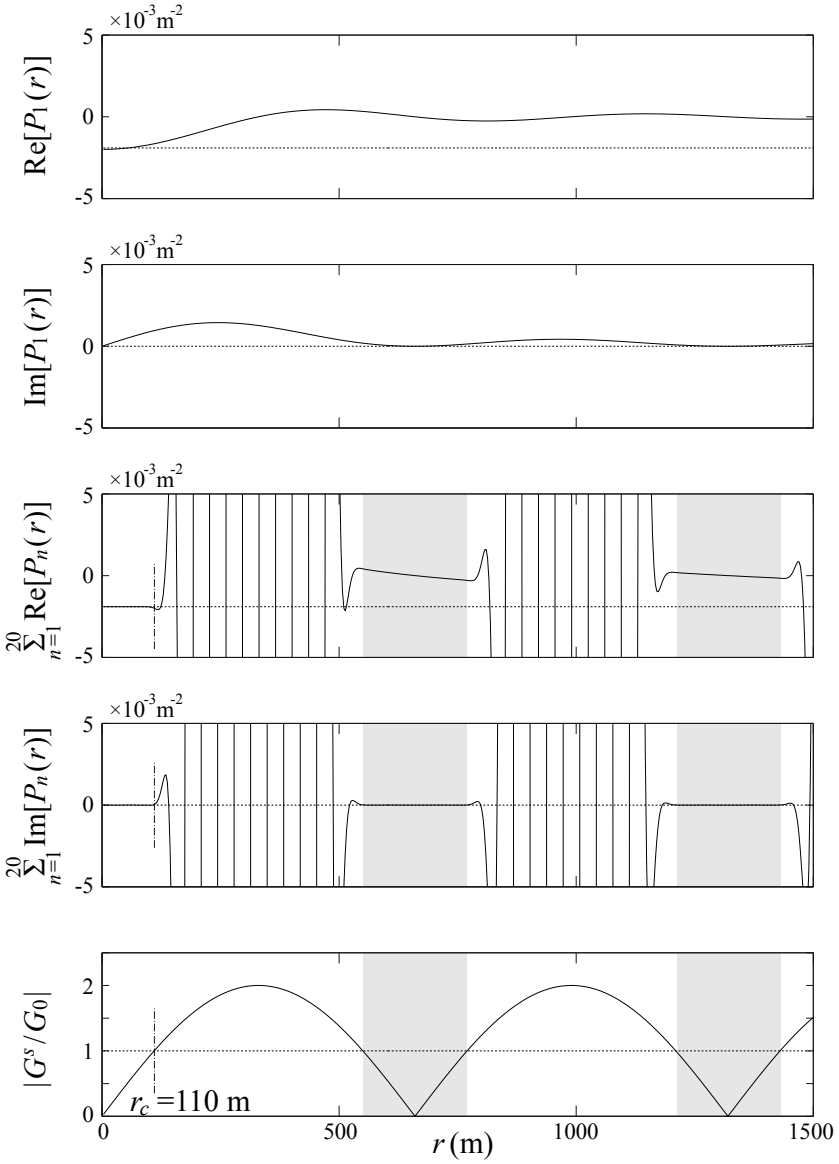

Figure 3.5. Spatial variation of the inverse scattering series for the acoustic wave equation. The employed parameters are summarized in Table 3.1. In the upper four panels, the solutions derived from the inverse series (solid curves) are compared with the exact value of the perturbation $\omega^2(1/c^2 - 1/c_0^2)$ (dotted lines), which is real. The first and third panels compare the real part, and the second and fourth panels show the imaginary part. The first term in the inverse series (the first and second panels) differs significantly from the exact value. The partial sum up to the 20th order term in the inverse series (the third and fourth panels) converges to the exact value within a limited range where $r < r_c$. Outside the range, the inverse series diverges (white regions) or converges to a value different from the exact value of the perturbation (shaded regions). The bottom panel shows the spatial variation of $|G^s(\mathbf{r})/G_0(\mathbf{r})|$.

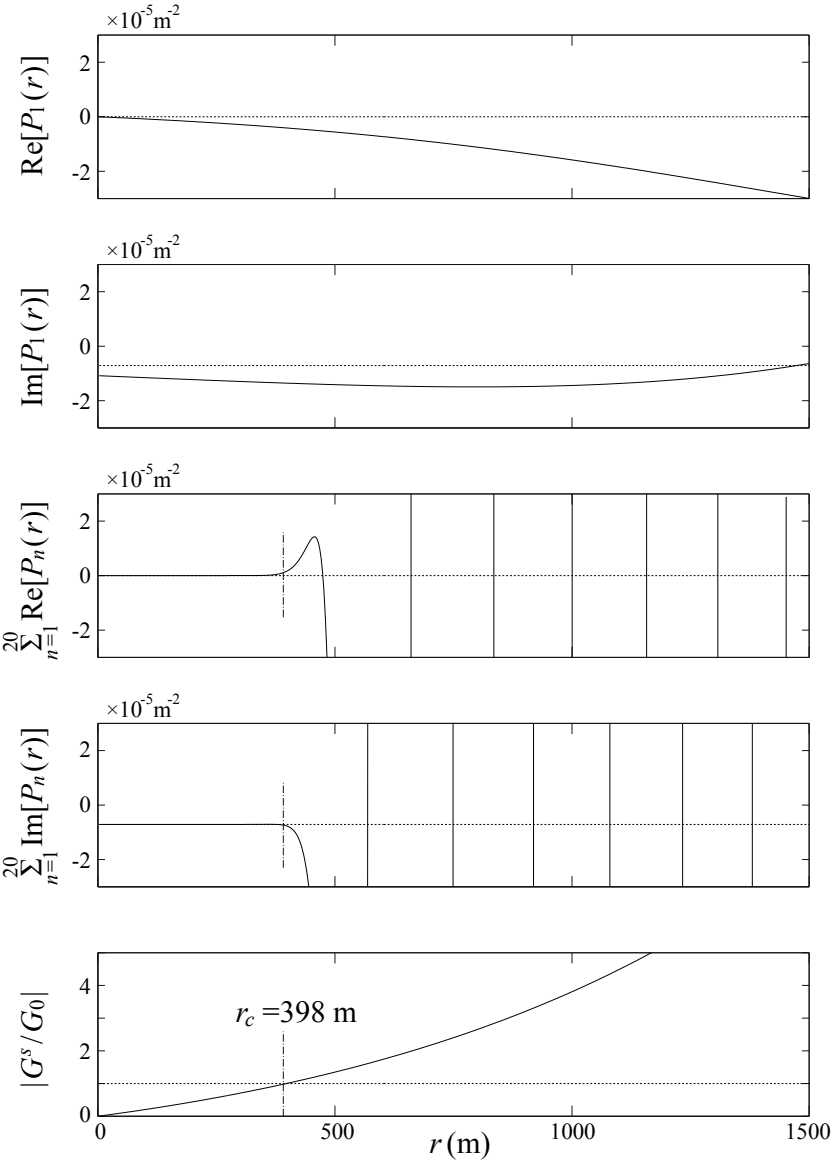

Figure 3.6. Spatial variation of the inverse scattering series for the electromagnetic diffusion equation. The employed parameters are summarized in Table 3.1. In the upper four panels, the solutions derived from the inverse series (solid curves) are compared with the exact value of the perturbation $i\omega\mu(\sigma - \sigma_0)$ (dotted lines), which is imaginary. The first and third panels compare the real part, and the second and fourth panels show the imaginary part. The first term in the inverse series (the first and second panels) differs significantly from the exact value. The partial sum up to the 20th order term in the inverse series (the third and fourth panels) converges to the exact value within a limited range where $r < r_c$ and diverges elsewhere. The bottom panel shows the spatial variation of $|G^s(\mathbf{r})/G_0(\mathbf{r})|$.

finite number of intervals where the convergence criterion is satisfied. This periodic variation arises from the amplitude modulation of the scattered field G^s (equation (3.34) and the dotted curves in Figure 3.3) and illustrates a phenomenon known as the cycle skipping in seismic exploration (Pratt, 1999; Virieux & Operto, 2009). The third and fourth panels in Figure 3.5 show that the inverse series for the acoustic wave equation converges to the exact value only for the first interval ($r < r_c$). Those panels also show that for the remaining intervals (shaded regions), the partial sum of the inverse series remains close to the first order term and does not converge to the exact value.

Compared to the inverse series for the acoustic wave equation (Figure 3.5), the series for the electromagnetic diffusion equation (Figure 3.6) converges to the exact value of the perturbation in a wider spatial range. This convergence pattern suggests that for the employed parameters, the inverse scattering series for the electromagnetic diffusion equation converges faster than does the series for the acoustic wave equation. The above observations also reveal that the convergence criterion given in equation (3.23) plays a crucial role in the reconstruction of the perturbation. We therefore perform a more detailed analysis on the convergence criterion. As noted before, wavenumber k is real for the acoustic wave equation. Denoting the spatial radius of convergence for the inverse series of the wave equation as r_c, we derive the following relation from equation (3.23):

$$\left|e^{i(k-k_0)r_c} - 1\right| = 1. \tag{3.36}$$

The spatial radius of convergence is, therefore, given as

$$r_c = \frac{\pi}{3\left|k - k_0\right|}. \tag{3.37}$$

In case of the electromagnetic diffusion problem, the wavenumber is derived from $k^2 = i\omega\mu\sigma$, and we denote the wavenumber as

$$k = \frac{1+i}{\sqrt{2}}|k|. \tag{3.38}$$

The convergence criterion given in equation (3.23) is rewritten as follows:

$$\left|\frac{G^s(\mathbf{r})}{G_0(\mathbf{r})}\right| = \left|e^{-\frac{|k|-|k_0|}{\sqrt{2}}r} e^{i\frac{|k|-|k_0|}{\sqrt{2}}r} - 1\right| < 1. \tag{3.39}$$

Denoting $\xi = (|k| - |k_0|)/\sqrt{2}$, we establish the following relation at $r = r_c$ (the spatial radius of convergence for the inverse series of the diffusion equation):

$$\left|e^{-\xi r} e^{i\xi r} - 1\right| = 1, \tag{3.40}$$

which can be simplified as

$$e^{-\xi r} = 2\cos\xi r. \tag{3.41}$$

Equation (3.41) is a transcendental equation for the spatial radius of convergence r_c that is analyzed graphically in Figure 3.7. The dotted curve shows the right-hand side of equation (3.41) while the dashed and solid curves show the left-hand side for $\xi < 0$ and $\xi > 0$, respectively. The distance r_c for which the inverse scattering series converges is larger for positive value of ξ ($\sigma > \sigma_0$) than for negative value of ξ ($\sigma < \sigma_0$). In other words, the spatial radius of convergence is larger when choosing a reference model with a small electric conductivity.

Equation (3.39) shows that as r increases, the ratio $|G^s/G_0|$ varies exponentially with distance: there is exponential decrease when $|k| > |k_0|$ ($\sigma > \sigma_0$) and exponential

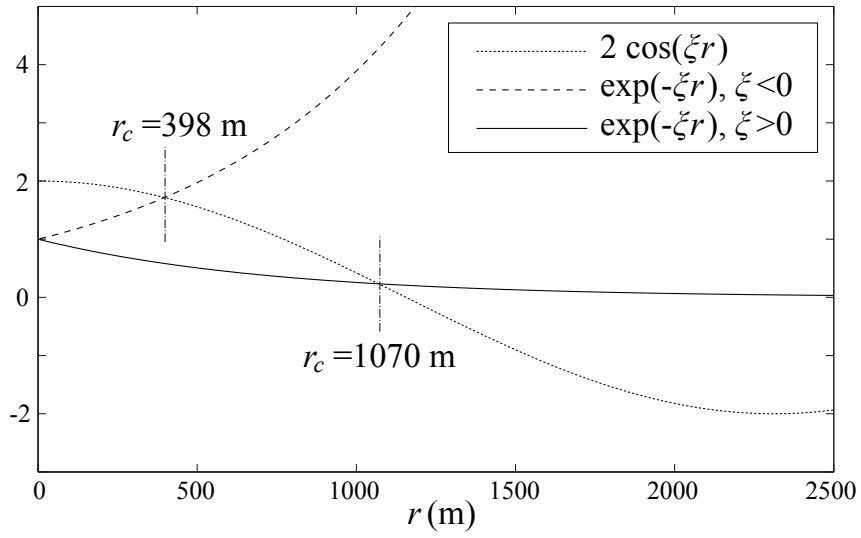

Figure 3.7. Derivation of the spatial radius of convergence r_c for the electromagnetic diffusion problem. The dashed and solid curves show the left-hand side of equation (3.41) for $\xi < 0$ and $\xi > 0$, respectively, while the dotted curve shows the right-hand side of equation (3.41). Applying the parameters summarized in Table 3.1, we derive r_c as 398 m. On the other hand, by switching the two conductivity values in Table 3.1 ($\sigma \leftrightarrow \sigma_0$), r_c is derived as 1070 m.

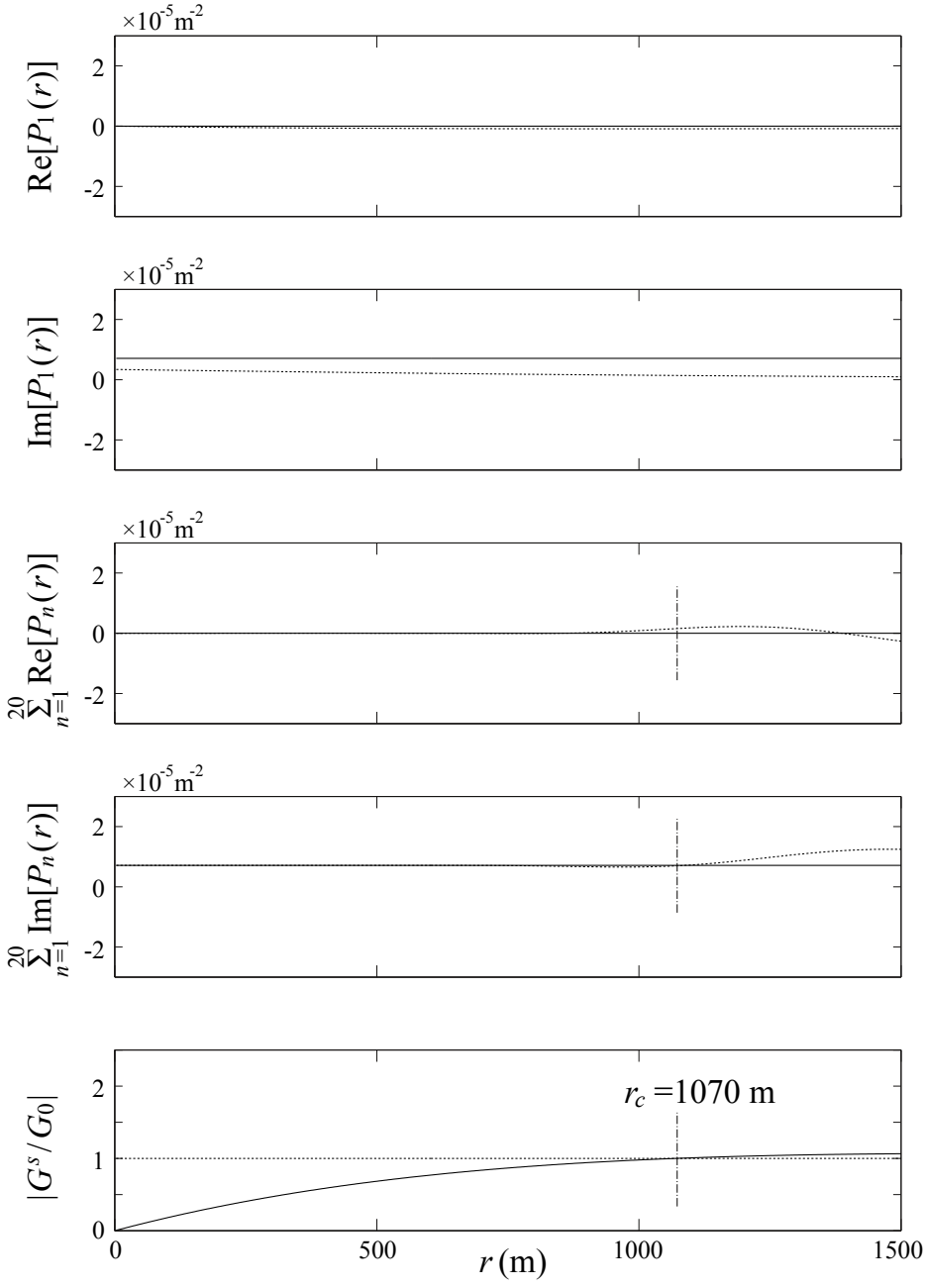

Figure 3.8. Spatial variation of the inverse scattering series for the electromagnetic diffusion equation. The medium properties of the true and reference media are switched from the previous case shown in Figure 3.6 and Table 3.1. Note that the spatial range where $|G^s(\mathbf{r})/G_0(\mathbf{r})| < 1$ is wider than the case shown in Figure 3.6.

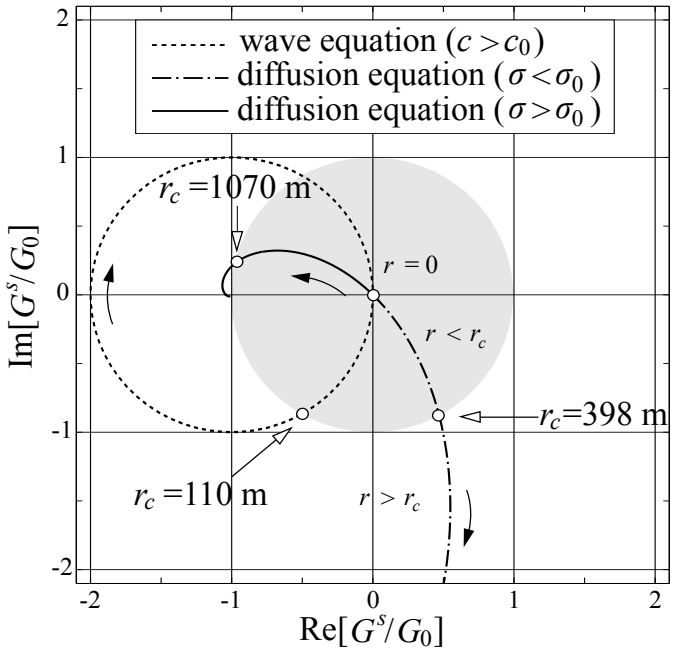

Figure 3.9. The variation of G^s/G_0 in the complex plane for different values of r. The origin of the complex plane indicate $r = 0$, and the arrows denote the directions of increasing r. Three different cases shown in Figures 3.5, 3.6, and 3.8 are compared. The shaded region denotes the area where the inverse series converges.

growth when $|k| < |k_0|$ ($\sigma < \sigma_0$). The inverse scattering problem aims to recover the unknown perturbation from the measured field and a reference model, and we have freedom in choosing a reference model. Therefore, the exponential variation of the ratio $|G^s/G_0|$ in equation (3.39) illustrates that given the true medium, we can accelerate the convergence of the inverse series for the electromagnetic diffusion equation by choosing a reference medium that is less conductive (smaller wavenumber) than the true medium. On the other hand, the acoustic wave equation has a real wavenumber, and the sign of $k-k_0$ is irrelevant to the convergence criterion (equation (3.37)). Figure 3.8 shows the spatial variation of the inverse scattering series for the electromagnetic diffusion equation when the true and reference media switch roles ($\sigma \leftrightarrow \sigma_0$) from the previous case shown in Figure 3.6. Compared to the case when the reference medium is more conductive than the true medium (Figure 3.6), the spatial range of the convergence shown in Figure 3.8 is wider.

Figure 3.9 shows the path of G^s/G_0 in the complex plane as the source-receiver offset r increases for three different cases: the inverse scattering series for the acoustic wave equation (dotted curve), the series for the electromagnetic diffusion equation that corresponds to Figure 3.6 (dashed curve), and the series for the electromagnetic diffusion equation with the reversed medium properties (solid curve). As the source-receiver distance increases, the value of G^s/G_0 moves away from the origin. In the case of acoustic wave propagation, the path forms a closed circle, and the sign of $c - c_0$ determines the direction of the movement as r increases (clockwise direction when $c > c_0$ and counterclockwise direction when $c < c_0$). On the other hand, the path of G^s/G_0 does not form a closed circle for the electromagnetic diffusion problem. Depending on the sign of $\sigma - \sigma_0$, the ratio G^s/G_0 moves out of the convergence area ($\sigma < \sigma_0$) and approaches the point where $G^s/G_0 = -1$ ($\sigma > \sigma_0$). The convergence of

the inverse series for the electromagnetic diffusion equation can thus be accelerated by choosing a reference medium that is less conductive than the true medium. The different paths represented by the dashed curve ($\sigma < \sigma_0$) and solid curve ($\sigma > \sigma_0$) demonstrate the significance of the choice of the reference medium for the convergence of the inverse scattering series for the electromagnetic diffusion problem.

3.5 Conclusions

We studied the feasibility of applying the inverse scattering series to electromagnetic exploration by identifying the difference between the convergence patterns of the scattering series for acoustic wave and electromagnetic diffusion problems. We considered two different states of infinite homogeneous media, related the scattered field G^s and perturbation P via the 3D Green functions of the homogeneous media, and formulated the forward and inverse scattering series. Analysis of the formal expressions of the scattering series solutions shows that for electromagnetic diffusion, the reference medium should be sufficiently conductive to allow convergence of the forward series. The analysis also shows that there is no fundamental difference between the convergence pattern of the scattering series for the acoustic wave and electromagnetic diffusion equations. In other words, the rapid spatial decay of a diffusive field does not necessarily mean fast convergence of the scattering series for the diffusion equation. Model tests with parameters representing geophysical exploration of hydrocarbon reservoirs suggest, however, that the scattering series for the electromagnetic diffusion equation converge faster than that for the acoustic wave equation. The model tests also show that for the electromagnetic diffusion equation, we can facilitate the convergence of the inverse scattering series by choosing a reference medium that is less conductive than the true medium. This study thus provides insights

into the convergence requirements of the scattering series and guidelines for further application of the inverse scattering series to the interpretation of electromagnetic data.

In this study, we considered mathematical prototypes of the wave and diffusion equations and did not associate our study with specific physical fields such as electric or magnetic fields. We formulated the scattering series via the Taylor series instead of the integral equation approach, which is necessary for studies regarding an inhomogeneous model (Prosser, 1969; Weglein *et al.*, 2003). The convergence condition of the forward scattering series deduced in this study is however equivalent to that from the integral equation approach (Prosser, 1976). Moreover, this study describes the convergence condition of the inverse scattering series in a more quantitative way than the integral equation approach. In fact, the convergence criterion of the inverse scattering series identified in this work is a necessary condition when we apply the inverse series to an inhomogeneous model. Note that in the integral equation approach, the evaluation of the nth order term (P_n) in the inverse scattering series involves a series that consists of all of the lower order terms ($P_1, P_2, \cdots, P_{n-1}$) in the inverse series (Prosser, 1969; Weglein *et al.*, 2003). This series is analogous with the forward scattering series, and the convergence condition of the forward series indirectly affects the convergence of the inverse series. Our next research will substantiate the convergence conditions identified in this work with a specific physical field, the electric field, within an inhomogeneous medium and examine how the convergence condition of the forward series affects the convergence of the inverse series.

While comparing the scattering series for acoustic wave propagation and electromagnetic diffusion, it is necessary to consider the noise stability of the forward and inverse scattering series as well as the convergence. The study of the noise stability

involves the nonlinear error propagation (**?**Dorren & Snieder, 1997) and necessitates elaborated modeling of the acoustic wave and electromagnetic data noise. We aim to extend our research to comparing between the noise stability for acoustic wave propagation and electromagnetic diffusion.

3.6 Acknowledgements

This work was supported by the Consortium Project on Seismic Inverse Methods for Complex Structures at Center for Wave Phenomena (CWP). We acknowledge Arthur Weglein (University of Houston) and Evert Slob (Delft University of Technology) for helpful information, discussions, and suggestions. We are also grateful to colleagues of CWP for valuable discussions and technical help.

Chapter 4

CONVERGENCE ANALYSIS OF SCATTERING SERIES INVERSE SCATTERING SERIES VS. MODIFIED INVERSE SCATTERING SERIES

4.1 Summary

The inverse scattering series (ISS) is a tool that enables rapid interpretation of electromagnetic data using fewer computational resources and less *a priori* information than conventional approaches. However, the ISS converges only when the contrast between true and reference models is sufficiently small. We discuss the origin of the narrow range of convergence and qualitatively describe that there are two contradictory conditions that determine the convergence of the ISS. To mitigate the convergence conditions, we propose an alternative approach to electromagnetic data inversion: the modified inverse scattering series (MISS). The MISS is based on the iterative dissipative method (IDM), which provides an absolutely converging forward series. We consider several 1D models and study the applicability of the MISS to inverse problems of electromagnetic data in geophysics. The model tests reveal that compared to the ISS, the MISS converges for a wider contrast of the electric conductivity between true and reference models. The 1D tests also demonstrate that models reconstructed by the MISS are closer to true models than models generated via the ISS. This study shows that the MISS enables fast reconstruction of an electromagnetic model, which can be a good starting model for large-scale geophysical data

processing, such as marine controlled-source electromagnetic (CSEM) data inversion.

4.2 Introduction

Marine electromagnetic surveys are efficient complementary tools to seismic surveys in searching for a hydrocarbon reservoir (Hoversten *et al.*, 2006; Hu *et al.*, 2009; Kwon & Snieder, 2011b). The advantage of electromagnetic exploration over seismic methods originates from its capability to discern the reservoir composition: hydrocarbon is a poor electric conductor while water within a reservoir increases the electric conductivity. The most well-known marine electromagnetic technique for hydrocarbon exploration is the controlled-source electromagnetic (CSEM) method (Chave & Cox, 1982; Cox *et al.*, 1986; Srnka *et al.*, 2006). The typical frequency range and depth of investigation of the method are 0.1 - 10 Hz and several kilometers, respectively. To ensure greater depth penetration, CSEM data can be combined with magnetotelluric (MT) data, which are generated by natural low-frequency sources (Abubakar *et al.*, 2009; Commer & Newman, 2009).

There is a wide spectrum of approaches to the modeling of CSEM and MT data: the finite-difference (Yee, 1966; Alumbaugh *et al.*, 1996), finite-element (Pridmore *et al.*, 1981; Um *et al.*, 2010), and integral equation methods (Hohmann, 1975; Zhdanov *et al.*, 2006). Several approximate methods that require various prerequisites such as a low-contrast assumption (Habashy *et al.*, 1993; Torres-Verdin & Habashy, 2001) are also available. Among them, the finite-difference method is the most prevalent approach for large-scale geophysical problems because of its apparent simplicity of numerical implementation and adaptability to model complexity. The finite-difference method, on the other hand, necessitates more computational resources and processing time. Furthermore, a reasonable interpretation of marine electromagnetic surveys

generally involves 3D inversion, which still remains a difficult and computationally intense task (Newman & Alumbaugh, 1997; Commer & Newman, 2008). Only recently, the first successful examples of 3D electromagnetic inversion have been reported, and the inverse problem is currently an area of intense research (Avdeev, 2005).

The difficulty of 3D electromagnetic inversion arises from the fact that the inverse problem is large-scale, strongly nonlinear, and severely ill-posed (Jackson, 1972; Parker, 1977). The inversion process aims to retrieve a model that has infinitely many degrees of freedom from a finite amount of data (Snieder, 1998). There are many factors that help constrain the output from the process that include the use of *a priori* information, using different starting models of the inversion, and the design of the data misfit function or model regularization (Tikhonov & Arsenin, 1977). In this study, we implement a scheme for electromagnetic data processing that enables rapid interpretation of data and provides a good starting model for more rigorous large-scale inversion. The inverse scattering series (ISS) is adequate for this goal because it can effectively resolve the nonlinearity of an inverse problem and reconstruct an electromagnetic model using fewer computational resources and less *a priori* information than the conventional approaches addressed above.

The inverse scattering theory quantitatively retrieves the scatterers from knowledge of the scattering data. The theory originates from inverse problems in quantum scattering theory and formal solutions of inverse scattering problems (Gel'fand & Levitan, 1951; Jost & Kohn, 1952; Moses, 1956; Prosser, 1969). The ISS expresses the retrieved model perturbation as a series in order of the scattered field. The geophysical application of the ISS has focused on seismic exploration, in particular on multiple suppressions (Weglein *et al.*, 1997) and seismic imaging (Weglein *et al.*, 2010). However the ISS has not been widely applied to the interpretation of electro-

magnetic surveys. Kwon & Snieder (2010) have recently investigated the feasibility of this application and clarified the difference between scattering series for acoustic wave propagation and electromagnetic diffusion. Their analytic study also identifies convergence conditions of the forward and inverse series for homogeneous models.

In the following, we formulate the ISS for 1D electromagnetic model reconstruction and exemplify that the ISS converges only when the contrast between the true and reference models is sufficiently small. We also show that in addition to the convergence condition of the inverse series, there is another condition that determines the convergence/divergence of the ISS, and we illustrate that this condition is closely related to the convergence condition of the forward series. We thereafter propose an alternative approach, the modified inverse scattering series (MISS). The MISS is based on the iterative dissipative method (IDM), which guarantees an absolutely converging forward series (Singer, 1995; Singer & Fainberg, 1995; Pankratov *et al.*, 1995), and the convergence of the MISS is thus free from the newly identified condition. Finally, we show that the MISS more robustly converges than the ISS and discuss the advantage of the MISS over the original by comparing the inversion results from the two methods.

4.3 1D formulation of inverse scattering series

The fundamental equations for electromagnetism, the Maxwell's equations (Jackson, 1999), in an isotropic medium are

$$\nabla \times \mathbf{E} - i\omega\mu\mathbf{H} = 0, \tag{4.1}$$

$$\nabla \times \mathbf{H} - (\sigma - i\omega\epsilon)\,\mathbf{E} = \mathbf{J}_s, \tag{4.2}$$

where $\mathbf{E}$ is the electric field (V/m), $\mathbf{H}$ the magnetic field (A/m), $\mathbf{J}_s$ the electric current source (A/m^2), μ the magnetic permeability (N/A^2), σ the electric conductivity (S/m), and ϵ the dielectric permittivity (C^2/Nm^2), respectively. We consider a single Fourier component corresponding to a time variation $e^{-i\omega t}$. Outside of certain types of ore bodies, magnetizable materials are rare in the subsurface (Chave & Cox, 1982), and we take the magnetic permeability μ to be the free space value. For frequencies of electromagnetic methods used in hydrocarbon exploration, the displacement current ($\omega\epsilon\mathbf{E}$) is much smaller than the induction current ($\sigma\mathbf{E}$) in the subsurface (Hohmann, 1975). We therefore ignore the variation of the dielectric permittivity ϵ and approximate it to the value of water. The 1D electromagnetic model of this study is illustrated in Figure 4.1: the electric conductivity varies in the z-axis direction, and a harmonic plane wave propagates in the same direction. Applying the 1D assumption to the Maxwell's equations, we derive the following scalar Helmholtz equation:

$$L(z;\omega)\, G(z, z_s;\omega) = -\delta(z - z_s), \tag{4.3}$$

where G is the Green function of the electric field (the component of $\mathbf{E}$ parallel to the electric current source), z_s represents the location of the unit current source, and the differential operator L is

$$L(z;\omega) = \frac{1}{i\omega\mu}\frac{d^2}{dz^2} + \sigma(z) - i\omega\epsilon. \tag{4.4}$$

Note that as shown in Figure 4.1, the electric field direction is opposite to the electric current source, and the unit of the Green function is Ω (electric field / (unit current source $\times$ unit length)).

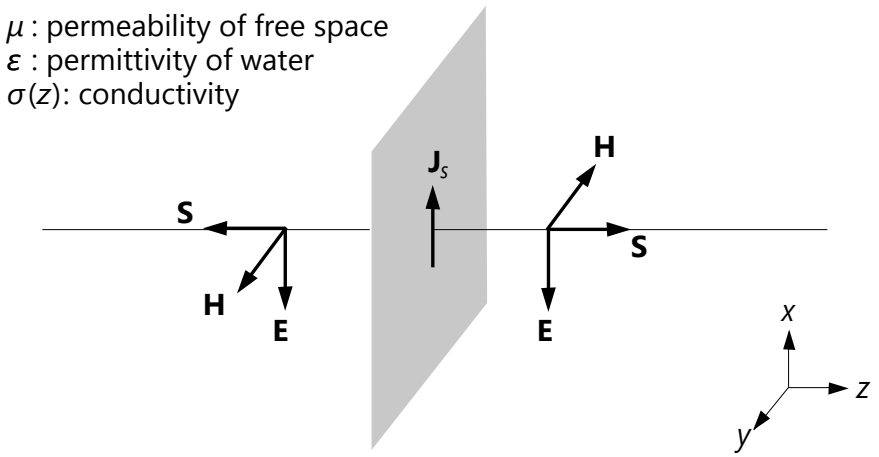

Figure 4.1. 1D electromagnetic radiation geometry for this study. The Poynting vector **S** indicates the direction of energy flux. The electric field **E** is divergenceless, and the direction of the electric field is opposite to that of the infinitely planar current source $\mathbf{J}_s$ on the (x, y) plane. The electric conductivity σ varies in the direction normal to the current source.

We consider two types of 1D electromagnetic media: the true (perturbed) and reference (unperturbed) media. The governing equations for the two media are represented by two differential operators: L and L_0, respectively. We denote the Green functions for the two media as G and G_0, respectively. The Lippmann-Schwinger equation (Lippmann & Schwinger, 1950; Colton & Kress, 1998) relates the Green functions for the true and reference models as

$$\begin{aligned} G(z, z_s; \omega) &= G_0(z, z_s; \omega) \\ &\quad + \int G_0(z, z'; \omega)\, P(z')\, G(z', z_s; \omega)\, dz', \end{aligned} \tag{4.5}$$

where the perturbation P is defined as the difference between the two differential

operators:

$$P(z) = L(z;\omega) - L_0(z;\omega) = \sigma(z) - \sigma_0(z). \tag{4.6}$$

The scattered field G^s is the difference between the two Green functions ($G - G_0$) that can, in operator form, be expanded as an infinite series in order of the perturbation P:

$$G^s = G_0 P G_0 + G_0 P G_0 P G_0 + \cdots . \tag{4.7}$$

The above equation is known as the Born, Neumann, or forward scattering series (Weglein *et al.*, 1997). It is known that for homogeneous models, the forward scattering series of electromagnetic diffusion problems converges only when the reference medium is sufficiently conductive (Kwon & Snieder, 2010) such that

$$\sigma < 2\,\sigma_0. \tag{4.8}$$

The divergence of the forward series implies that strong scattering occurs, and the term $G_0 P$ in equation (4.5) is no longer a contracting kernel (Pankratov *et al.*, 1995).

While the forward series describes the scattered field G^s as a series in order of the perturbation P, the inverse scattering series (ISS) addresses the perturbation as a series expansion in order of the scattered field:

$$P = P_1 + P_2 + P_3 + \cdots , \tag{4.9}$$

where P_n is the portion of P that is of the nth order of the scattered field. Substituting expression (4.9) into the forward series (equation (4.7)) and equating terms that are

of the same order of the scattered field G^s (Prosser, 1969; Weglein *et al.*, 2003) yield the following set of integral equations represented in operator form:

$$\begin{aligned} G^s &= G_0 P_1 G_0, && (4.10)\\ 0 &= G_0 P_2 G_0 + G_0 P_1 G_0 P_1 G_0, && (4.11)\\ 0 &= G_0 P_3 G_0 + G_0 P_1 G_0 P_2 G_0 + G_0 P_2 G_0 P_1 G_0 \\ &+ G_0 P_1 G_0 P_1 G_0 P_1 G_0, && (4.12)\\ &\cdots \end{aligned}$$

Equation (4.10) is the linear or Born approximation which allows P_1 to be determined from the scattered field G^s. P_2 is then computed from P_1 with equation (4.11). Equation (4.12) determines P_3 from P_1 and P_2. Starting with the scattered field, one continues the iterative process and constructs the entire series for the perturbation P. The nth order term in the inverse series is derived by solving the following Fredholm integral equation of the first kind (Morse & Feshbach, 1953):

$$\begin{aligned} &D_n(G^s, P_1, P_2, \cdots, P_{n-1}; \omega) \\ &\quad = \int G_0(z, z'; \omega)\, P_n(z')\, G_0(z', z_s; \omega)\, dz', \end{aligned} \tag{4.13}$$

where D_n generally consists of $2^{n-1}-1$ terms. In this study, we assume that the source and receiver are coincident. Applying this assumption and utilizing the reciprocity principle yield the following relation:

$$G_0 P_l G_0 P_m G_0 = G_0 P_m G_0 P_l G_0, \tag{4.14}$$

where l and m are arbitrary. The above relation simplifies D_n to

$$D_n = \begin{cases} G^s & (n=1), \\ -G_0 P_1 G_0 P_1 G_0 & (n=2), \\ -G_0 P_1 D_{n-1} & (n=3,4,\cdots). \end{cases} \tag{4.15}$$

Kwon & Snieder (2010) have shown that for homogeneous models, expression (4.9) converges only for weakly scattered fields that satisfy

$$\left| \frac{G^s}{G_0} \right| < 1. \tag{4.16}$$

This convergence condition suggests that for electromagnetic diffusion, we can improve the convergence of the ISS by choosing a resistive reference medium for which the amplitude of the reference Green function $|G_0|$ is large.

The main advantage of the ISS is that it enables rapid interpretation of electromagnetic data. The merit of the ISS is best taken advantage of by choosing a reference model for which the Green function G_0 is known analytically. Throughout this study, we assume the simplest reference model, a homogeneous medium. In the case of a homogeneous reference medium, the solution of equation (4.3) is (Morse & Feshbach, 1953)

$$G_0(z, z_s; \omega) = -\frac{\omega\mu}{2k_0} e^{ik_0|z-z_s|}, \tag{4.17}$$

where $k_0^2 = \omega^2\mu\epsilon + i\omega\mu\sigma_0$, and equation (4.13) becomes

$$D_n(\omega) = \left(\frac{\omega\mu}{2k_0}\right)^2 \int e^{ik_0(|z-z'|+|z'-z_s|)} P_n(z')\, dz'. \tag{4.18}$$

The above expression can, however, generate a negative conductivity. A conventional approach to avoid this unphysical solution is inverting for the logarithm of the electric conductivity (Newman & Alumbaugh, 1997). Following that convention, we introduce an intermediate parameter M such that $\sigma = \sigma_0\, e^M$, assume that σ is close to the reference conductivity, and approximate the perturbation as

$$P(z) = \sigma(z) - \sigma_0 \simeq \sigma_0\, M(z). \tag{4.19}$$

Expression (4.18) is then rewritten as

$$D_n(\omega) = \left(\frac{\omega\mu}{2k_0}\right)^2 \int \sigma_0 e^{ik_0(|z-z'|+|z'-z_s|)} M_n(z')\, dz'. \tag{4.20}$$

We solve equation (4.20) for M_n through singular value decomposition (Golub & Reinsch, 1970) and reconstruct the electric conductivity as follows:

$$\sigma(z) = \sigma_0 \, \exp\left(\sum M_n(z)\right). \tag{4.21}$$

Note that the approximation in equations (4.19) - (4.21) is a deviation from the rigorous definition of the ISS approach in equations (4.6) - (4.18) because expression (4.19) is a linear approximation, and we discard higher order terms of the Taylor series expansion of $\sigma(M)$. We adopt the approximation to clarify limitations of the ISS and to highlight the advantages of a modified approach that we propose later in this study.

4.4 Model tests of inverse scattering series

To simulate the electric field for true (perturbed) models, we use the finite-difference method with the staggered grid algorithm (Yee, 1966) and suppress artificial reflections from the boundary of the modeling domain via the perfectly match layer method (Berenger, 1994). The spatial range of the modeling domain is $-20 < z < 20$ km, the spatial discretization interval Δz is 20 m, and the unit electric current source is at the origin. We add frequency independent Gaussian random noise with a standard deviation 10^{-9} V/m to the simulated electric field. To solve equation (4.20) for M_n, we discretize the inverse problem: the frequency sampling range is 0.1 - 10 Hz, and 51 frequency samples are evenly distributed on a logarithmic scale.

The inverse problem is ill-posed (Jackson, 1972; Parker, 1977) and nonlinear (Snieder, 1998). It is thus necessary to include a stabilizing functional (Tikhonov & Arsenin, 1977) for the reconstruction of a stable solution. The stabilizing functional Φ_m is part of a penalty functional Φ and trades off between data misfit Φ_d and *a priori* information: $\Phi = \Phi_d + \beta\Phi_m$, where β is a trade-off coefficient or model regularization factor. The choice of stabilizing functional is important for electromagnetic inverse problems. In this study, we regularize the roughness of the model (Constable *et al.*, 1987) as follows:

$$\Phi_m = \int \left(w(z) \frac{d^2 M}{dz^2} \right)^2 dz, \tag{4.22}$$

where a depth weighting factor $w(z)$ is proportional to $e^{|z/1\mathrm{km}|}$. The trade-off coefficient β is model-dependent, and we determine the coefficient from an L-curve analysis (Hansen, 1992) for each model. In this section, we consider resistive and conductive anomaly models.

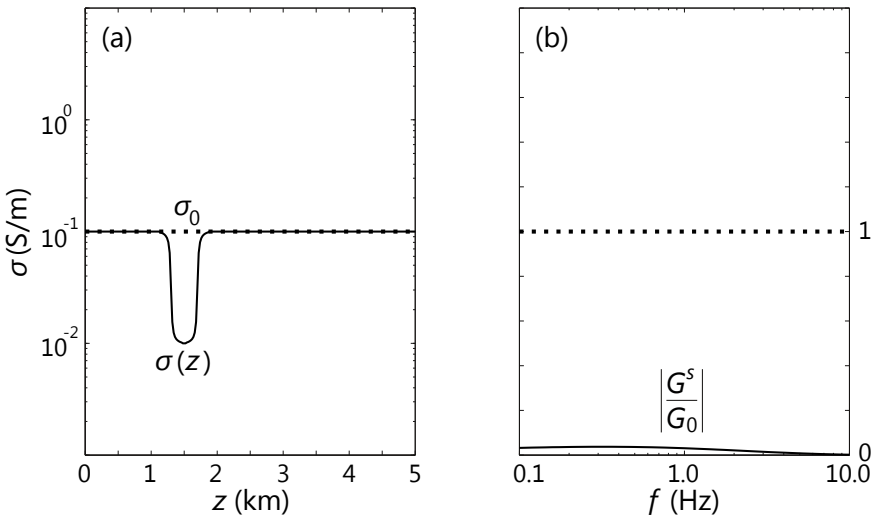

Figure 4.2. Resistive anomaly model. (a) True model (solid curve) versus reference model (dotted line) of the inverse series. The reference conductivity is identical with the background conductivity of the true model. (b) The convergence requirement of the inverse series, expression (4.16), is satisfied in the employed frequency range.

4.4.1 Resistive anomaly model

Figure 4.2(a) presents the true (solid curve) and reference (dotted line) media of the resistive anomaly model. The true medium consists of a resistive structure at $z = 1.5$ km and a conductive background. Note that the resistive layer constitutes a strong perturbation: the ratio of the electric conductivity between the conductive background and resistive target is 10. The conductivity of the background is same as that of the reference medium. Figure 4.2(b) illustrates that within the frequency range used in the experiment, the scattered field has a smaller amplitude than the reference Green function and fulfills the convergence condition of the inverse series in expression (4.16).

Figure 4.3 demonstrates how the ISS evolves as we include higher order pertur-

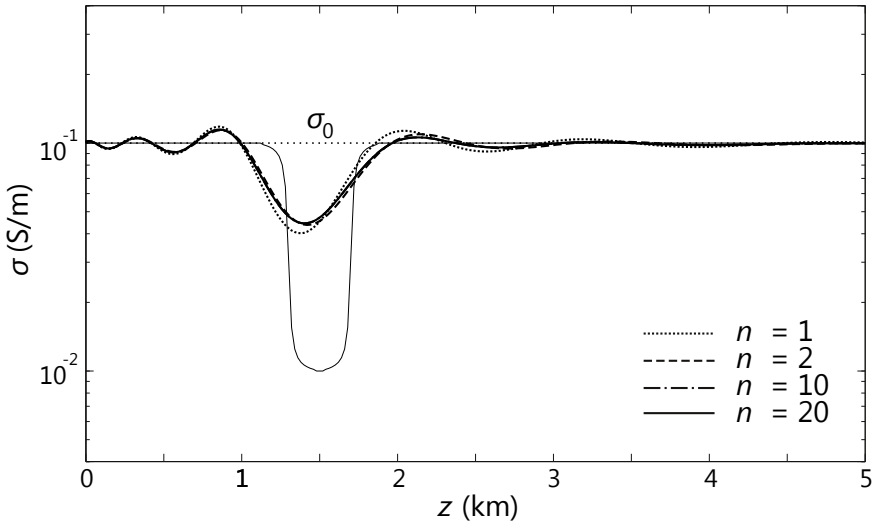

Figure 4.3. ISS solutions for the resistive anomaly model shown in Figure 4.2. The solutions are derived from equation (4.21) and compared for increasing order n of the inverse series. The thin solid curve denotes the true model. The ISS converges.

bation terms. The inverse series converges for the resistive anomaly model: the ISS solution evaluated up to the 10th order ($n = 10$) is practically identical to the solution evaluated up to the 20th order ($n = 20$). This convergence pattern of the ISS is consistent with the value of $|G^s/G_0|$ shown in Figure 4.2(b). The reconstructed model is a linear combination of singular vectors that span the resolvable model space and shows a more significant oscillatory variation near the resistive target. The reconstructed conductivity value of the resistive target is roughly three times that of the true model because the reconstruction of the resistive target is physically limited by the relatively conductive background medium, which shields the resistive structure. The Born approximation ($n = 1$) accounts for most of reconstructing the resistive structure of this model.

4.4.2 Conductive anomaly model

Figure 4.4 depicts a conductive structure at $z = 1.5$ km and a relatively resistive background. The conductivity of the reference model is same as that of the background medium. As in the case of the previous model, the scattered field has a smaller amplitude than the reference Green function within the employed frequency range, which suggests convergence of the inverse series. The inverse series shown in Figure 4.5, however, does not converge for the conductive anomaly model. The model reconstructed by the Born approximation (dotted curve) reveals the conductive structure, but the subsequent higher order solutions diverge. The divergence of the ISS for this model suggests that in addition to the amplitude of the scattered field G^s (expression (4.16)), there is another factor that affects the convergence/divergence of the ISS. Recall that during the ISS procedure, we iteratively solve equation (4.20) for the increasing order n of the inverse series, and its solution M_n depends on the left hand side of equation (4.20), D_n. Figure 4.6 shows that contrary to the case of the resistive anomaly model, $|D_n|$ increases exponentially during the iterative process for the conductive anomaly model. This divergence of D_n causes the divergence of the ISS.

To illustrate the convergence condition of D_n, we rewrite D_n from equation (4.15) as

$$D_n = (-1)^{n+1} (G_0 P_1)^n G_0 \tag{4.23}$$

and observe the similarity between D_n and the forward scattering series. Assume that we solve a forward scattering problem for a true model that is identical to the model recovered from the Born approximation ($P = P_1$ and $\sigma = \sigma_1$). The nth order

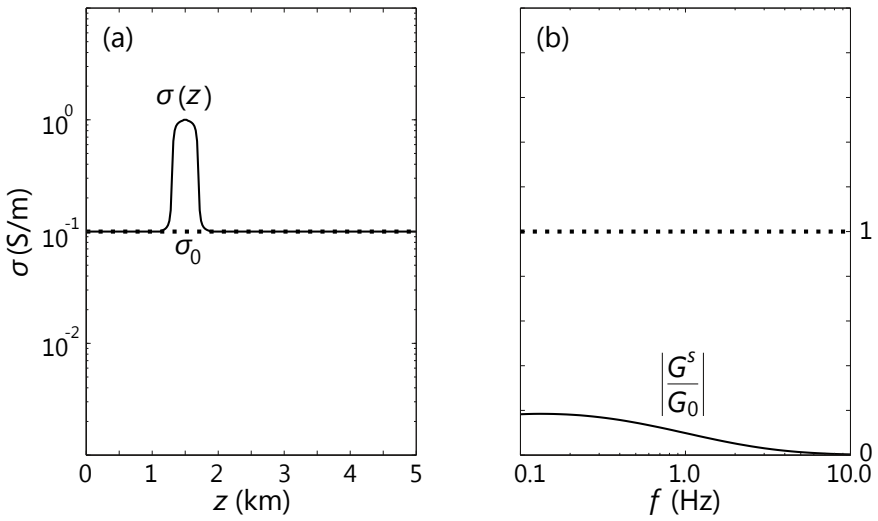

Figure 4.4. Conductive anomaly model. (a) True model (solid curve) versus reference model (dotted line) of the inverse series. The reference conductivity is identical with the background conductivity of the true model. (b) The convergence requirement of the inverse series, expression (4.16), is satisfied in the employed frequency range.

term in this forward series then becomes

$$G_n^s = (G_0 P_1)^n G_0. \tag{4.24}$$

Considering the convergence condition for homogeneous models in equation (4.8), we qualitatively estimate the convergence condition of this forward series as

$$\sigma_1 < 2\,\sigma_0. \tag{4.25}$$

Note that equations (4.23) and (4.24) have an identical kernel $G_0 P_1$, and expression (4.25) therefore also qualitatively describes the convergence condition of D_n: for the convergence of D_n, the reconstructed model from the Born approximation σ_1 needs

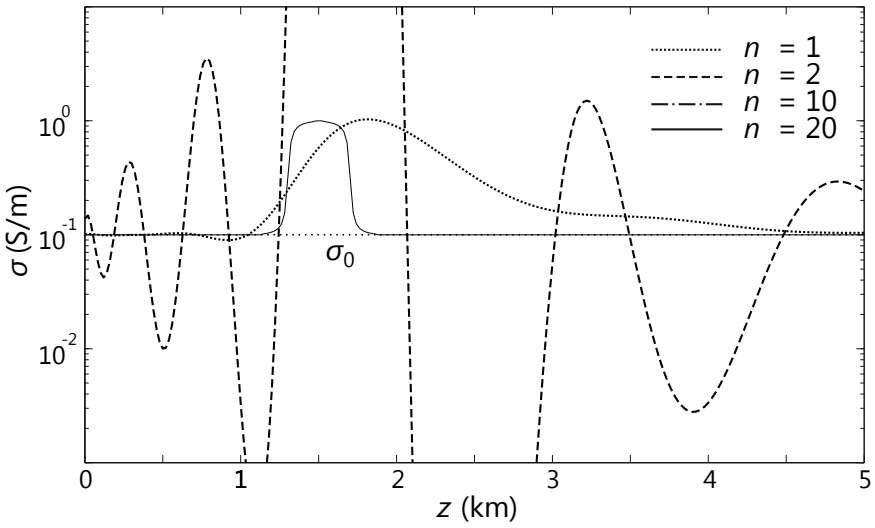

Figure 4.5. ISS solutions for the conductive anomaly model shown in Figure 4.4. The solutions are derived from equation (4.21) and compared for increasing order n of the inverse series. The thin solid curve denotes the true model. The ISS diverges. The ISS solutions evaluated up to the 10th and 20th orders are not displayed because of the rapid divergence.

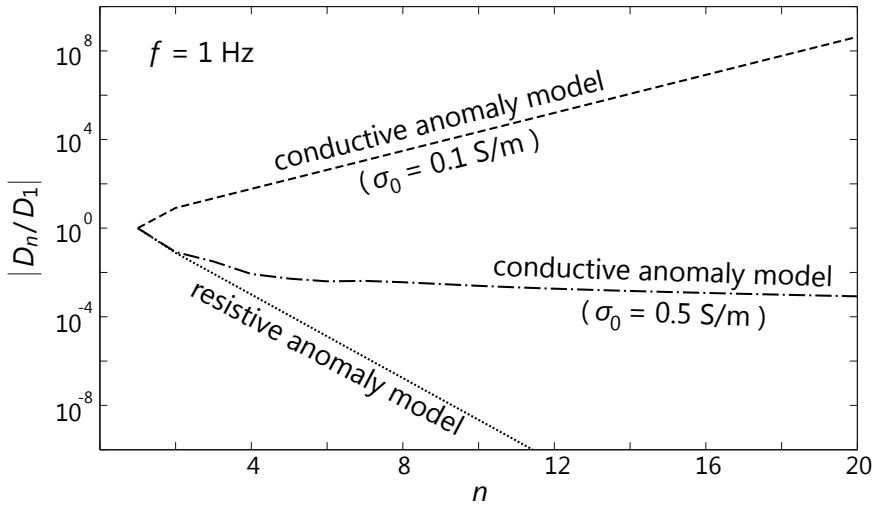

Figure 4.6. The left hand side of equation (4.20), D_n, as a function of the order n of the ISS for $f = 1$ Hz. The dotted and dashed curves represent the ratio $|D_n/D_1|$ for the models shown in Figures 4.2 and 4.4, respectively. Contrary to the resistive anomaly model, the ratio exhibits an exponential increase for the conductive anomaly model with $\sigma_0 = 0.1$ S/m. This exponential increase causes the divergence of the ISS (Figure 4.5). Choosing a more conductive reference model ($\sigma_0 = 0.5$ S/m) decreases the ratio (dot-dashed curve).

to be sufficiently resistive compared to the reference model. In other words, it is necessary to choose a sufficiently conductive reference model that allows σ_1 to satisfy expression (4.25).

Figure 4.5 shows that near $z = 1.7$ km, the maximum conductivity of the solution retrieved from the Born approximation ($n = 1$) is 10 times larger than the reference conductivity (0.1 S/m), and the criterion (4.25) for convergence is not satisfied. The left hand side of equation (4.20) and the inverse series consequently diverge as we incorporate higher order terms. This example demonstrates the challenge of reconstructing a conductive anomaly via the inverse scattering formulation and suggests that for the convergence of the inverse series, the reference model must be sufficiently conductive such that the Born approximation yields a solution that satisfies expression (4.25). One therefore may choose a more conductive reference model that allows D_n to decrease during the ISS procedure as shown in Figure 4.6 (dot-dashed curve). Figure 4.7(a) presents the situation, where the reference conductivity σ_0 is 5 times larger than the background value of the previous example in Figure4.4(a). The more conductive reference model yields, however, a smaller amplitude of the reference Green function and a larger ratio between the scattered field and reference Green function in expression (4.16). Figure 4.7(b) shows that by choosing the more conductive reference model, the convergence condition of the inverse series ($|G^s/G_0| < 1$) is violated. The corresponding divergence of the inverse series is demonstrated in Figure 4.8.

4.4.3 Limitation of inverse scattering series

The convergence conditions of expressions (4.16) and (4.25) are contradictory: expression (4.16) favors more a resistive reference model, and expression (4.25) prefers more a conductive model. The two examples presented in Figures 4.4 - 4.8 pose the

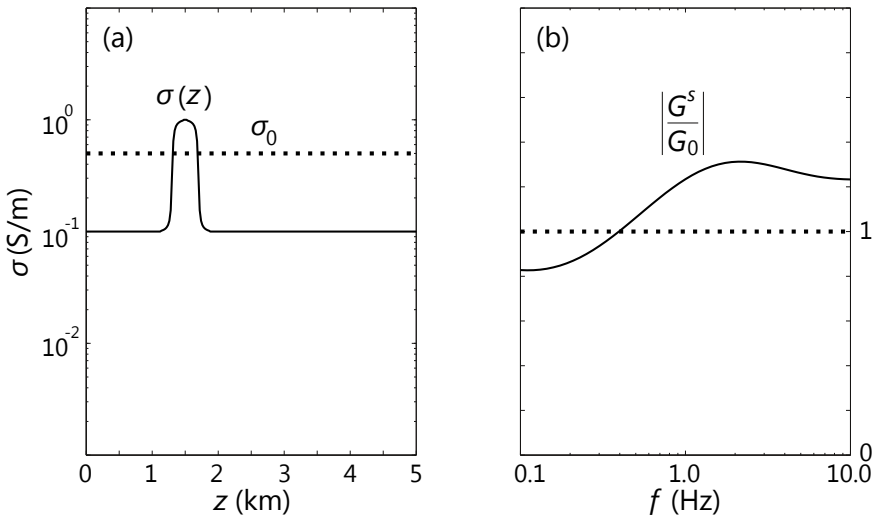

Figure 4.7. Conductive anomaly model with a more conductive reference model than the model shown in Figure 4.4. (a) True model (solid curve) versus reference model (dotted line) of the inverse series. The reference conductivity is 5 times larger than the background conductivity of the actual medium. (b) The convergence requirement of the inverse series, expression (4.16), is violated in the employed frequency range.

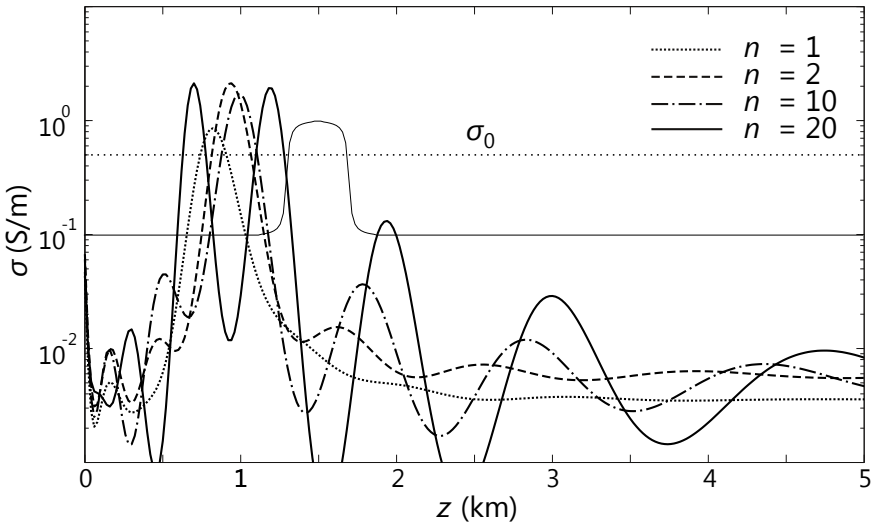

Figure 4.8. ISS solutions for the conductive anomaly model shown in Figure 4.7. The solutions are derived from equation (4.21) and compared for increasing order n of the inverse series. The thin solid curve denotes the true model. The ISS diverges.

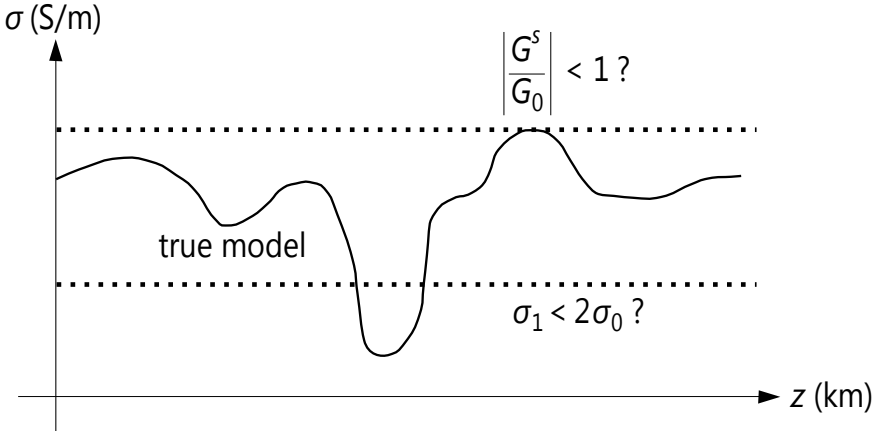

Figure 4.9. Dilemma of the ISS. A conductive reference model increases the possibility of violating the convergence condition of inverse series, expression (4.16). A resistive reference model, on the other hand, can result in the divergence of the left hand side of equation (4.20) and the inverse series itself. The range of the reference conductivity that allows convergence of the inverse series is limited by both the upper and lower bounds (dotted lines).

dilemma of choosing a reference model, which is inherent in the ISS procedure. Figure 4.9 summarizes the dilemma. As we choose a more conductive reference model, it is increasingly likely to violate the convergence condition of the inverse series in expression (4.16). On the other hand, the left hand side of equation (4.20) more readily diverges by choosing a more resistive reference model. The two contradictory conditions result in a narrow range of the reference model in which the ISS converges. This limitation of the ISS therefore necessitates an alternative approach of the inverse series. In this study, we remove the lower bound of convergence in Figure 4.9 and guarantee the convergence of the inverse series within a wider range of reference models.

4.5 1D formulation of modified inverse scattering series

As discussed in the previous section, the application of the ISS is limited by both the convergence condition of the inverse series and that of D_n, which is closely related to the forward series. We next remove the latter limitation. For electromagnetic diffusion, the iterative dissipative method (IDM) allows one to formulate an absolutely converging forward series for physically meaningful medium parameters, i.e., positive and finite electric conductivity. The IDM is also an efficient preconditioner that is necessary for large scale 3D electromagnetic forward problems (Avdeev, 2005). The IDM has been implemented for 3D electromagnetic problems (Avdeev *et al.*, 1997) and applied to forward simulations of field data (Kuvshinov *et al.*, 2005). In this study, we apply the IDM in an inverse sense and formulate an alternative approach of the inverse series: the modified inverse scattering series (MISS). The application of the modified approach is not restricted by the convergence condition of the forward series.

The basic idea of the IDM originates from the fact that the electric current created in a conductive medium by an external current source is smaller than the external current. The IDM is valid for arbitrary conductive media (Singer, 1995; Singer & Fainberg, 1995). The IDM transforms the Lippmann-Schwinger equation (4.5) into the following modified scattering equation (Avdeev *et al.*, 2002):

$$\chi(z, z_s; \omega) = \chi_0(z, z_s; \omega) + \int Q(z, z'; \omega)\, R(z')\, \chi(z', z_s; \omega)\, dz', \tag{4.26}$$

where

$$\chi(z, z_s; \omega) = \frac{1}{2\sqrt{\sigma_0(z)}}[\,(\sigma(z)+\sigma_0(z))\, G(z, z_s; \omega) - 2\sigma_0(z)\, G_0(z, z_s; \omega)\,], \tag{4.27}$$

$$\chi_0(z, z_s; \omega) = \int Q(z, z'; \omega)\sqrt{\sigma_0(z')}\, R(z') G_0(z', z_s; \omega)\, dz', \tag{4.28}$$

$$Q(z, z'; \omega) = \delta(z - z') + 2\sqrt{\sigma_0(z)}\; G_0(z, z'; \omega)\, \sqrt{\sigma_0(z')}, \tag{4.29}$$

and the conductivity ratio R is defined as

$$-1 \;<\; R(z) = \frac{\sigma(z) - \sigma_0(z)}{\sigma(z) + \sigma_0(z)} \;<\; 1. \tag{4.30}$$

Contrary to the Lippmann-Schwinger equation, the modified scattering equation has a contracting kernel QR such that

$$\forall \chi : \quad \left\| \int Q(z, z'; \omega)\, R(z')\, \chi(z', z_s; \omega)\, dz' \right\| < \|\chi\|, \tag{4.31}$$

where $\|\chi\|$ denotes the L_2-norm of χ (Pankratov *et al.*, 1995). Equation (4.26) therefore yields the following forward series that absolutely converges:

$$\chi = \chi_0 + QR\chi_0 + QRQR\chi_0 + \cdots . \tag{4.32}$$

In this modified forward series, the χ field is expressed as a series in order of the conductivity ratio R, and the true Green function G is subsequently derived using equation (4.27) from the χ field and electric conductivity at the receiver location.

In this study, we consider homogeneous reference models and rewrite equation (4.32) as

$$\frac{\chi}{\sqrt{\sigma_0}} = QRG_0 + QRQRG_0 + \cdots . \tag{4.33}$$

Following the procedure of the ISS presented in the previous section, we formulate the MISS that describes the conductivity ratio R as a series in order of the χ field:

$$R = R_1 + R_2 + R_3 + \cdots , \tag{4.34}$$

where R_n is the portion of R that is of the nth order of the χ field. We substitute the above series into equation (4.33), equate terms that are of the same order of the

χ field, and derive the following integral equation:

$$\begin{aligned}\tilde{D}_n(\chi, R_1, R_2, \cdots, R_{n-1}; \omega) \\ = \int Q(z, z'; \omega)\, R_n(z')\, G_0(z', z_s; \omega)\, dz',\end{aligned} \tag{4.35}$$

which allows one to iteratively solve for R_n from the measured χ field and all of the lower order terms of the modified inverse series. Note that for the evaluation of the χ field, we require both the electric conductivity at the receiver location and the scattered field (equation (4.27)). As in the case of the ISS, $\tilde{D}_n$ consists of $2^{n-1} - 1$ terms for higher order cases. In this study, we locate the source and receiver at the same position ($z = 0$), assume that the reference conductivity at the location is the true electric conductivity, and establish the following relation in operator form:

$$QR_lQR_mG_0 = QR_mQR_lG_0, \tag{4.36}$$

where l and m are arbitrary. The above relation simplifies $\tilde{D}_n$ to

$$\tilde{D}_n = \begin{cases} \chi/\sqrt{\sigma_0} & (n = 1), \\ -QR_1QR_1G_0 & (n = 2), \\ -QR_1\tilde{D}_{n-1} & (n = 3, 4, \cdots). \end{cases} \tag{4.37}$$

Since QR_1 is a contracting kernel, $\tilde{D}_n$ does not diverge. The convergence of $\tilde{D}_n$ implies that we resolve the dilemma of the ISS and remove the lower limit of convergence in Figure 4.9. The reference Green function is given by equation (4.17), and equation

(4.35) is expressed as

$$\begin{aligned}\tilde{D}_n(\omega) &= R_n(z)\, G_0(z, z_s; \omega) \\ &\quad + \int G_0(z, z'; \omega)\, R_n(z')\, G_0(z', z_s; \omega)\, dz' \\ &= \left(\frac{\omega\mu}{2k_0}\right)^2 \int 2\sigma_0 e^{ik_0(|z-z'|+|z'-z_s|)} R_n(z')\, dz', \end{aligned} \tag{4.38}$$

where we apply that the reference conductivity is the true electric conductivity at the receiver location ($R_n(z) = 0$). Note the similarity between the equation above and equation (4.20). We iteratively solve equations (4.37) and (4.38) for R_n and reconstruct the electric conductivity from

$$\sigma(z) = \sigma_0 \frac{1 + \sum R_n(z)}{1 - \sum R_n(z)}. \tag{4.39}$$

4.6 Model tests of modified inverse scattering series

In this section, we identify a different convergence pattern between the ISS and MISS for three representative models: resistive, conductive, and complex anomaly models. We also discuss the difference between the inversion results from the ISS and MISS. The input electric field data are identical for the two cases. The stabilizing functional Φ_m however is not identical. As shown in equation (4.22), the implemented ISS approach recovers models that exhibit a smooth variation in terms of the logarithm of the electric conductivity. The MISS, on the other hand, regularize the conductivity ratio R as

$$\Phi_m = \int \left(w(z) \frac{d^2 R}{dz^2} \right)^2 dz, \tag{4.40}$$

where $w(z)$ is the same depth weighting factor as the ISS. Therefore, the trade-off coefficient β should be different from the model tests of the ISS, and we derive the model-dependent coefficient from an independent L-curve analysis. We also require the trade-off coefficient to yield a physically valid electric conductivity: $-1 < R < 1$. The rest of the MISS procedure is identical to that of the ISS procedure.

4.6.1 Resistive anomaly model

We consider the model of Figures 4.2 and 4.3. Figure 4.10 shows that as in the case of the ISS, the MISS converges for the resistive anomaly model. The convergence criterion illustrated in Figure 4.2(b) adequately predicts the convergence of the modified inverse series. The convergence pattern also shows that the Born approximation ($n = 1$) contributes most to the model reconstruction of this resistive structure, and the contribution of the higher order terms are less significant.

Figure 4.11 compares the two solutions from the ISS and MISS. The difference between the two inversion results are insignificant near the origin and becomes more obvious near the resistive target. This difference originates from the fact that the relatively conductive background medium shields the resistive structure, and the reconstruction of the resistive target is physically limited. As a result, the inverse problem is ill-posed, and the solutions shown in Figure 4.11 are constrained by the employed regularization. Since the regularization acts on different functions in the ISS and MISS (M and R, respectively) with different regularization parameters, the reconstructed models differ. With respect to the location and conductivity value of the reconstructed resistive structure, the MISS yields a model that is closer to the true model (solid curve) than the ISS. From equations (4.21) and (4.39), we can express the differential dependence of the electric conductivity on the two parameters

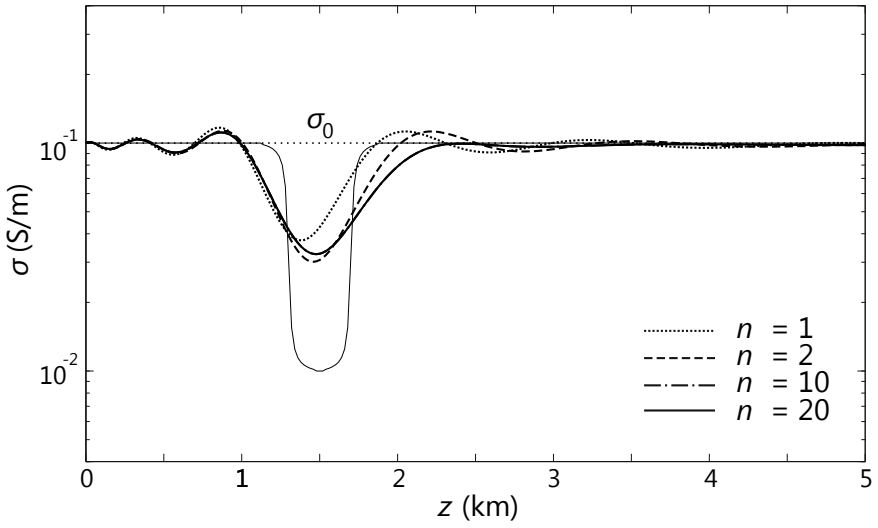

Figure 4.10. MISS solutions for the resistive anomaly model shown in Figure 4.2. The solutions are derived from equation (4.39) and compared for increasing order n of the inverse series. The thin solid curve denotes the true model. Both the ISS (Figure 4.3) and MISS converge.

M and R as

$$\frac{\partial \sigma}{\partial M} = \sigma_0 e^M = \sigma \tag{4.41}$$

and

$$\frac{\partial \sigma}{\partial R} = \frac{2\sigma_0}{(1-R)^2} = \frac{(\sigma+\sigma_0)^2}{2\sigma_0}, \tag{4.42}$$

respectively, where M and R are the partial sums up to the nth order. These equations suggest that the variation of the electric conductivity depends more strongly on the

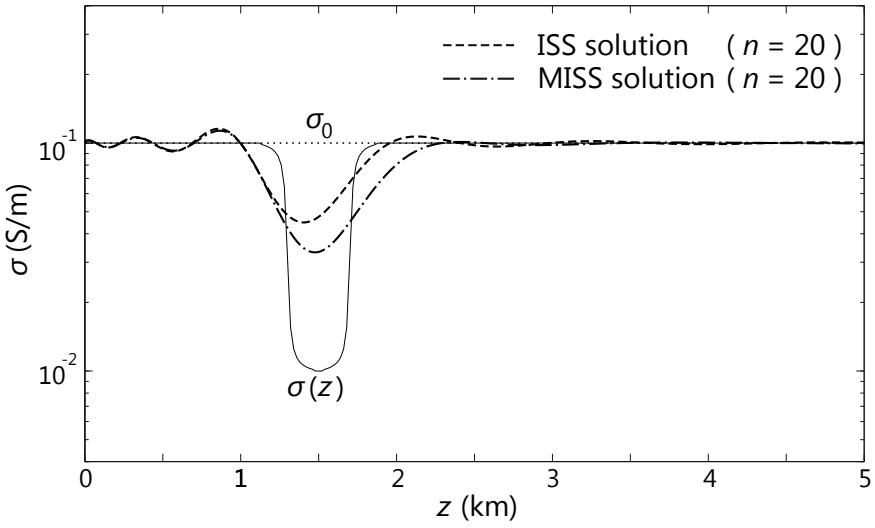

Figure 4.11. Comparison between the reconstructed models from the ISS and MISS for the resistive anomaly model shown in Figure 4.2. The MISS solution (dot-dashed curve) is closer to the true model (thin solid curve) than the model generated via the ISS (dashed curve).

conductivity ratio R than on the logarithm of the conductivity M:

$$\frac{\partial \sigma}{\partial M} < \frac{\partial \sigma}{\partial R}\,. \tag{4.43}$$

As depicted in Figure 4.11, the MISS therefore enables more detailed model reconstruction than the ISS.

4.6.2 Conductive anomaly model

Figures 4.4 and 4.5 illustrate that the ISS do not converge for the conductive anomaly model. This divergence arises from the fact that the electric conductivity from the Born approximation surpasses the approximate limit shown in expression (4.25), and the left hand side of equation (4.20), D_n, diverges (dashed curve in Figure

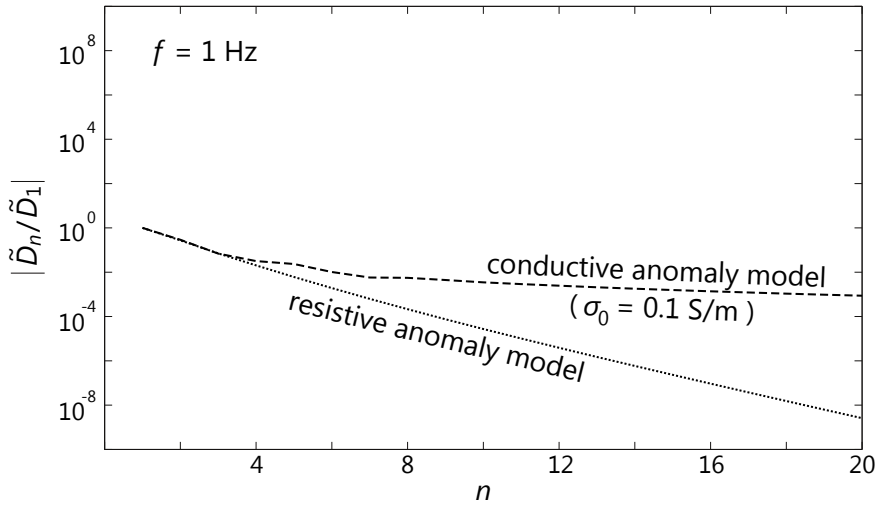

Figure 4.12. The left hand side of equation (4.38), $\tilde{D}_n$, as a function of the order n of the MISS for $f = 1$ Hz. The dotted and dashed curves represent the ratio $|\tilde{D}_n/\tilde{D}_1|$ for the models shown in Figures 4.2 and 4.4, respectively. Contrary to the case of the ISS (dashed curve in Figure 4.6), the ratio decreases for the conductive anomaly model.

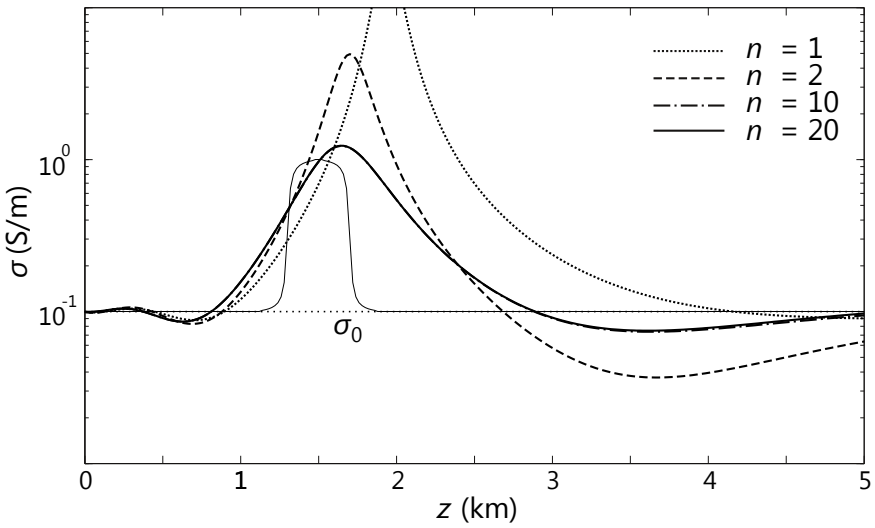

Figure 4.13. MISS solutions for the conductive anomaly model shown in Figure 4.4. The solutions are derived from equation (4.39) and compared for increasing order n of the inverse series. The thin solid curve denotes the true model. Contrary to the ISS (Figure 4.5), the MISS converges.

4.6). The MISS, on the other hand, is based on an absolutely converging forward series and free from the limitation. Figure 4.12 illustrates that for the same conductive anomaly model, the left hand side of equation (4.38), $\tilde{D}_n$, decreases. The MISS thus yields a solution that corresponds to the prediction of the convergence criterion in Figure 4.4(b) ($|G^s/G_0| < 1$). Figure 4.13 shows that contrary to the ISS, the MISS converges to a model that reveals the conductive anomaly structure. The convergence of the MISS demonstrates that it provides a converging solution for a larger contrast between the true and reference models than the ISS. Figure 4.14 compares the reconstructed model from the MISS with that from the Born approximation of the ISS. As in the case of the resistive anomaly model, the MISS solution is closer to the conductive target than the model retrieved via the ISS.

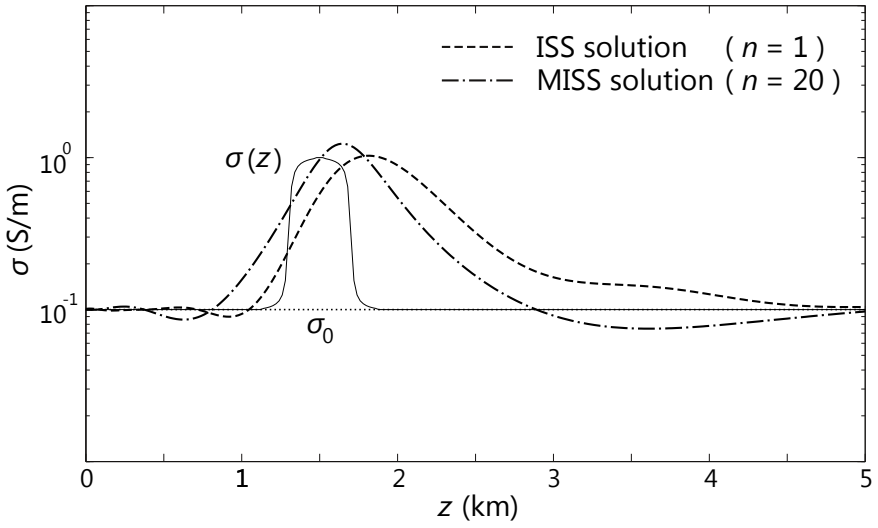

Figure 4.14. Comparison between the reconstructed models from the ISS and MISS for the conductive anomaly model shown in Figure 4.4. The MISS solution (dot-dashed curve) is closer to the true model (thin solid curve) than the model reconstructed by the Born approximation of the ISS (dashed curve).

4.6.3 Complex anomaly model

We consider a complicated conductivity structure that further highlights the advantage of the modified approach over the ISS. Figure 4.15(a) shows the true and reference conductivity distributions of the complex anomaly model, and Figure 4.15(b) depicts the ratio between the scattered field and reference Green function. Within the employed frequency range, the scattered field satisfies the convergence criterion of the inverse series in expression (4.16), and both the ISS and MISS converge (Figures 4.16 and 4.17). Compared to the previous models, the contribution of the higher order terms in the inverse series is more pronounced for the complex anomaly model. As a result, the solutions evaluated up to the 20th order are substantially different from the models reconstructed by the Born approximation, which suggests that the

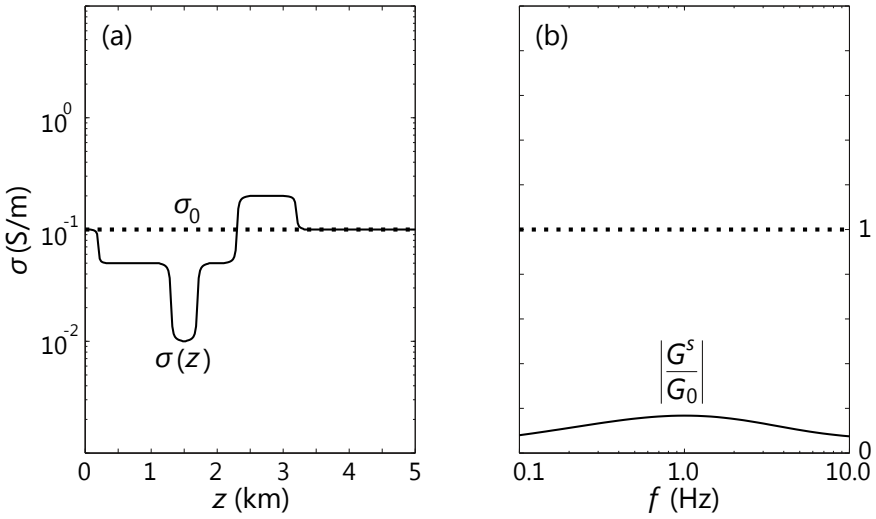

Figure 4.15. Complex anomaly model. (a) True model (solid curve) versus reference model (dotted line) of the inverse series. The reference conductivity is identical with the background conductivity of the true model. (b) The convergence requirement of the inverse series, expression (4.16), is satisfied in the employed frequency range.

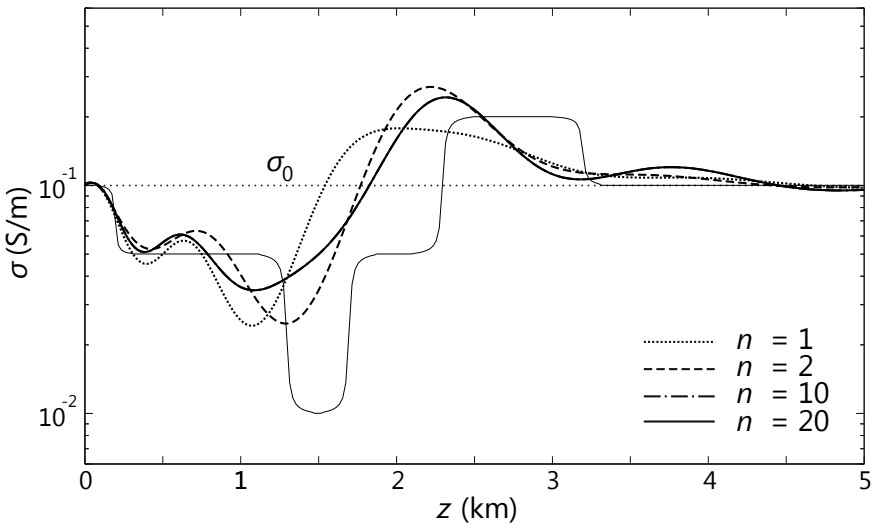

Figure 4.16. ISS solutions for the complex anomaly model shown in Figure 4.15. The solutions are derived from equation (4.21) and compared for increasing order n of the inverse series. The thin solid curve denotes the true model. The ISS converges.

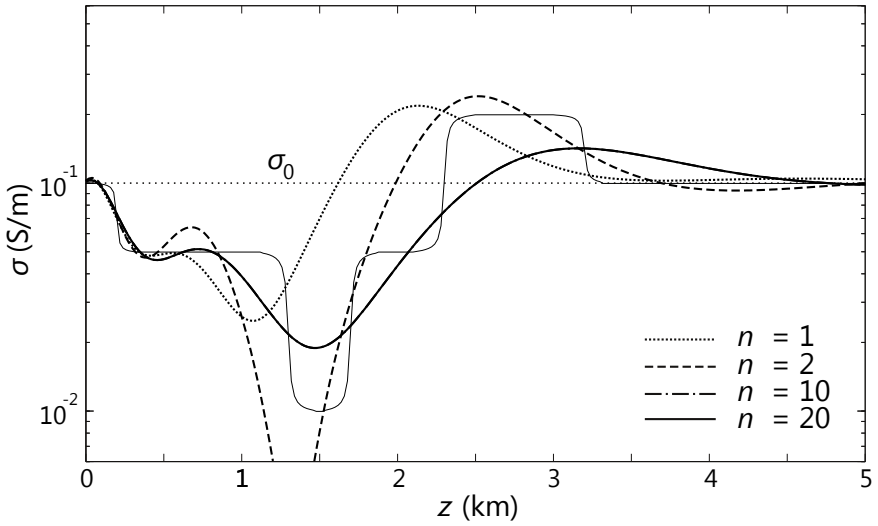

Figure 4.17. MISS solutions for the complex anomaly model shown in Figure 4.15. The solutions are derived from equation (4.39) and compared for increasing order n of the inverse series. The thin solid curve denotes the true model. Both the ISS (Figure 4.16) and MISS converge.

ISS and MISS are more significant with increasing model complexity. This reflects that the Born approximation cannot be expected to give a useful result for strongly non-linear problems (Snieder, 1990a).

Figure 4.18 compares the reconstructed models from the ISS and MISS. The difference between the two solutions is insignificant near the source/receiver location ($z = 0$) but increases with distance from that location. Note that the MISS recovers the resistive structure at $z = 1.3$ - 1.7 km, which the ISS fails to retrieve. This example demonstrates that compared to the ISS, the modified approach more effectively reconstructs the complicated conductivity structure. Combined with the previous model test that demonstrates the robust convergence of the MISS, the successful reconstruction of the complex anomaly structure manifests the superiority of the modified approach to the original.

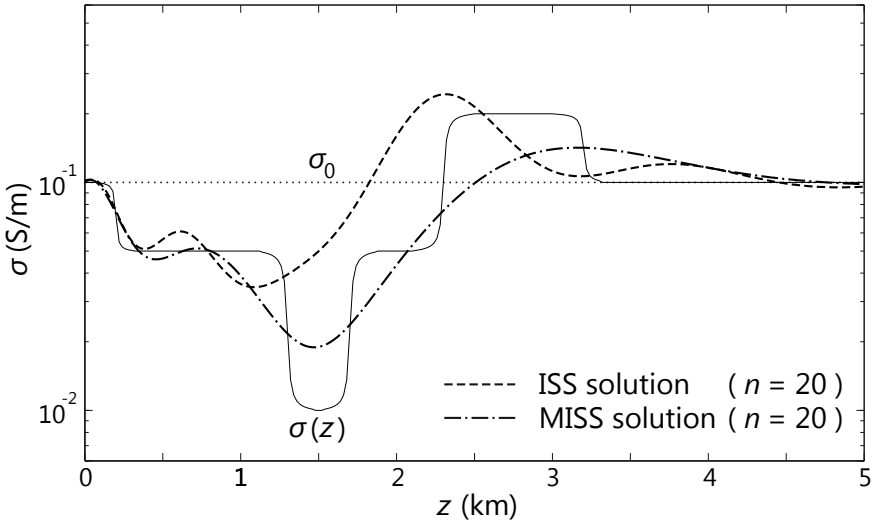

Figure 4.18. Comparison between the reconstructed models from the ISS and MISS for the complex anomaly model shown in Figure 4.15. The true (thin solid curve) and reference (dotted line) models are also depicted. The ISS does not retrieve the resistive structure at z = 1.3 - 1.7 km. The MISS, on the other hand, recovers the resistive structure.

4.7 Conclusions

We formulated the ISS and MISS for the 1D electromagnetic radiation geometry and identified the difference between the convergence patterns of the two approaches for three representative anomaly structures: the resistive, conductive, and complex anomaly models. We also studied the difference between the reconstructed models from the ISS and MISS. The analysis of the ISS shows that in addition to the convergence condition of the inverse series, there is another condition that determines the convergence/divergence of the ISS, and this condition is closely related to the convergence condition of the forward series. These two convergence conditions are contradictory and, as a result, strongly restrict the application of the ISS: the inverse series converges only for a narrow range of a reference conductivity that is close enough to a true model. The MISS, on the other hand, allows one to more freely choose a reference model, and the newly identified convergence condition no longer affects the convergence of the MISS. Moreover, the models reconstructed by the MISS are closer to the true models than the models generated via the ISS: the resistive target of the complex anomaly model is not identified by the ISS while the modified approach retrieves the target within the resolution limits of the inverse problem. In addition to the robust convergence, the estimate of the resistive target signifies that the MISS is more advantageous than the ISS for the reconstruction of electric conductivity, which varies in the order of magnitude within the subsurface.

The Born approximation plays the most significant role during the iterative model update of the inverse series. The contribution of the higher order terms is insignificant for the simple structures with an isolated resistive or conductive anomaly. The higher order terms, however, play a more significant role in the inversion with increasing model complexity: in the case of the complex anomaly model, the solution

evaluated up to the 20th order of the MISS is substantially different from the model retrieved from the Born approximation. In searching for a hydrocarbon reservoir, the electromagnetic inversion involves complex geological structures and is a computationally intensive process. The MISS is therefore an effective scheme that can provide a good starting model for more rigorous large-scale inversion for the three-dimensional conductivity structure of the subsurface. In this study, we consider the 1D radiation geometry shown in Figure 4.1, assume that the source and receiver are coincident, and simplify the left hand side of equations (4.20) and (4.38) as equations (4.15) and (4.37), respectively. However, the application of the MISS to more general cases is straightforward, and the conclusions deduced in this study are still valid for 3D radiation geometries and arbitrary source/receiver locations.

4.8 Acknowledgements

This work was supported by the Consortium Project on Seismic Inverse Methods for Complex Structures at Center for Wave Phenomena (CWP). We acknowledge Arthur Weglein (University of Houston), Dmitry Avdeev (Halliburton), and Yuanzhong Fan (Shell International) for helpful information, discussions, and suggestions. We are also grateful to colleagues of CWP for valuable discussions and technical help.

Chapter 5

CONCLUSION

We have analyzed two unconventional approaches of electromagnetic inversion: hierarchical Bayesian inversion and inverse scattering series. We applied the hierarchical Bayesian inversion to the uncertainty analysis for the joint inversion and utilized rock-physics models to integrate these two disparate data sets. Numerical simulations show that rock-physics model uncertainties play a more significant role on the overall uncertainty variation than do seismic and CSEM data noise. The numerical experiment also suggests different ways of accomplishing uncertainty reduction depending on whether our interests focus on porosity or on water saturation. When porosity is our prime concern, we can effectively accomplish uncertainty reduction by acquiring more precise P-wave velocity information and suppressing the seismic data noise. On the other hand, if we need a more accurate assessment of water saturation, the acquisition of more detailed electric conductivity information and the suppression of CSEM data noise are desirable. We have also studied the feasibility of the inverse scattering series (ISS), which can effectively resolve the nonlinearity of an inverse problem, for the interpretation of electromagnetic data. The application of the inverse scattering series is limited because the series converges when the reference model is sufficiently close to the true model. The analysis of the inverse scattering series shows that there are two contradictory conditions that determine the convergence/divergence of the series. These two conditions strongly restrict the application of the ISS: the inverse scattering series converges only for a narrow range of a reference conductivity that

is close enough to a true model. We have therefore suggested the modified inverse scattering series (MISS), which allows one to more freely choose a reference model, Moreover, the models reconstructed by the MISS are closer to the true models than the models generated via the original inverse scattering series: the resistive target of the complex anomaly model is not identified by the ISS while the modified approach retrieves the target within the resolution limits of the inverse problem. In addition to the robust convergence, the estimate of the resistive target signifies that the MISS is more advantageous than the ISS for the reconstruction of electric conductivity, which varies in the order of magnitude within the subsurface.

REFERENCES

Abubakar, A., Li, M., Liu, J., & Habashy, T. M. 2009. Simultaneous joint inversion of MT and CSEM data using a multiplicative cost function. *SEG Expanded Abstract*, **28**, 719 – 723.

Alumbaugh, D. L., Newman, G. A., Prevost, L., & Shadid, J. N. 1996. Three-dimensional wideband electromagnetic modeling on massively parallel computers. *Radio Science*, **31**(1), 1 – 23.

Archie, G. E. 1942. The Electrical Resistivity Log as an Aid in Determining Some Reservoir Characteristics. *Transactions of AIME*, **146**, 54 – 62.

Aster, R. C., Borchers, B., & Thurber, C. H. 2005. *Parameter Estimation and Inverse Problems*. Boston: Elsevier.

Avdeev, D. B. 2005. Three-dimensional electromagnetic modelling and inversion from theory to application. *Surveys in Geophysics*, **26**(6), 767 – 799.

Avdeev, D. B., Kuvshinov, A. V., Pankratov, O. V., & Newman, G. A. 1997. High-Performance Three-Dimensional Electromagnetic Modelling Using Modified Neumann Series. Wide-Band Numerical Solution and Examples. *Journal of Geomagnetism and Geoelectricity*, **49**, 1519 – 1539.

Avdeev, D. B., Kuvshinov, A. V., Pankratov, O. V., & Newman, G. A. 2002. Three-dimensional induction logging problems, Part I: An integral equation solution and model comparisons. *Geophysics*, **67**(2), 413 – 426.

Batzle, M., & Wang, Z. 1992. Seismic properties of pore fluids. *Geophysics*, **57**(11), 1396 – 1408.

Bayes, Rev . T. 1763. An essay towards solving a problem in the doctrine of chances. *Philosophical Transactions of the Royal Society of London*, **53**, 370 – 418.

Berenger, J. P. 1994. A Perfectly Matched Layer for the Absorption of Electromagnetic Waves. *Journal of Computational Physics*, **114**, 185 – 200.

Chave, A., & Cox, C. S. 1982. Controlled Electromagnetic Sources for Measuring Electrical Conductivity Beneath the Oceans 1. Forward Problem and Model Study. *Journal of Geophysical Research*, **87**(B7), 5327 – 5338.

Chen, J., & Dickens, T. A. 2009. Effects of uncertainty in rock-physics models on reservoir parameter estimation using amplitude variation with angle and controlled-source electromagnetics data. *Geophysical Prospecting*, **57**(1), 61 – 74.

Chen, J., Hoversten, G. M., Vasco, D., Rubin, Y., & Hou, Z. 2007. A Bayesian model for gas saturation estimation using marine seismic AVA and CSEM data. *Geophysics*, **72**(2), WA85 – WA95.

Colton, D., & Kress, R. 1998. *Inverse Acoustic and Electromagnetic Scattering Theory*. 2nd edn. Berlin: Springer.

Commer, M., & Newman, G. A. 2008. New advances in three-dimensional controlled-source electromagnetic inversion. *Geophysical Journal International*, **172**(2), 513 – 535.

Commer, M., & Newman, G. A. 2009. Three-dimensional controlled-source electromagnetic and magnetotelluric joint inversion. *Geophysical Journal International*, **178**(3), 1305 – 1316.

Constable, S., & Srnka, L. 2007. An introduction to marine controlled-source electromagnetic methods for hydrocarbon exploration. *Geophysics*, **72**(2), WA3 – WA12.

Constable, S. C., Parker, R. L., & Constable, C. G. 1987. Occam's inversion: A practical algorithm for generating smooth models from electromagnetic sounding data. *Geophysics*, **52**(3), 289 – 300.

Cox, C. S., Constable, S. C., Chave, A. D., & Webb, S. C. 1986. Controlled-source electromagnetic sounding of the oceanic lithosphere. *Nature*, **320**(6057), 52 – 54.

Docherty, P. 1987. *Ray theoretical modeling, migration and inversion in two-and-one-half-dimensional layered acoustic media*. Ph.D. thesis, Colorado School of Mines.

Dorren, H. J. S., & Snieder, R. 1997. Error propagation in non-linear delay-time tomography. *Geophysical Journal International*, **128**(3), 632 – 638.

Fan, Y., Snieder, R., Slob, E., Hunziker, J., Singer, J., Sheiman, J., & Rosenquist, M. 2010. Synthetic aperture controlled source electromagnetics. *Geophysical Research Letters*, **37**, L13305.

Fisher, R. A., Bennett, J. H., & Yates, F. 1990. *Statistical Methods, Experimental Design, and Scientific Inference*. New York: Oxford University Press.

Gallardo, L. A., & Meju, M. A. 2004. Joint two-dimensional DC resistivity and seismic travel time inversion with cross-gradients constraints. *Journal of Geophysical Research*, **109**, B03311.

Gassmann, F. 1951. Uber die elastizitat poroser medien. *Vierteljahrsschrift der Naturforschenden Gesellschaft in Zurich*, **96**, 1 – 23.

Gel'fand, I. M., & Levitan, B. M. 1951. On the determination of a differential equation from its spectral function. *Izvestiya Akademii Nauk SSSR Seriya Matematicheskaya*, **15**(4), 309 – 360.

Gelman, A., Carlin, J. B., Stern, H. S., & Rubin, D. B. 2003. *Bayesian Data Analysis*. 2nd edn. London: Chapman and Hall.

Geman, S., & Geman, D. 1984. Stochastic Relaxation, Gibbs distribution, and the Bayesian Restoration of Images. *IEEE Transactions on Pattern Analysis and Machine Intelligence*, **6**, 721 – 741.

Golub, G. H., & Reinsch, C. 1970. Singular value decomposition and least squares solutions. *Numerische Mathematik*, **14**(5), 403 – 420.

Gouveia, W. P., & Scales, J. A. 1998. Bayesian seismic waveform inversion: Parameter estimation and uncertainty analysis. *Journal of Geophysical Research*, **103**(B2), 2759 – 2779.

Gribenko, A., & Zhdanov, M. 2007. Rigorous 3D inversion of marine CSEM data based on the integral equation method. *Geophysics*, **72**(2), WA73 – WA84.

Habashy, T. M., Groom, R. W., & Spies, B. R. 1993. Beyond the Born and Rytov Approximations: A Nonlinear Approach to Electromagnetic Scattering. *Journal of Geophysical Research*, **98**(B2), 1759 – 1775.

Han, D., & Batzle, M. 2004. Gassmann's equation and fluid-saturation effects on seismic velocities. *Geophysics*, **69**(2), 398 – 405.

Hansen, P. C. 1992. Analysis of discrete ill-posed problems by means of the L-curve. *SIAM Review*, **34**(4), 561 – 580.

Harris, P., & MacGregor, L. 2006. Determination of reservoir properties from the integration of CSEM and seismic data. *First Break*, **24**(11), 53 – 59.

Hastings, W. K. 1970. Monte Carlo sampling methods using Markov chains and their applications. *Biometrika*, **57**(1), 97 – 109.

Hohmann, G. W. 1975. Three-dimensional induced polarization and electromagnetic modeling. *Geophysics*, **40**(2), 309 – 324.

Hoversten, G. M., Cassassuce, F., Gasperikova, E., Newman, G. A., Chen, J., Rubin, Y., Hou, Z., & Vasco, D. 2006. Direct reservoir parameter estimation using joint inversion of marine seismic AVA and CSEM data. *Geophysics*, **71**(3), C1 – C13.

Hu, W., Abubakar, A., & Habashy, T. M. 2009. Joint electromagnetic and seismic inversion using structural constraints. *Geophysics*, **74**(6), R99 – R109.

Jackson, D. D. 1972. Interpretation of inaccurate, insufficient and inconsistent data. *Geophysical Journal of the Royal Astronomical Society*, **28**(2), 97 – 109.

Jackson, J. D. 1999. *Classical Electrodynamics*. 3rd edn. New York: Wiley.

Jannane, M., Beydoun, W., Crase, E., Cao, D., Koren, Z., Landa, E., Mendes, M., Pica, A., Noble, M., Roeth, G., Singh, S., Snieder, R., Tarantola, A., Trezeguet, D., & Xie, M. 1989. Wavelengths of earth structures that can be resolved from seismic reflection data. *Geophysics*, **54**(7), 906 – 910.

Jost, R., & Kohn, W. 1952. Construction of a Potential from a Phase Shift. *Physical Review*, **87**(6), 977 – 992.

Kaipio, J. P., Kolehmainen, V., Somersalo, E., & Vauhkonen, M. 2000. Statistical inversion and Monte Carlo sampling methods in electrical impedance tomography. *Inverse Problems*, **16**(5), 1487 – 1522.

Kuvshinov, A., Utada, H., Avdeev, D., & Koyama, T. 2005. 3-D modelling and analysis of Dst C-responses in the North Pacific Ocean region, revisited. *Geophysical Journal International*, **160**(2), 505 – 526.

Kwon, M. J., & Snieder, R. 2010. Comparison of scattering series solutions for acoustic wave and electromagnetic diffusion equations. *SEG Expanded Abstract*, **29**, 758 – 763.

Kwon, M. J., & Snieder, R. 2011a. 1D electromagnetic model reconstruction by modified inverse scattering series. *SEG Expanded Abstract*, **30**.

Kwon, M. J., & Snieder, R. 2011b. Uncertainty analysis for the integration of seismic and CSEM data. *Geophysical Prospecting*, **59**.

Lippmann, B. A., & Schwinger, J. 1950. Variational Principles for Scattering Processes. I. *Physical Review*, **79**(3), 469 – 480.

Mavko, G., Mukerji, T., & Dvorkin, J. 1998. *The Rock Physics Handbook - Tools for Seismic Analysis in Porous Media*. Cambridge: Cambridge University Press.

Metropolis, N., Rosenbluth, A. W., Rosenbluth, M. N., & Teller, A. H. 1953. Equation of State Calculations by Fast Computing Machines. *The Journal of Chemical Physics*, **21**(6), 1087 – 1092.

Morse, P. M., & Feshbach, H. 1953. *Methods of Theoretical Physics*. New York: McGraw-Hill.

Mosegaard, K., & Sambridge, M. 2002. Monte Carlo analysis of inverse problems. *Inverse Problems*, **18**(3), R29 – R54.

Mosegaard, K., Singh, S., Snyder, D., & Wagner, H. 1997. Monte Carlo analysis of seismic reflections from Moho and the W reflector. *Journal of Geophysical Research*, **102**(B2), 2969 – 2981.

Moses, H. E. 1956. Calculation of the Scattering Potential from Reflection Coefficients. *Physical Review*, **102**(2), 559 – 567.

Musil, M., Maurer, H. R., & Green, A. G. 2003. Discrete tomography and joint inversion for loosely connected or unconnected physical properties: application to crosshole seismic and georadar data sets. *Geophysical Journal International*, **153**(2), 389 – 402.

Newman, G. A., & Alumbaugh, D. L. 1997. Three-dimensional massively parallel electromagnetic inversion - I. Theory. *Geophysical Journal International*, **128**(2), 345 – 354.

Palacky, G. J. 1987. Resistivity characteristics of geologic targets. Electromagnetic methods in applied geophysics. Tulsa: Society of Exploration Geophysicists.

Pankratov, O. V., Avdeev, D. B., & Kuvshinov, A. V. 1995. Electromagnetic field scattering in a heterogeneous Earth: A solution to the forward problem. *Physics of the Solid Earth*, **31**(3), 201 – 209.

Parker, R. L. 1977. Understanding Inverse Theory. *Annual Review of Earth and Planetary Sciences*, **5**, 35 – 64.

Pratt, R. G. 1999. Seismic waveform inversion in the frequency domain, Part 1: Theory and verification in a physical scale model. *Geophysics*, **64**(3), 888 – 901.

Pridmore, D. F., Hohmann, G. W., Ward, S. H., & Sill, W. R. 1981. An investigation of finite-element modeling for electrical and electromagnetic data in three dimensions. *Geophysics*, **46**(7), 1009 – 1024.

Prosser, R. T. 1969. Formal Solutions of Inverse Scattering Problems. *Journal of Mathematical Physics*, **10**(10), 1819 – 1822.

Prosser, R. T. 1976. Formal Solutions of Inverse Scattering Problems. II. *Journal of Mathematical Physics*, **17**(10), 1775 – 1779.

Ramirez, A. C., & Weglein, A. B. 2009. Green's theorem as a comprehensive framework for data reconstruction, regularization, wavefield separation, seismic interferometry and wavelet estimation: A tutorial. *Geophysics*, **74**(6), W35 – W62.

Revil, A., Cathles, L. M., & Losh, S. 1998. Electrical conductivity in shaly sands with geophysical applications. *Journal of Geophysical Research*, **103**(B10), 23925 – 23936.

Sambridge, M., Beghein, C., Simons, F. J., & Snieder, R. 2006. How do we understand and visualize uncertainty? *The Leading Edge*, **25**(5), 542 – 546.

Scales, J. A., & Tenorio, L. 2001. Prior information and uncertainty in inverse problems. *Geophysics*, **66**(2), 389 – 397.

Singer, B. Sh. 1995. Method for solution of Maxwell's equations in non-uniform media. *Geophysical Journal International*, **120**(3), 590 – 598.

Singer, B. Sh., & Fainberg, E. B. 1995. Generalization of the iterative dissipative method for modeling electromagnetic fields in nonuniform media with displacement current. *Journal of Applied Geophysics*, **34**, 41 – 46.

Snieder, R. 1990a. A perturbative analysis of non-linear inversion. *Geophysical Journal International*, **101**(3), 545 – 556.

Snieder, R. 1990b. The role of the Born approximation in nonlinear inversion. *Inverse Problems*, **6**(2), 247 – 266.

Snieder, R. 1998. The role of nonlinearity in inverse problems. *Inverse Problems*, **14**(3), 387 – 404.

Snieder, R., Xie, M. Y., Pica, A., & Tarantola, A. 1989. Retrieving both the impedance contrast and background velocity: A global strategy for the seismic reflection problem. *Geophysics*, **54**(8), 991 – 1000.

Spikes, K., Mukerji, T., Dvorkin, J., & Mavko, G. 2007. Probabilistic seismic inversion based on rock-physics models. *Geophysics*, **72**(5), R87 – R97.

Srnka, L., Carazzone, J. J., Ephron, M. S., & Eriksen, E. A. 2006. Remote reservoir resistivity mapping. *The Leading Edge*, **25**(8), 972 – 975.

Tarantola, A. 2005. *Inverse Problem Theory and Methods for Model Parameter Estimation*. Philadelphia: Society for Industrial and Applied Mathematics.

Telford, W. M., Geldart, L. P., & Sheriff, R. E. 1990. *Applied Geophysics*. 2nd edn. New York: Cambridge University Press.

Tenorio, L. 2001. Statistical Regularization of Inverse Problems. *SIAM Review*, **43**(2), 347 – 366.

Tikhonov, A. N., & Arsenin, V. Y. 1977. *Solution of Ill-posed Problems*. Washington: Winston.

Torres-Verdin, C., & Habashy, T. M. 2001. Rapid numerical simulation of axisymmetric single-well induction data using the extended Born approximation. *Radio Science*, **36**(6), 1287 – 1306.

Ulrych, T. J., Sacchi, M. D., & Woodbury, A. 2001. A Bayes tour of inversion: A tutorial. *Geophysics*, **66**(1), 55 – 69.

Um, E. S., Harris, J. M., & Alumbaugh, D. L. 2010. 3D time-domain simulation of electromagnetic diffusion phenomena: A finite-element electric-field approach. *Geophysics*, **75**(4), F115 – F126.

Virieux, J., & Operto, S. 2009. An overview of full-waveform inversion in exploration geophysics. *Geophysics*, **74**(6), WCC1 – WCC26.

Waxman, M. H., & Smits, L. J. M. 1968. Electrical conductivities in oil-bearing shaly sands. *Society of Petroleum Engineering Journal*, **8**(2), 107 – 122.

Weglein, A. B., Boyse, W. E., & Anderson, J. E. 1981. Obtaining three-dimensional velocity information directly from reflection seismic data: An inverse scattering formalism. *Geophysics*, **46**(8), 1116 – 1120.

Weglein, A. B., Gasparotto, F. A., Carvalho, P. M., & Stolt, R. H. 1997. An inverse-scattering series method for attenuating multiples in seismic reflection data. *Geophysics*, **62**(6), 1975 – 1989.

Weglein, A. B., Araujo, F. V., Carvalho, P. M., Stolt, R. H., Matson, K. H., Coates, R. T., Corrigan, D., Foster, D. J., Shaw, S. A., & Zhang, H. 2003. Inverse Scattering series and seismic exploration. *Inverse Problems*, **19**(6), R27 – R83.

Weglein, A. B., Zhang, H., Ramirez, A. C., Liu, F., & Lira, J. E. M. 2009. Clarifying the underlying and fundamental meaning of the approximate linear inversion of seismic data. *Geophysics*, **74**(6), WCD1 – WCD13.

Weglein, A. B., Liu, F., Wang, Z., Li, X., & Liang, H. 2010. The inverse scattering series depth imaging algorithms: development, tests and progress towards field data applications. *SEG Expanded Abstract*, **29**, 4133 – 4138.

Wood, A. W. 1955. *A Textbook of Sound*. London: The MacMillan Co.

Yee, K. S. 1966. Numerical Solution of Initial Boundary Value Problems Involving Maxwell's Equations in Isotropic Media. *IEEE Transactions on Antennas and Propagation*, **14**, 302 – 307.

Yilmaz, O. 1987. *Seismic Data Processing*. Tulsa: Society of Exploration Geophysicists.

Zhang, H., & Weglein, A. B. 2009a. Direct non-linear inversion of multi-parameter 1D elastic media using the inverse scattering series. *Geophysics*, **74**(6), WCD15 – WCD27.

Zhang, H., & Weglein, A. B. 2009b. Direct nonlinear inversion of 1D acoustic media using inverse scattering subseries. *Geophysics*, **74**(6), WCD29 – WCD39.

Zhdanov, M. S. 2002. *Geophysical Inverse Theory and Regularization Problems*. Amsterdam: Elsevier.

Zhdanov, M. S., Lee, S. K., & Yoshioka, K. 2006. Integral equation method for 3D modeling of electromagnetic fields in complex structures with inhomogeneous background conductivity. *Geophysics*, **71**(6), G333 – G345.

APPENDIX A

METROPOLIS-HASTINGS ALGORITHM

The Metropolis-Hastings algorithm (Metropolis *et al.*, 1953; Hastings, 1970) is a method for generating a sequence of samples from a probability distribution that is difficult to sample directly. The actual implementation of the algorithm is comprised of the following steps.

1. Pick an initial sample $\mathbf{m}_{prev} \in \mathbb{R}^n$ and set $k = 1$, $\mathbf{m}^{(k)} = \mathbf{m}_{prev}$.

2. Increase $k \to k + 1$.

3. Draw a proposal sample $\mathbf{m}_{prop} \in \mathbb{R}^n$ from the proposal distribution $q(\mathbf{m}_{prev}, \mathbf{m}_{prop})$ and calculate the acceptance ratio

$$\alpha(\mathbf{m}_{prev}, \mathbf{m}_{prop}) = \min\left[1, \frac{\pi_{post}(\mathbf{m}_{prop})q(\mathbf{m}_{prop}, \mathbf{m}_{prev})}{\pi_{post}(\mathbf{m}_{prev})q(\mathbf{m}_{prev}, \mathbf{m}_{prop})}\right]. \tag{A.1}$$

4. Draw $t \in [0, 1]$ from uniform probability density.

5. If $\alpha(\mathbf{m}_{prev}, \mathbf{m}_{prop}) \geq t$, set $\mathbf{m}^{(k)} = \mathbf{m}_{prop}$; otherwise, $\mathbf{m}^{(k)} = \mathbf{m}_{prev}$.

6. When k is the desired sample size, stop; otherwise, repeat the procedure starting with step (2).

We choose a Gaussian distribution as a proposal distribution as follows:

$$\mathbf{m}_{prop} \sim N(\mathbf{m}_{prev}, \sigma_i^2\mathbf{I}), \tag{A.2}$$

where the variances σ_i^2 describe the probabilistic sampling step of the model parameters during the random simulation. If σ_i^2 is too large, the drawn $\mathbf{m}_{prop}$ is practically never accepted. On the other hand, if σ_i^2 is too small, a proper sampling of the distribution requires a prohibitively large sample set. A good rule of thumb is that roughly 20 - 30% of all $\mathbf{m}_{prop}$ should be accepted (Kaipio *et al.*, 2000).

APPENDIX B

ROCK-PHYSICS MODELS OF THIS STUDY

P-wave velocity V_p is defined as function of bulk modulus K, shear modulus μ, and density ρ, such that

$$V_p = \sqrt{\frac{K + \frac{4}{3}\mu}{\rho}}. \tag{B.1}$$

The bulk modulus K is related to porosity ϕ and water saturation S_w. For a fluid saturated medium, the bulk modulus is given by Gassmann's equation (Gassmann, 1951; Han & Batzle, 2004) as follows:

$$K = K_d + \frac{(1 - \frac{K_d}{K_0})^2}{\frac{\phi}{K_f} + \frac{1-\phi}{K_0} - \frac{K_d}{K_0^2}}, \tag{B.2}$$

where K_d, K_0, and K_f are the bulk modulus of the dry rock, mineral material, and pore fluid, respectively. We model two phases of pore fluid: water and gas. A mixture of two different pore fluids can be regarded as an effective fluid model and the bulk modulus is derived from Wood's equation (Wood, 1955; Batzle & Wang, 1992) as follows:

$$\frac{1}{K_f} = \frac{S_w}{K_w} + \frac{1 - S_w}{K_g}, \tag{B.3}$$

where K_w and K_g are the bulk modulus of the water and gas phases. We also relate the bulk modulus of the dry rock K_d and shear modulus μ with porosity ϕ as follows:

$$K_d = K_0 \left(1 - \frac{\phi}{\phi_c}\right), \tag{B.4}$$

$$\mu = \mu_0 \left(1 - \frac{\phi}{\phi_c}\right), \tag{B.5}$$

where μ_0 is the shear modulus of mineral material, and ϕ_c is the critical porosity which is the threshold porosity value between the suspension and the load-bearing domain. Finally, we model the dependence of density ρ on porosity and water saturation as:

$$\rho = \phi S_w \rho_w + (1 - \phi)\rho_0, \tag{B.6}$$

where ρ_w and ρ_0 are the density of water phase and mineral material, respectively.

The relationship between the reservoir parameters and electric conductivity is first given by Archie's second law (Archie, 1942), which describes electric conductivity in clean sands. In fact, electric conductivity in shaley sands is complicated by the presence of clays and is described by Waxman-Smits formula (Waxman & Smits, 1968):

$$\sigma_e = \phi^m S_w^n \left[\sigma_w + \frac{BQ_v}{S_w}\right], \tag{B.7}$$

where m is the cementation exponent, n is saturation exponent, and σ_w is electric conductivity of pore fluid. The parameter B is an equivalent counterion mobility and Q_v is the excess of surface charge per unit pore volume. The parameter B is given

empirically at 25°C by

$$B = B_0 \left[1 - 0.6 \exp\left(-\frac{\sigma_w}{0.013}\right)\right], \tag{B.8}$$

where σ_w is in S/m and the maximum counterion mobility B_0 is given by $4.78 \times 10^{-8}\mathrm{m}^2/\mathrm{V/s}$ (Revil *et al.*, 1998). The parameter Q is related to the mineral density ρ_0 (in $\mathrm{kg/m}^3$) and the cation exchange capacity (CEC) by

$$Q_v = \rho_0 \frac{1-\phi}{\phi} \mathrm{CEC}. \tag{B.9}$$

The CEC is only significant for clay minerals, and the variation of CEC for different clay minerals is dramatic.

The modeled values of each rock physics parameters introduced above are summarized in Table 2.1.

APPENDIX C

THE nTH ORDER DERIVATIVE OF $F(z) = \exp(a\sqrt{1+z} - a) - 1$

We prove that given a complex number a and complex variable z, the nth order derivative of a complex function,

$$F(z) = e^{a\sqrt{1+z}-a} - 1, \tag{C.1}$$

is expressed as

$$\frac{d^n F}{dz^n} = \frac{1}{2^n} \sum_{m=1}^{n} \beta_{n,m} a^{n-m+1} (1+z)^{-\frac{n+m-1}{2}} \, e^{a\sqrt{1+z}-a}, \tag{C.2}$$

where

$$\beta_{n,m} = \begin{cases} 1 & (m = 1), \\ -\dfrac{\beta_{n,m-1}}{m-1} \displaystyle\sum_{l=m-1}^{n-1} l & (m = 2, 3, 4, \cdots, n). \end{cases} \tag{C.3}$$

Direct differentiation of equation (C.1) yields

$$\frac{dF}{dz} = \frac{a}{2\sqrt{1+z}} \, e^{a\sqrt{1+z}-a}. \tag{C.4}$$

For $n = 1$, equations (C.2) and (C.3) give

$$\frac{dF}{dz} = \frac{1}{2}\beta_{1,1}a(1+z)^{-\frac{1}{2}}\, e^{a\sqrt{1+z}-a} = \frac{a}{2}(1+z)^{-\frac{1}{2}}\, e^{a\sqrt{1+z}-a}, \tag{C.5}$$

which is the same result with the direct differentiation of $F(z)$. From equation (C.2), we write the $(n-1)$th order derivative of $F(z)$ as

$$\frac{d^{n-1}F}{dz^{n-1}} = \frac{1}{2^{n-1}}\sum_{m=1}^{n-1}\beta_{n-1,m}\, a^{n-m}(1+z)^{-\frac{n+m-2}{2}}\, e^{a\sqrt{1+z}-a} \tag{C.6}$$

for any integer $n \geq 2$. Differentiating equation (C.6), we derive

$$\begin{aligned}
\frac{d^nF}{dz^n} &= \frac{1}{2^n}\sum_{m=1}^{n-1}\beta_{n-1,m}\, a^{n-m+1}(1+z)^{-\frac{n+m-1}{2}}\, e^{a\sqrt{1+z}-a} \\
&- \frac{1}{2^n}\sum_{m=1}^{n-1}(n+m-2)\beta_{n-1,m}\, a^{n-m}(1+z)^{-\frac{n+m}{2}}\, e^{a\sqrt{1+z}-a} \\
&= \frac{1}{2^n}\sum_{m=1}^{n-1}\beta_{n-1,m}\, a^{n-m+1}(1+z)^{-\frac{n+m-1}{2}}\, e^{a\sqrt{1+z}-a} \\
&- \frac{1}{2^n}\sum_{m=2}^{n}(n+m-3)\beta_{n-1,m-1}\, a^{n-m+1}(1+z)^{-\frac{n+m-1}{2}}\, e^{a\sqrt{1+z}-a}.
\end{aligned} \tag{C.7}$$

Rearranging terms, we express the nth order derivative of $F(z)$ as

$$\begin{aligned}
\frac{d^nF}{dz^n} &= \frac{1}{2^n}\beta_{n-1,1}\, a^n(1+z)^{-\frac{n}{2}}\, e^{a\sqrt{1+z}-a} \\
&+ \frac{1}{2^n}\sum_{m=2}^{n-1}\left[\beta_{n-1,m} - (n+m-3)\beta_{n-1,m-1}\right] a^{n-m+1}(1+z)^{-\frac{n+m-1}{2}}\, e^{a\sqrt{1+z}-a} \\
&- \frac{1}{2^n}(2n-3)\beta_{n-1,n-1}\, a(1+z)^{-\frac{2n-1}{2}}\, e^{a\sqrt{1+z}-a}.
\end{aligned} \tag{C.8}$$

We apply the recursive relations of $\beta_{n,m}$ (Appendix D) and simplify the above expres-

sion as

$$\begin{aligned}
\frac{d^n F}{dz^n} &= \frac{1}{2^n}\beta_{n,1}\, a^n (1+z)^{-\frac{n}{2}}\, e^{a\sqrt{1+z}-a} \\
&+ \frac{1}{2^n}\sum_{m=2}^{n-1}\beta_{n,m}\, a^{n-m+1}(1+z)^{-\frac{n+m-1}{2}}\, e^{a\sqrt{1+z}-a} \\
&+ \frac{1}{2^n}\beta_{n,n}\, a(1+z)^{-\frac{2n-1}{2}}\, e^{a\sqrt{1+z}-a} \\
&= \frac{1}{2^n}\sum_{m=1}^{n}\beta_{n,m}\, a^{n-m+1}(1+z)^{-\frac{n+m-1}{2}}\, e^{a\sqrt{1+z}-a}, \qquad \text{(C.9)}
\end{aligned}$$

which conforms with equation (C.2). Q.E.D.

APPENDIX D

RECURSIVE RELATIONS OF $\beta_{n,m}$

Given an integer $n \geq 1$, we define the following recursive formula:

$$\beta_{n,m} = \begin{cases} 1 & (m = 1), \\ -\dfrac{\beta_{n,m-1}}{m-1} \displaystyle\sum_{l=m-1}^{n-1} l & (m = 2, 3, 4, \cdots, n), \end{cases} \tag{D.1}$$

for any integer $n \geq m \geq 1$, and prove the following relations:

$$\beta_{n,1} = \beta_{n-1,1}, \tag{D.2}$$

$$\beta_{n,m} = \beta_{n-1,m} - (n+m-3)\beta_{n-1,m-1} \quad (m = 2, 3, 4, \cdots, n-1), \tag{D.3}$$

$$\beta_{n,n} = -(2n-3)\beta_{n-1,n-1}. \tag{D.4}$$

It is obvious from the definition that

$$\beta_{n,1} = \beta_{n-1,1} = 1. \quad \text{Q.E.D.} \tag{D.5}$$

We prove equation (D.3) by rewriting it as

$$\begin{aligned}\beta_{n,m} &= \beta_{n-1,m} - (n+m-3)\beta_{n-1,m-1} \\ &= -\frac{\beta_{n-1,m-1}}{m-1}\sum_{l=m-1}^{n-2} l - (n+m-3)\beta_{n-1,m-1} \\ &= -\frac{\beta_{n-1,m-1}}{m-1}\left[\sum_{l=1}^{n-2} l - \sum_{l=1}^{m-2} l\right] - (n+m-3)\beta_{n-1,m-1}. \end{aligned} \tag{D.6}$$

After an algebraic calculation, we can simplify the above equation as

$$\beta_{n,m} = -\beta_{n-1,m-1}\frac{(n+m-2)(n+m-3)}{2(m-1)}. \tag{D.7}$$

For $m = 2$, equation (D.7) becomes

$$\beta_{n,2} = -\beta_{n-1,1}\frac{n(n-1)}{2} = -\sum_{l=1}^{n-1} l, \tag{D.8}$$

which is the same result with the definition in equation (D.1). From equation (D.7), we write $\beta_{n,m-1}$ for any $m \geq 3$ as

$$\beta_{n,m-1} = -\beta_{n-1,m-2}\frac{(n+m-3)(n+m-4)}{2(m-2)}. \tag{D.9}$$

We also establish the following relation from the definition:

$$\beta_{n-1,m-1} = -\frac{\beta_{n-1,m-2}}{m-2}\sum_{l=m-2}^{n-2} l. \tag{D.10}$$

Therefore, $\beta_{n,m}$ is written as

$$\begin{aligned}\beta_{n,m} &= -\frac{\beta_{n,m-1}}{m-1}\sum_{l=m-1}^{n-1} l = -\beta_{n-1,m-1}\frac{(n+m-3)(n+m-4)}{2(m-1)}\frac{\sum_{l=m-1}^{n-1} l}{\sum_{l=m-2}^{n-2} l} \\ &= -\beta_{n-1,m-1}\frac{(n+m-3)(n+m-4)}{2(m-1)}\frac{\sum_{l=1}^{n-1} l - \sum_{l=1}^{m-2} l}{\sum_{l=1}^{n-2} l - \sum_{l=1}^{m-3} l}. \qquad \text{(D.11)}\end{aligned}$$

We can simplify the above equation as

$$\beta_{n,m} = -\beta_{n-1,m-1}\frac{(n+m-2)(n+m-3)}{2(m-1)}, \qquad \text{(D.12)}$$

which conforms with equation (D.7). Q.E.D.

Applying $m = n$ to equation (D.7), we derive

$$\beta_{n,n} = -(2n-3)\beta_{n-1,n-1}, \qquad \text{(D.13)}$$

which is identical to equation (D.4). Q.E.D.

APPENDIX E

THE nTH ORDER DERIVATIVE OF $F(z) = [\ln(1+z)]^2$

We prove that given a complex function $F(z)$ of a complex variable z,

$$F(z) = [\ln(1+z)]^2, \tag{E.1}$$

the nth order derivative of $F(z)$ is

$$\frac{d^n F}{dz^n} = -2\eta_n(1+z)^{-n} + 2(-1)^{n-1}(n-1)!(1+z)^{-n}\ln(1+z), \tag{E.2}$$

where

$$\eta_n = \begin{cases} 0 & (n=1), \\ -(n-1)\eta_{n-1} + (-1)^{n-1}(n-2)! & (n=2,3,4,\cdots). \end{cases} \tag{E.3}$$

Direct differentiation of equation (E.1) yields

$$\frac{dF}{dz} = \frac{2\ln(1+z)}{1+z}. \tag{E.4}$$

For $n=1$, equations (E.2) and (E.3) give

$$\frac{dF}{dz} = -2\eta_1(1+z)^{-1} + 2(1+z)^{-1}\ln(1+z) = 2(1+z)^{-1}\ln(1+z), \tag{E.5}$$

which is the same result with the direct differentiation of $F(z)$. From equation (E.2), we write the $(n-1)$th order derivative of $F(z)$ as

$$\frac{d^{n-1}F}{dz^{n-1}} = -2\eta_{n-1}(1+z)^{-n+1} + 2(-1)^{n-2}(n-2)!(1+z)^{-n+1}\ln(1+z) \tag{E.6}$$

for any integer $n \geq 2$. Differentiating equation (E.6), we derive

$$\begin{aligned} \frac{d^nF}{dz^n} &= 2(n-1)\eta_{n-1}(1+z)^{-n} \\ &+ 2(-1)^{n-1}(n-1)!(1+z)^{-n}\ln(1+z) + 2(-1)^{n-2}(n-2)!(1+z)^{-n}. \end{aligned} \tag{E.7}$$

Rearranging terms, we express the nth order derivative of $F(z)$ as

$$\begin{aligned} \frac{d^nF}{dz^n} &= 2(-1)^{n-1}(n-1)!(1+z)^{-n}\ln(1+z) \\ &- 2\left[-(n-1)\eta_{n-1} + (-1)^{n-1}(n-2)!\right](1+z)^{-n}. \end{aligned} \tag{E.8}$$

Applying the recursive relation in equation (E.3), we simplify the above expression as

$$\frac{d^nF}{dz^n} = 2(-1)^{n-1}(n-1)!(1+z)^{-n}\ln(1+z) - 2\eta_n(1+z)^{-n}, \tag{E.9}$$

which conforms with equation (E.2). Q.E.D.